University of Southampton Research Repository

Copyright © and Moral Rights for this thesis and, where applicable, any accompanying data are retained by the author and/or other copyright owners. A copy can be downloaded for personal non-commercial research or study, without prior permission or charge. This thesis and the accompanying data cannot be reproduced or quoted extensively from without first obtaining permission in writing from the copyright holder/s. The content of the thesis and accompanying research data (where applicable) must not be changed in any way or sold commercially in any format or medium without the formal permission of the copyright holder/s.

When referring to this thesis full bibliographic details must be given:

Thesis: Marzanna Szwaj (2022) "Nonlinear Optical Endoscopy with Anti-Resonant Hollow-Core Fibre (ARF) for Cancer Diagnosis ", University of Southampton, Faculty of Engineering and Physical Sciences, PhD Thesis.

Data: Author (Year) Title. URI [dataset]

University of Southampton

Faculty of Engineering and Physical Sciences

Chemistry

Nonlinear Optical Endoscopy with Anti-Resonant Hollow-Core Fibre (ARF) for Cancer Diagnosis

by

Marzanna Szwaj, MSc

Thesis for the degree of **Doctor of Philosophy**

February 2022

University of Southampton

Abstract

Faculty of Engineering and Physical Sciences

Chemistry

Doctor of Philosophy

Nonlinear Optical Endoscopy with Anti-Resonant Hollow-Core Fibre (ARF) for Cancer Diagnosis

Marzanna Szwaj

Endoscopy is a medical procedure used in examinations of internal organs and tissues to diagnose diseases including cancer. Presently, the gold standard in cancer diagnosis is x-Ray scanning, biopsy, and histology. This approach is very lengthy and intrusive. Often the treatment option for treating cancerous tumours is surgical intervention. Complete surgical removal of the tumours with minimal damage to the healthy tissues is a challenge and potentially can be achieved with an endoscope equipped to perform objective real-time imaging.

Nonlinear light-matter interaction forms the basis of multiphoton microscopy (MPM) that offers real-time and label-free imaging with a deeper penetration range. It combines multimodal imaging techniques that can give a spectrum of information on the molecular composition and morphology of biological specimens, permitting the detection of diseases with higher sensitivity and specificity. The second harmonic generation (SHG) and two-photon fluorescence (TPF) techniques signals, generated by fibrillar collagen and elastic fibres and some cell metabolic compounds, can deliver robust biological data for analysis of cancerous versus healthy tissue and their structural makeup, which is adding value to the overall diagnosis.

A fibre optic is key in the development of a portable miniature and laser-driven endoscopic instrument that would allow for the performance of MPM in the operating theatre. Its primary function is the efficient delivery of distortion-free ultra-short laser pulses to the sample. The potent candidate for multiphoton endoscopy is double-clad anti-resonant fibre (DC-ARF) characterized by light guidance and propagation properties free of dispersion and nonlinearity.

This thesis presents work on building an endoscope for nonlinear, multiphoton microscopy using DC-ARF. Its suitability for MPM was investigated in a series of tests, including a study to compare with the performance of DC-ARF with similar optical fibres. Then, DC-ARF was incorporated into a portable miniaturized hand-held microscope (HHM) to test different signal collection configurations in MPM (SHG and TPF) imaging. The final stage of this project describes the

development of a micro-endoscope with a piezo scanner actuator, micro-objective, and DC-ARF. The work consisted of several optimisation and development steps including generation and calibration of scanning patterns, selection and implementation of optical components to achieve a high-resolution image, and software creation for synchronized scanner operation with image reconstruction. The micro-endoscopic setup benefited from the compact size due to distortion-free high-power pulse delivery with DC-ARF without the need for dispersion and nonlinearity compensation optical elements. Additionally, utilization of cladding area of DC-ARF while maintaining the standardized fibre geometry for signal collection further decreased the setup dimensions by use of a single waveguide for bidirectional signal transmission. SHG images of mouse tail tendon and barium titanate crystals were successfully taken in the lab with the DC-ARF micro-endoscope. The work demonstrates the huge potential of the non-linear imaging micro-endoscopic system based on DC-ARF fibres. Overall, the novelty of the work is the study of a new DC-ARF for multi-photon imaging and the successful demonstration of portable-microscopic and micro-endoscopic applications.

Table of Contents

Table of Contents .... **i**

List of Tables .... **v**

List of Figures .... **ix**

Research Thesis: Declaration of Authorship .... **xix**

Acknowledgements .... **xxi**

Definitions and Abbreviations .... **xxiii**

Chapter 1 Introduction **1**

Chapter 2 Multiphoton Nonlinear Endoscopy **5**

- 2.1 Nonlinear Optics 5
  - 2.1.1 Second Harmonic Generation Process 6
  - 2.1.2 Two-Photon Fluorescence 8
  - 2.1.3 Biomedical Applications of Second Harmonic Generation and Two-Photon Fluorescence 9
- 2.2 Hollow-Core Fibre for Endoscopy 10
  - 2.2.1 Solid Core Fibre 11
  - 2.2.2 Dispersion 14
  - 2.2.3 Nonlinearity 15
  - 2.2.4 Nonlinear Pulse Propagation 16
  - 2.2.5 Hollow-Core Fibres 16
  - 2.2.6 Anti-Resonant Negative Curvature Hollow-Core Fibre 18
- 2.3 Towards Development of Endoscope for Multiphoton Microscopy 21
  - 2.3.1 Miniaturization 21
  - 2.3.2 Portability – Ultra-Short Pulse Delivery 23
  - 2.3.3 Remote Fibre-based Image Scanning Techniques 24
  - 2.3.4 Nonlinear Multiphoton Endoscopy 28
- 2.4 Conclusions 29

Chapter 3 Fibre Optics for Label-free Multiphoton Endoscopy **31**

- 3.1 Introduction 31
  - 3.1.1 Aim and Objectives 31
- 3.2 Characterisation of Double-Clad Anti-Resonant Fibre 32

3.2.1 Attenuation Measurement 33
3.2.2 Bend Loss Measurement 34

3.3 Suitability of Fibre Characteristics For Multiphoton Endoscopy 34

3.3.1 Optical Transmission 35
3.3.2 Nonlinear Spectral Effects 36
3.3.3 Dispersion 37
3.3.4 Polarization 38
3.3.5 M^2 Measurement 39
3.3.6 Second Harmonic Generation Imaging 40

3.4 Conclusions 49

Chapter 4 Hand-Held Microscope with Double-Clad Anti-Resonant Hollow-Core Fibre 51

4.1 Introduction 51

4.1.1 Aim and Objectives 52

4.2 The Experimental Setup 53

4.2.1 Detection Configurations 54

4.3 Performance of the Multiphoton Hand-Held Microscope 55

4.3.1 Free-Space Non-Descanned Detection 55
4.3.2 Free-Space Descanned Detection 57
4.3.3 Descanned Detection via Double-Clad Anti-Resonant Hollow- Core Fibre 59
4.3.4 Comparison of Different Detection Configurations for Hand-Held Microscope 61
4.3.5 Hand-Held Microscope for Multiphoton Microscopy 64
4.3.6 Comparison of Hand-Held Microscope Performance with a Traditional System for Multiphoton Microscopy 65

4.4 Conclusions 67

Chapter 5 Probe for Multiphoton Endoscopy with Double-Clad Anti-Resonant Hollow-Core Fibre 69

5.1 Introduction 69

5.1.1 Aim and Objectives 70

5.2 Development of the Probe for Multiphoton Endoscopy 70

5.2.1 Fibre Scanner.. 70

5.2.2 Spiral Scanning Pattern Generation 72

5.2.3 Optical Micro-System of the Micro-Endoscope 80

5.2.4 Imaging System.. 84

5.3 Multiphoton Micro-Endoscopic Imaging.. 87

5.3.1 The Experimental System 87

5.3.2 Second Harmonic Generation Imaging with Micro-Endoscope 89

5.3.3 Signal-to-Noise Ratio (SNR) 90

5.3.4 Resolution.. 92

5.3.5 Not a Number (NaN) Values.. 94

5.3.6 Optical Aberrations 97

5.4 Perspective and Future Work 97

5.5 Conclusions 100

Chapter 6 Conclusions and Perspective 101

List of References 103

Table of Contents

List of Tables

Table 1 Measured geometry of the DC-ARF main components.

Table 2 Table 2 Comparison of the geometry of the main components for three fibres: SCF, SC-ARF, and DC-ARF. HCFs have a very close dimension.

Table 3 Pulse duration of 116 fs laser measured directly at the fibre output for SCF, SC-ARF, and DC-ARF. FWHM of the autocorrelation function was divided by deconvolution factor corresponding to the pulse shape. For Gaussian beam, it was 1.41.

Table 4 Dispersion in fibres. Dispersion parameter (*D*) for group velocity dispersion (*GVD*) calculated for SCF, SC-ARF, and DC-ARF. ± - Standard Error of the Mean (SEM).

Table 5 Summary of the final specifications of multiphoton micro-endoscopic setup built in this project. Data presents optical parameters and some of the endoscope dimensions.

List of Figures

Photon energy diagram of two multiphoton processes; **(A)** in second harmonic generation (SHG) two incident photons ω_i of lower energy are combining to generate a new photon with double of the incident frequency; **(B)** in two-photon fluorescence (TPF), two photons are excited to the excitation state by the simultaneous absorption.

Figure 2.2 **(A)** Size of the excited volume in one-photon fluorescence (OPF) (left) and two-photon fluorescence (TPF) (right). In OPF, the emission is evenly distributed leading to the need for a pinhole to remove the out-of-focus signal. In TPF, the fluorescence emission is generated at the laser focus and out-of-focus light decreases as $1/z^2$ where z is the direction of the plane; **(B)** Comparison of OPF (lower beam) and TPF (upper beam) in a fluorescent dye cell (Adopted from https://www.newport.com/n/two-photon-microscopy).

Figure 2.3 Structure of the optical fibre. It contains a guided light core in the centre, a layer of cladding, and a plastic jacket to help confine the signal inside the core and to protect fibre.

Figure 2.4 Process of total internal reflection. When the angle of incident φ_1 is greater than critical angle φ_c, the total light is reflected back into the original material with refractive index n_1 and does not enter the new material (refractive index n_2).

Figure 2.5 Ray path and cross-section in step-index single-mode fibre. It is characterized by a sudden change in the refractive index value at the transition point between core and cladding.

Figure 2.6 Ray path and cross-section in step-index multimode fibre. It is characterized by a sudden change in the refractive index value at the transition point between core and cladding.

Figure 2.7 Ray path and cross-section in graded-index multimode fibre.

Figure 2.8 Schematic representation of structure of solid core photonic crystal fibre. Amendment of a diameter of capillaries d and the hole-to-hole distance Λ results in the control of fibre's modality and dispersion.

Figure 2.9 Nonlinearity **(A)** and dispersion **(B)** for different type of fibres. Kerr nonlinear coefficient is several orders of magnitude smaller for HC-PCF (**A**); HC-PCF has both normal and anomalous dispersion with the ZDW at the centre of the narrow transmission window (**B**). Adapted from [38].

Figure 2.10 SEM micrographs of different hollow-core fibres; **(A)** A HC-PBG fibre [42]; **(B)** a Kagome lattice HC fibre [43]; **(C)** negative curvature antiresonant hollow-core fibre (ARF), it contains a hollow- core in the centre, cladding (microstructure with the ring of glass, and coating).

Figure 2.11 Attenuation comparison for three types of fibres: anti-resonant **(A)** photonic bandgap **(B),** and solid core **(C)**. The graph presents different sources of losses and CL – confinement loss, SSL- scattering surface loss. The solid line is measured data, while dotted/dashed lines are simulated data. The dominated losses in ARFs come from CL, while in PBGF from SSL [39].

Figure 2.12 Principle of ARROW guidance, when the propagated light is in on resonance and off-resonance state.

Figure 2.13 Optical microscope image of NANF cross-section **(A)**, comparison between ARF and NANF: structural **(B)** and confinement loss (CL) **(C)**. NANF has additional tubes that decreased CL [39].

Figure 2.14 Portable microscopes; (**A**) Schematic representation of the setup with a portable microscope for imaging freely moving animal's brain [52]; (**B**) Digital image of a hand-held microscope [55].

Figure 2.15 Fibre bundle; (**A**) SEM image; (**B**) microscope image with hundredfold magnification [70].

Figure 2.16 Microelectromechanical system (MEMS) scanning mirror; (**A**) schematic representation of MEMS [61]; (**B**) a MEMS actuator with a 600μm diameter mirror [73]; (**C**) Location of 2-axis scanning MEMS mirror inside the probe [72].

Figure 2.17 Graphical reconstruction of three main scan pattern modes: (**A**) spiral; (**B**) Lissajous; (**C**) raster [74].

Figure 2.18 Various types of piezo actuators; (**A**) tubular piezo scanner based on resonant scan [75]; (**B**) The miniaturized fibre raster scanner driven by high-performance two-layer piezoelectric actuators or bimorphs [78]; (**C**) fibre actuator with two orthogonally placed piezoelectric bimorph cantilevers for a multiple-pattern generation [74].

Figure 2.19 Multiphoton endoscopy; (**A, B**) Label-free in vivo examination of rat kidney with SHG (green) and TPF (red). Images (**A, B**) presents the different size of FOV. Scale bars 50 μm. [80]; (**C**) images of human colon SHG (green), CARS (red) pump/stocks power P = 20/10 mW, SHG power P =60 mW [81].

Figure 3.1 DC-ARF with its transmission and bend loss characterization; **(A)** The optical image of the DC-ARF cross-section. Thanks to low refractive index coating (not visible on the image due to fibre cleaving) light can be guided in the core by glass anti-resonance and in glass cladding based on total internal reflection (TIR); **(B)** Image of the light confined in hollow-core and cladding of the DC-ARF; **(C)** Attenuation spectrum of the DC-ARF obtained in cut-back test, highlighting fundamental window with loss <0.2dB/m over 500 nm wide band, high loss region and second transmission window; **(D)** Bend loss of DC-ARF for different bend radii and wavelengths.

Figure 3.2 Comparison study of SCF, SC-ARF and DC-ARF; **(A)** Measured transmission spectra in the core and cladding for all three fibres that show their strong guiding properties between

800 -100 nm in the core required for excitation light, and DC-ARF transmission capacity in the cladding; **(B)** The effect of optical nonlinearity on pulse laser propagation in all three fibres taken at 810 nm and 900 nm for 20 mW (bottom four rows) and 60 mW (top four rows). Increased power has no effect on spectra in two HCFs, and it caused strong spectral broadening for SCF.

Figure 3.3 Dispersion in ARFs **(A, B)** comparison of GVD simulated data (black) with measured results (red) for SC-ARF and DC-ARF; **(C, D)** Intensity autocorrelation traces of the transform-limited fs laser pulses (116 fs Ti:Sa) measured at the input and output of the 3 m DC-ARF at 810 nm and 900 nm and 20 mW power.

Figure 3.4 Dependence of transmission power behaviour on different degree of polarization for pulse laser propagated in free-space, SCF, SC-ARF, and DC-ARF. The results demonstrate the polarization-maintaining properties of ARFs.

Figure 3.5 M^2 results for three studied fibres and the laser pump. Guiding light in the SC-ARF and DC-ARF maintained high focusing capacity that is supported by M^2 results close to 1.

Figure 3.6 Schematic representation of SHG system working in non-descanned detection (NDD) (**A**) and descanned detection (DD) (**B**) signal collection configuration. The red thick line represents the excitation path and the blue thick line - signal collection path. FI – Faraday isolator, GSM – Galvanometric scanning mirrors, BE – Beam expander, DM – Dichroic mirror, F – Filter, PMT – Photon multiplier tube.

Figure 3.7 SHG images of mouse tail tendon taken in non-descanned detection (NDD) and descanned detection (DD) configuration using 1 m (**A**) and 3 m (**B**) SCF, SC-ARF and DC-ARF at 810 nm and 900 nm excitation wavelength are shown. The images were obtained from different areas of the same samples; (NDD: 20x objective, zoom 3, 341 pixels, 10,7 µs dwell time, ~20 mW power; DD: 20x objective, zoom 3, 341 pixels, 27 µs dwell time, ~20 mW power, average 10 frames). Scale bar = 50 µm.

Figure 3.8 SHG images of barium titanate crystals taken in non-descanned detection (NDD) and descanned detection (DD) configuration using 1 m (**A**) and 3 m (**B**) SCF, SC-ARF and DC-ARF at 810 nm and 900 nm excitation wavelength are shown. The images were obtained from different areas of the same samples; (NDD: 20x objective, zoom 3, 341 pixels, 10,7 µs dwell time, ~20 mW power; DD: 20x objective, zoom 3, 341 pixels, 27 µs dwell time, ~20 mW power, average 10 frames). Scale bar = 50 µm.

Figure 3.9 SHG images of mouse tail tendon (**a, b**) and barium titanate crystals (**c, d**) taken using a free-space propagated laser at 810 nm and 900 nm excitation wavelength. The images were obtained from different areas of the same samples; (20x objective, zoom 3, 341x341 pixels, 10.7 µs dwell time, ~ 20 mW power). Scale bar = 50 µm.

Figure 3.10 The analysis of the SNR for mouse tail tendon images taken in non-descanned detection (NDD) configuration. Images obtained in NDD for 1 m (**A, B**) and 3 m (**C, D**) long SCF,

SC-ARF, DC-ARF presented in **Fig. 3.7** underwent SNR examination and the average SNR for the signal profile (**Fig. 3.7A1)** vs distance was plotted. The noise level was reduced for light propagated in 3 m fibre and is comparable with free-space laser propagation (black and red profile on the graphs).

Figure 3.11 The analysis of the SNR for barium titanate crystals images taken in non-descanned detection (NDD) configuration. Images obtained in NDD for 1 m (**A, B**) and 3 m (**C, D**) long SCF, SC-ARF, and DC-ARF presented in **Fig. 3.8** underwent SNR evaluation and the average SNR (**Fig. 3.7A1)** vs distance along the line-profile is plotted. The noise level was reduced for light propagated in 3 m fibre and is comparable with free-space laser propagation (black and red profile on the graphs).

Figure 3.12 Measured grey as a function of distance for SHG barium titanate crystals images (**Fig. 3.8 A, B** images 1). The decrease in signal intensity between 1 and 3 m long solid core fibre (SCF) is mainly caused by anomalous group velocity dispersion (GVD) and nonlinearity.

Figure 3.13 SNR analysis performed for mouse tail tendon and barium titanate crystals samples captured with descanned detection for 1m and 3 m long DC-ARF. The graphs of SNR vs distance are for mouse tail (**a, b**) and barium titanate crystals (**c, d**) measured along the line-profile (white line on the images in the middle) for images 6 and 12, **Figures 3.7** and **3.8 A, B** images. There is noticeable noise suppression for 3 m DC-ARF leading to similar SNR for two fibres lengths (red line profile).

Figure 4.1 HHM; **(A)** Schematic representation of the experimental design shows the main parts of the HHM: fibre, Galvano mirrors, beam expander, and optical objective; the HHM was tested with different detection configuration, that are presented on a diagram (fNDD, fDD, DD); **(B)** Assembled presentation of the HHM executed in Fusion 360, Autodesk software; **(C)** Photo of the HHM.

Figure 4.2 Experimental HHM setup for free-space NDD. In this configuration the detection section (band pass filters, L_5 lens and the PMT) is placed just behand the microscope objective. The dichroic mirror (DM 458) separates the signal from the excitation.

Figure 4.3 Images acquired with the HHM operating with the free-space NDD configuration of (**A** – top row) barium titanate crystals and (**B** – bottom row) mouse tail tendon samples using the SHG modality. Two different areas are shown for the same sample. Image parameters: 20x objective, pixels – 512 x 512, dwell time 32 µs, optical zoom x 3, ~ 20 mW average power on the sample.

Figure 4.4 Experimental HHM setup for free-space DD illustrates part of detection path (band pass filters, L_5 lens, and the PMT) placed at the distal end of the fibre. The dichroic mirror (DM 458) separates the signal collection path from the excitation path.

Figure 4.5 Images obtained in the HHM operating with fDD mode of (A – top row) barium titanate crystal and (B – bottom row) mouse tail tendon samples using the SHG modality. Two

different areas are shown for the same sample. Image parameters: 20x objective, pixels – 512 x 512, dwell time 32 µs, optical zoom x 3, ~ 20 mW average power.

Figure 4.6 Experimental HHM setup for DD via DC-ARF has detection section parts (band pass filters, L5 lens and the PMT) placed at the proximal end of the fibre. The dichroic mirror (DM 458) separates the signal collection path from the excitation path. Two additional lenses (L6, L7) were added for higher nonlinear signal coupling efficiency.

Figure 4.7 Images obtained with the HHM operating with DD via DC-ARF mode based of (**A**) barium titanate crystals (a single frame) and (**B**) mouse tail tendon (3 average frames) samples using the SHG modality. Image parameters: 20x objective, pixels – 512 x 512, dwell time 32 µs, optical zoom x 3, ~ 20 mW average power.

Figure 4.8 SHG images of barium titanate crystals taken with the HHM system under three different types of detection configuration (**A**) fNDD, (**B**) fDD, and (**C**) DD via DC-ARF. Two representative images of different areas on the sample are shown for each configuration.

Figure 4.9 SHG images of mouse tail tendon taken with the HHM system under 3 different configurations: (**A**) fNDD, (**B**) fDD, and (**C**, **D**) DD via DC-ARF. Two representative images of different areas on the sample are shown for each configuration. For fNDD (**A**) and fDD (**B**) a single frame was acquired. For DD via DC-ARF images with 3 averaged frames (**C**) and 1 frame (**D**) are shown.

Figure 4.10 SNR analysis of four images of mouse tail obtained using HHM system in fNDD, fDD, and DD via DC-ARF signal collection configuration from different area of the sample. **Images 1, 2, 3,** were taken with single frame acquisition, **image 4** was obtained with 3 averaged frames. **Graph A** presents gray value as a function of distance acquired along a white profile line seen on images. From these results in the **graph A**, SNR was calculated (**graph B**). Scale bar = 50 µm.

Figure 4.11 Transmission range of 458 nm long-pass filter (Semrock, FF458-Di02) used in the HHM system. The transmission band of DM affected the selection of TPF signal that could be collected from biological tissue.

Figure 4.12 SHG and TPF images of mouse bone tissue (**A**) and mouse lung tissue (**B**) (separate (**1, 2**) and merged (**3**)). Excitation wavelength SHG – 810 nm, TPF – 835 nm; signal collection SHG – 405 nm, TPF – 450 nm; Power on the sample ~ 30 mW; Obj. 20x/ NA 0.75; Pixels 512 x 512; Dwell time 32000 ns; optical zoom 3.

Figure 4.13 Comparison of HHM performance in fNND configuration with benchtop microscope system using barium titanate crystals (**A**) and mouse tail tendon (**B**) samples. Two representative images of different areas on the sample are shown for each setup. Technique SHG; Excitation wavelength 810 nm; signal collection 405 nm, Power on the sample ~ 15 mW; Objective 20x / NA 0.75; Pixels 512 x 512; Dwell time 32000 ns; Optical zoom 3.

Figure 4.14 SNR analysis of SHG mouse tail images obtained using benchtop multiphoton microscopy system (**A**) and HHM system (**B**) in fNDD, detection configuration with average power on the sample ~15mW. Graph 1 presents grey values as a function of distance acquired along a white profile line seen on images. The SNR calculated from these imaging results is shown in graph 2.

Figure 5.1 **(A)** An assembled scanner. The main components are: PZT, fibre optic, adaptors, wires, and collar; **(B-C)** 3D printed adaptors used to increase fibre alignment with the main axis of the probe (top and side view).

Figure 5.2 **(A)** The structure of the piezoelectric tube contains four isolated electrodes (a-d) on its external surface, and the inner electrode (e) serves as ground; **(B)** Deflection of the PZT in response to the applied external voltage (adapted from https://www.piezodrive.com).

Figure 5.3 Resonance frequency for free-standing fibre in the endoscopic probe; **(A)** Evolution of the calculated resonance frequency as a function of the length of free-standing DC-ARF; **(B)** Experimentally measured resonance frequencies of two axes for fibre resonator were found to be 812 Hz for the x-axis and 819 Hz for the y-axis.

Figure 5.4 Schematic representation of the spiral scan formation; **(A)** Two sine waves with a linearly modulated amplitude and 90° phase shift creates a spiral pattern **(B)**.

Figure 5.5 Formation of the linearly increased sine wave from ramp and sine function.

Figure 5.6 The amplitude-modulated signal drive of the fibre scanner. It contains three periods: imaging scan, active breaking, and free decay. The imaging scan period sweeps the sample area and fibre collects the signal, while active braking and free decay return the fibre to its initial position and remove residual oscillations.

Figure 5.7 Red curve plot represents the fibre tip motion in response to a generated signal (grey curve). The transient regimes at the beginning of the outgoing spiral indicate a high $\boldsymbol{Q}$ factor.

Figure 5.8 Whirling effect of the fibre resonator: **(A) 1-2** Cross-coupling of axes x and y when individual electrode resonated at its f_{RES} resulting in the elliptic trajectory; **(A) 2-3** Using off-resonance frequencies causes electrodes to follow line scan with a smaller displacement; **(B)** Whirling effect registered with the PSD, here single fibre axis was driven by a linearly increasing sine wave **1-2** at fibre resonance and **3-4** off fibre resonance.

Figure 5.9 Elimination of the whirling effect by creating two virtual axes X_V and Y_V, and changing the $\boldsymbol{\theta}$ angle between them and the real pair electrodes X, Y.

Figure 5.10 Correction of the phase deviation by adding extra phase value to obtain the circular pattern; **(A)** A circular scan with a 90° phase shift between two electrodes performs an elliptic trajectory; **(B)** an additional 27° removes the elliptic shape and corrects it to obtain a circular scan.

Figure 5.11 Registered spiral scanning pattern of the fibre scanner; **(A)** The PSD registers the *x* and the *y* position of the rotating fibre scanner with time; **(B)** spiral scan in the *x-y* plane. **Figure 5.12** is an example image of a motionless **(A)** and resonating fibre-optic cantilever **(B)**.

Figure 5.12 Fibre-optic cantilever at rest **(A)** and when performing the oscillations **(B)**.

Figure 5.13 Micro-sphere insulation process in DC-ARF and its impact on laser beam diameter; **(A)** Setup used in the micro-sphere installation in the fibre face contains fibre facing down to make contact with micro-spheres placed on the microscope slide. The procedure is assisted with an optical microscope and 3D stage; **(B)** The side–view of the DC-ARF with the micro-bead inserted as shown by the white arrow; An image of the laser beam spot through the DC-ARF **(C)** without and **(D)** with a microsphere, bar scale = 17 µm.

Figure 5.14 Improved focus of a laser beam spot with a micro-sphere. The size of the core diameter of the DC-ARF **(A)** and DC-ARF with an attached micro-sphere in the core **(C)** observed with a beam profiler camera. The beam profile was measured again after the beam propagated a distance of 0.36 mm. A significant increase in the spot diameter was observed for the fibre with the micro-sphere **(D)** while for that without the bead, negligible difference in the beam waist dimension was noticed **(A-B)**.

Figure 5.15 Micro-lens assembly objective designed for micro-endoscopic probe is composed of two achromatic doublets from Edmund Optics: L_1 - #84-127, L_2 - #84-128.

Figure 5.16 Schematic representation of the architecture of the imaging procedure that contains two steps: *scan calibration* that obtains *x(t)*, *y(t)* position of the fibre scanner motion, and *imaging* – sample intensity signal acquisition. The image is reconstructed based on the fibre position and signal intensity data.

Figure 5.17 Image construction requires fibre position measurement **(1)**, which is converted to its pixel coordinates **(2)** creating a square matrix. The average light intensity is assigned to the spot position on the matrix specified at detection **(3)**. A second matrix is created to assign a number of counts for each pixel **(3)**. Finally, two matrices are normalized and the image is generated.

Figure 5.18 Schematic representation of the setup for micro-endoscopy. There are four distinct paths that are highlighted;; *optical paths for*: light excitation (red), signal collection (blue); and *electrical connections for* : V_x, and V_y waveform generation (black), fibre position measurement *x(t)*, *y(t)*, and signal intensity *I(t)* (yellow). PMT - Photon multiplier tube, PSD – Position sensitive detector, BNC – Terminal block, PZT – Piezo tube, L -lens.

Figure 5.19 SHG images of a mouse tail tendon (**row A**), and barium titanate crystals (**row B**) taken with the multiphoton micro-endoscopic system using SHG technique. Image parameters: pixels 300x300, 0.33 fps, ~ 40 mW on the sample, magnification 0.28. Scale bar = 60 µm.

Figure 5.20 Images of barium titanate crystals with 1, 5, and 15 averages obtained from different areas of the same sample. Images show improvement in signal level as the number of frames increases. Scale bar = 60 µm.

Figure 5.21 Images of mouse tail tendon obtained with 1, 5, and 15 averages from different areas of the same sample. Images show improvement in signal level as the number of frames increases. Scale bar = 60 µm.

Figure 5.22 Graphs in panel **A** present grey value vs distance for the images taken along the white line profiles (images 1, 2, 3). Graphs in panel **B** show SNR as a function of distance for the images 1, 2, 3 obtained along with the white line profile.

Figure 5.23 PSF measurements: **(A)** Image of 5 µm polystyrene beads obtained with the system for multiphoton micro-endoscopy in the forward detection scheme; **(B, C)** signal intensity peaks shows the FWHM at 6.75 µm and 13.7 µm in the lateral and axial direction, respectively; **(D)** Intensity map of the 3D PSF along the *xz* plane.

Figure 5.24 Uniform sampling points distribution.

Figure 5.25 Changes in sampling point’s distribution for different spiral time durations. For more uniform distribution of sampled points across an image plane, hence, a reduction NaN numbers, the *d*, *f* images were selected as a template for image reconstruction.

Figure 5.26 Post-process hybrid interpolation: raw data undergo linear interpolation, which estimates the missing NaN values that are then used in the hybrid interpolation process to refill absent information on the original image matrix (**row A**). Example of the hybrid interpolation applied on images taken with the micro-endoscopic system (**row B**). Image 4 shows raw data with black dots representing missing values; in image 5, raw data from image 4 underwent linear interpolation; image 6, hybrid interpolation assigned only NaNs obtained in linear interpolation to the black spots in image 4.

Figure 5.27 Transmission image of the 20 µm PB obtained in the forward detection presents off-axis spherical aberrations and the beads become blurry at the edges of the image. Bar scale = 60 µm.

Figure 5.28 The examples of misalignment of optomechanical components **(A)** generation of deviation angle between fibre and adaptor that will increase with the distance and caused the laser beam enter the lenses assembly far off from the centre of the lens surface; **(B)** Micro-sphere insulation process in DC-ARF shows fibre tip that must be perpendicular to glass slide position to improve micro-sphere alignment with the axis of the fibre’s core.

Research Thesis: Declaration of Authorship

Print name: MARZANNA SZWAJ

Title of thesis: Nonlinear Optical Endoscopy with Anti-Resonant Hollow-Core Fibre (ARF) for Cancer Diagnosis

I declare that this thesis and the work presented in it are my own and has been generated by me as the result of my own original research.

I confirm that:

1. This work was done wholly or mainly while in candidature for a research degree at this University;
2. Where any part of this thesis has previously been submitted for a degree or any other qualification at this University or any other institution, this has been clearly stated;
3. Where I have consulted the published work of others, this is always clearly attributed;
4. Where I have quoted from the work of others, the source is always given. With the exception of such quotations, this thesis is entirely my own work;
5. I have acknowledged all main sources of help;
6. Where the thesis is based on work done by myself jointly with others, I have made clear exactly what was done by others and what I have contributed myself;
7. None of this work has been published before submission

Signature: ....Date 28.02.2022

Acknowledgements

I would like to thank my supervisors Professor Sumeet Mahajan and Professor Francesco Poletti for giving me the opportunity to do this fantastic project. I am grateful for your support and guidance as mentors, but also for showing me real Academia.

Dr Ian Davidson, thank you for the time you spent explaining to me the fibre optics, for your emails, support, and that I always felt welcome.

My colleagues Dr Anna Crisford, Dr Peter Johnson, and Dr Niall Hanrahan, thank you for the science-time and the fun-time we had together.

Dr David Gray, our collaboration on the software for micro-endoscopy system faced many challenges. Thank you for not giving up on the project at the beginning, when University introduced restrictions, and for your hard work afterward knowing, I had only 4 months for the project to end. My only regret is that I did not learn more about LabView.

My good friend, Kam Kaur-Bicchu, your hugs many times lifted my spirit.

Finally, to my beloved husband and life partner, Andrzej Samborowski –we did it! You pushed me into this deep water, and not only taught me how to swim in it, but every time I was drowning, you threw me a lifebuoy. You were always there to discuss my project, to teach me engineering skills, and to mentor me on independent thinking. I am very lucky to have you in my life.

In the end, I would like to quote the song that led me through the last 4 years and gave me the strength not to give up:

> *Carry on, my wayward son*
>
> *There'll be peace when you are done*
>
> *Lay your weary head to rest*
>
> *Don't you cry no more*
>
> (“Carry On Wayward Son” by Kansas”)

So now, like Bilbo Baggins would say: I am ready for a new adventure!

Definitions and Abbreviations

APD	Avalanche photodiodes
ARF	Anti-resonant hollow-core fibre
ARROW	Anti-resonant reflection optical waveguide
BE	Beam expander
BNC	Terminal block
CARS	Coherent anti-Stokes Raman scattering
CL	Confinement losses
DC-ARF	Double-clad anti-resonant fibre
DD	Descanned detection
DM	Dichroic mirror
FB	Fibre bundle
FGS	Fluorescence-guided surgery
FL	Focal length
FOV	Field of view
FP	Fabry – Perot
FS	Fibre scanner
FR	Frame rates
FWHM	Full width at half maximum
FWM	Four-wave mixing
GRIN lens	Gradient-index lens
GVD	Group velocity dispersion
HCF	Hollow-core fibre
HC-PBG	Hollow-core photonic band gap
HC-PCF	Hollow-core photonic crystal fibre
HHM	Hand-held microscope
IC	Inhibited coupling
LMA	Large mode area

M	Magnification
MEMS	Microelectromechanical system scanning mirror
MFD	Mode-field diameter
MPE	Multiphoton endoscopy
MPM	Multiphoton microscopy
NA	Numerical aperture
NaN	Not a number
NANF	Nested anti-resonant nodeless fibre
NDD	Non-descanned detection
NIR	Near-infrared
OPF	One-photon fluorescence
OSA	Optical spectrum analyser
PB	Polymer beads
PCF	Photonic crystal fibre
PMF	Polarization maintenance fibre
PMT	Photon multiplier tube
PSD	Position sensitive detector
PSF	Point spread function
PZT	Piezo tube
SC-ARF	Single-clad anti-resonant fibre
SCF	Solid core fibre
SHG	Second harmonic generation
SNR	Signal-to-noise ratio
SMF	Single mode fibre
SOP	State of polarization
SPM	Self-phase modulation
SSL	Scattering surface loss
TIR	Total internal reflection
TPF	Two-photon fluorescence

UV	Ultraviolet light
VIS	Visible light
WD	Working distance
WLS	White light source
ZDW	Zero dispersion wavelength

Chapter 1 Introduction

Cancer claims millions of lives worldwide every year. According to Cancer Research UK [1], in 2015, there were 359 960 new cases of cancer in the UK alone, which was nearly 1000 per day. With the rate of death of 163 444, the survival rate is only about 50%. However, 33% of cancer cases are preventable, and early diagnosis will potentially increase patient's chances of complete recovery or at least extend lives.

Currently, the only available cancer treatment is the surgical removal of a cancerous tumour, in combination with chemotherapy and postoperative radiation therapy [2]. Unfortunately, during the removal of a cancerous body, a region of healthy tissue undergoes resection to eliminate the chances of leaving any cancer cells behind in the surgical cavity. This process is technically challenging and has to be performed with microscopic precision to avoid removing vital healthy tissue regions and thus compromising the patient's quality of life post-surgery. At the same time, any missed tumour tissues have the potential to cause a re-lapse of the disease and complications leading to lower survival rates.

The methodology currently used in clinical practice relies on the surgeon's ability to identify tumour boundaries in real-time [2]. The assessment of a surgical margin is established post-operative based on the histology examination or X-ray scanning of the tumour sample. To recognize the cancer margin within the patient, the contrast agent or molecular probes can be used. However, the approval of suitable probes is a lengthy process. In addition, the administration and utilization of such a probe in the patient is a very complex process.

5-ALA (5-aminolevulinic acid) is one of the most common contrast agents used clinically in Fluorescence-Guided Surgery (FGS) as a fluorescent dye for tumour discrimination from the healthy tissue [3]. However, this method is limited by different level of fluorescence emission and signal strength depending on person's dye uptake into the tumour. Additionally, 5-ALA is relatively of high costs and has to be orally administrated with the high risk of skin sensitization within 24 h after the operation.

For these reasons, providing medical personnel with the best state-of-the-art equipment capable to identify cancer margins in real-time is most desirable and highly sought.

There is a high need for label-free, real-time "digital histology" to examine tumour residues on the cellular level during surgery. Such a technology would provide not only slide-free, dye/stain-free inspection but also help to find a better solution for cancer treatment and save financial and human resources.

Nonlinear multiphoton microscopy (MPM) meets all the above requirements for “digital histology”. As a very powerful tool for live tissue imaging, MPM does not require staining of the samples and provides high special resolution and molecular specificity at the same time. MPM combines different nonlinear and multiphoton contrast techniques, such as coherent anti-Stokes Raman scattering (CARS), second harmonic generation (SHG), and two-photon fluorescence (TPF). However, the focus of this thesis is placed mainly on the exploration of the SHG modality.

In SHG, two incident photons of the same energy and frequency are directly converted into one photon during the interaction with the medium; the resultant photon has twice the energy and frequency of the original photons [4]. In biomedicine, SHG is used mostly for the analysis of connective tissue that is rich in Collagen Type I in rat tail, Collagen Type II in human articular cartilage, and is strongly SHG active [5-7].

Multiphoton imaging has been successfully applied in studies of molecular, metabolic, and physiological processes to visualize both actual tumour cells and tumour microenvironment [8-13]. For these reasons, MPM is a promising tool for performing *in vivo* optical histology.

The conventional configuration for the MPM has very large and bulky dimensions that are not suitable for the clinical environment especially for providing surgical guidance. Therefore, MPM design for surgical applications needs the development of a miniature and portable endoscope platform. One of the key issues in the development of such an instrument is optical fibre for delivery of an ultra-short pulse laser that has to be applied in MPM system since the signal intensity of MPM is inversely proportional to the pulse width of the laser [4]. Hence, fibre selection has to be based on its capability to guide short pulses without any distortion over the excitation spectral region of MPM (700 -1100 nm). However, propagation of the pulse in a solid core fibre (the current prevalent fibre technology) is affected by dispersion and nonlinear response that causes temporal and spectral broadening of the pulse that decreases the efficiency of nonlinear signal excitation. To overcome these effects, pre-compensation schemes have been proposed [14-17], but they introduce complexity to the system by adding additional components.

The emergence of hollow-core fibre (HCF) technology creates guiding conditions for ultra-short pulses similar to free-space light propagation. Therefore, dispersion and nonlinearity are very low in HCFs resulting in their negligible effect on propagated ultra-short pulses [18].

The overall aim of this PhD project is to build an endoscope for nonlinear multiphoton imaging techniques using a new type of HCFs - tubular double-clad anti-resonant fibres (DC-ARF). It is characterized by a simplistic design, large core diameter and broad spectral transmission with low attenuation. Furthermore, low refractive index coating creates an additional area for signal transmission that is adopted for the collection of signal from the sample.

The novelty of this project lies in the integration of a new DC-ARF with a system for multi-photon micro-endoscopy and the successful demonstration of imaging of non-biological and biological samples. Apart from excellent properties for high power, short pulse delivery, and back signal collection, DC-ARF preserves the standard size of geometry with only one layer of low refractive index jacket that allows for increased fabrication replicability. Employment of waveguide with smaller dimensions and higher cladding NA for light emission provides better miniaturization of the system without compromising on the collected signal level.

In this thesis, the endoscope development is divided into three parts that contain:

- The characterization of a new DC-ARF and its comparison with a standard solid core fibre (SCF) and ARF of similar dimension to DC-ARF but without the transmission ability in the cladding (Chapter 3).
- The construction of a hand-held microscope (HHM) with DC-ARF for remote operation and testing its multiphoton imaging capability in different signal collection configurations: free-space non-descanned detection (NDD), free-space descanned detection (DD), and decanned detection (DD) via DC-ARF (Chapter 4).
- The development of a miniaturized system for multiphoton endoscopy with piezo tube actuator, achromatic miniature lens assembly and DC-ARF for SHG imaging (Chapter 5).

This thesis is organized as follows:

Chapter 2 introduces the concept of nonlinear optics and two multiphoton modalities: Second Harmonic Generation and Two-Photon Fluorescence. Then, the most crucial aspects of the fibre optics technology are presented including pulse propagation in optical fibres, dispersion, and nonlinearity. The chapter also discusses different types of hollow-core fibres like Photonic Bandgap and Kagome, and finally talks about tubular double-clad anti-resonant hollow-core fibres (DC-ARF) that is used for the development of the endoscope in this PhD. The second part of chapter 2 examines the main design requirements for endoscopes like miniaturization, portability, and optical fibres. Furthermore, remotely operating imaging devices are categorized based on their size and the proximal or distal locating of scanners and is supported with the examples from the literature.

Chapter 3 reports the characterisation of the DC-ARF. Main characteristics such as transmission, attenuation, bend loss, and numerical aperture (NA) are presented. The second part of the chapter examines the suitability of DC-ARF for MPM by comparing it against single clad anti-resonant hollow-core fibres (SC-ARF) with dimensions similar to the DC-ARF but with the capacity to guide the light in the core only, and solid-core fibre (SCF). A crucial factor that decides on fibre selection for MPM is its ability to deliver distortion-free ultra-short pulses; hence all three fibres undergo appropriate measurements that show no alteration in the spectral and temporal domain of the laser pulse width after propagation in HCFs. Moreover, SCF, SC-ARF, and DC-ARF were connected to the laboratory benchtop SHG microscope imaging system to obtain images of mouse tail tendon and barium titanate crystals in NDD and DD configuration. Presented results show that only DC-ARF has the ability to deliver unaltered laser pulses to the sample and collect signal simultaneously.

Chapter 4 presents the development of a hand-held microscope (HHM) and evaluation of its performance with SHG and TPF imaging under a variety of signal collection configurations (free-space non-descanned detection (NDD), free-space descanned detection (DD), and decanned detection (DD) via DC-ARF). This work was for transitioning towards building the endoscope and is concerned with the incorporation of DC-ARF to remotely operating imaging device at the development stage. Produced results helped in a better understanding of the endoscope for MPM that was built in this thesis work.

The culmination stage of this project is contained in Chapter 5, which reports the construction and evaluation of the micro-endoscopic probe – this is the part which uses the delivered pulsed-laser and scans the sample to generate an image. The first part of this chapter describes the generation and calibration of the spiral scan pattern using a tubular piezo actuator and the assembly process of a custom-designed miniature lens system. Furthermore, there are descriptions on developing the software in LabView for scan control, signal acquisition and image reconstruction. Later in the chapter, SHG images of mouse tail tendon and barium titanate crystals obtained with the endoscope are presented. The section discusses their resolution, signal-to-noise ratio, and appearance of Not a Number values.

Chapter 2 Multiphoton Nonlinear Endoscopy

This chapter will introduce the theoretical foundation underlying multiphoton nonlinear endoscopy including two imaging modalities that are used in this project: second harmonic generation (SHG) and two-photon fluorescence (TPF), with examples of their applications in biomedical imaging. Furthermore, this chapter will provide an overview of optical fibre technology together with the development of hollow-core waveguides. Further, the current progress and knowledge in label-free, multiphoton endoscopy will be discussed. The key technical aspects required of a miniature imaging device will be examined based on portability, miniaturization, scanner type, and fibre.

2.1 Nonlinear Optics

Nonlinear optics studies the effect of the intense, incident electromagnetic field on matter [19, 4]. On the atomic level, an applied electric field will affect particles in the material in a way that negatively charged electrons will move in the opposite direction to the applied field, and positive charges will be attracted to this field [19]. A linear or nonlinear processes is defined by the relationship between the applied electric field $\boldsymbol{E}$ and the polarization of the material $\boldsymbol{P}$. Under the influence of the field, an electric dipole is created with electric dipole moment $\boldsymbol{\mu}(t)$, which is expressed by:

$$\mu(t) = -e \cdot r(t) \qquad (1)$$

where $-e$ stands for the charge of the electron, and $r(t)$ is the displacement which is related to the strength of bonding of the electrons with the nuclei. Sum of all N electric dipoles per unit volume in the material results in microscopic polarization P:

$$P(t)=N\mu(t) \qquad (2)$$

If an electric field is applied, an induced polarization is linearly proportional to its magnitude which is a fundamental dependence for linear optical processes to occur.

$$P(t) = \varepsilon_0 \chi E(t) \qquad (3)$$

where ε_0 is the electric permittivity in a vacuum, and χ is the susceptibility of the material.

For higher intensity, the response of the electrons in the material is different - they are displaced further from their equilibrium status and their harmonic binding potential becomes more an-harmonic. The induced polarization is not linear anymore, and the susceptibility of the material will no longer be of the same magnitude. This induces a higher-order susceptibility, and the relationship (3) includes higher order terms for the material susceptibility:

$$P(t) = \varepsilon_0\chi_1 E^1(t) + \varepsilon_0\chi_2 E^2(t) + \varepsilon_0\chi_3 E^3(t) + \ldots \tag{4}$$

Where $\chi 1$ is the linear susceptibility, $\chi 2$ and $\chi 3$ are the second - and third-order susceptibility. The term $\chi 2$ is responsible for the second harmonic generation phenomenon.

2.1.1 Second Harmonic Generation Process

The phenomenon of second harmonic generation (SHG) was first discovered in 1961 in quartz crystals [4] by a team led by Peter Franken at the University of Michigan in Ann Arbor. In their study, a ruby laser beam at 694.3 nm propagated into a slab of crystalline quartz resulting in a nonlinear response at 347.15 nm.

Second harmonic generation, which is the simplest of the second-order nonlinear processes, can occur only in media that are non-centrosymmetric (due to their lack of inversion symmetry). It results from the fact that all even-order nonlinear susceptibility $\chi_{(n)}$ (including second-order χ_2 for SHG) terms vanish in centrosymmetric materials because they do not exhibit asymmetric characteristics. Second harmonic generation activity is shown by Type I and Type II collagen fibres or microtubules [5-7] in biological tissue, and also in birefringent crystals like barium titanium oxide or barium titanate ($BaTiO_3$) [20].

Second Harmonic Generation Theory

The electromagnetic field strength is expressed by:

$$E(t) = Ee^{-i\omega t} + c.c. \tag{5}$$

where i is the imaginary unit, ω – field frequency, $c.c$ – complex conjugate. When the applied field with frequency $\omega_1 = \omega$ interacts with medium with non-zero χ_2, a polarization of material is created with new frequency $\omega_2 = 2\omega$.

$$P_2(t) = \varepsilon_0\chi_2 EE + (\varepsilon_0\chi_2 E^2\, e^{-2i\omega t} + c.c.) \tag{6}$$

The above formula contains two parts – the first term is at zero–frequency contribution and the second term at 2ω frequency contributes to the second-order polarization, which leads to the formation of the second harmonic generation.

Second harmonic generation phenomena can be illustrated as an exchange of photons between various frequency components of the applied field [21]. Two incident photons at frequency ω_i are interacting within the material (**Fig. 2.1**), and when effectively combined they form a new photon of double the original energy (2ω) in a single quantum-mechanical process following the conservation of energy. A virtual state is a quantum state that cannot be observed as it is short-lived. The response time of SHG is at the femtosecond level ~ 10^{-15}s.

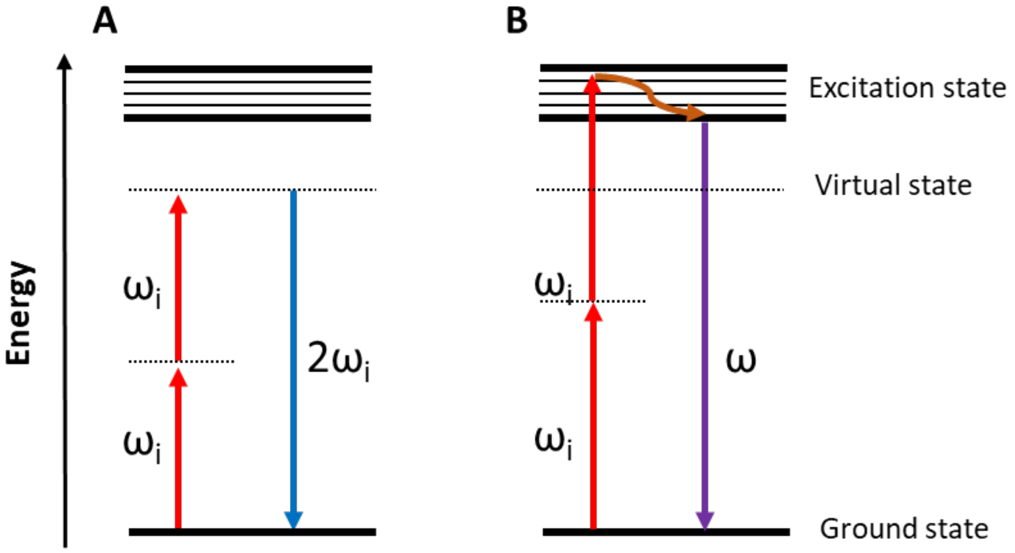

Figure 2.1 Photon energy diagram of two multiphoton processes; **(A)** in second harmonic generation (SHG) two incident photons ω_i of lower energy are combining to generate new photon with double of the incident frequency; **(B)** in two-photon fluorescence (TPF), two photons are excited to the excitation state by the simultaneous absorption.

The process must not violate energy and momentum conservation. Energy conservation implies that $\omega_i = 2\omega_s$, while from momentum conservation arrives the phase-matching condition [4]:

$$\overrightarrow{k_s} = 2\overrightarrow{k_\iota} \tag{7}$$

Where ω_i and ω_s are the frequencies of the incident and scattered photons, and k_i and k_s are their wavevectors, respectively.

The SHG signal is proportional to the square of the excitation power in such a way that:

$$I_{SHG} \propto |P^{(2)}(2\omega)|^2 \propto I_{exc}^2 \tag{8}$$

2.1.2 Two-Photon Fluorescence

Two-photon fluorescence (TPF) involves a two-photon absorption process. Two NIR photons of the same energy that match the energy gap between the ground and excitation state of the molecule, are excited to a higher energy state by the simultaneous absorption in an atom or molecule within 10^{-18} s to 10^{-16} s (**Fig. 2.2B).** After excitation, the electron relaxes to the vibrational ground state after ~10^{-12} s and then decays to the ground state emitting a photon 10^{-9} s after the beginning of the process [22].

TPF is a nonlinear process and is related to the imaginary part of the third-order susceptibility $I_m \chi_3$. Furthermore, its transition probability depends on the square of the light intensity:

$$I_{TPF} \propto I_{exc}{}^{2} \tag{9}$$

The utilization of the intense laser pulses will increase the average two-photon absorption. When fs laser is applied with 100 fs duration pulses at a 100MHz repetition rate the TPE process will be enhanced even up to 100,000-fold and 10^{10}-fold improvements over a continuous wave (CW) illumination for TPF [23].

One-photon fluorescence (OPF) has a linear relation between light and fluorescence intensity while in TPF the fluorescence signal intensity depends on the square of the number of photons that reach the sample, however, the probability of TPF is much lower than OPF. This is one of the fundamental differences between one- and two-photon fluorescence. In OPF, each plane of the excited volume that is perpendicular to the optical axis has evenly distributed emitted intensity leading to lower resolution and poorer contrast of the image with no optical sectioning in z (**Fig. 2.2A** and **B**). The solution comes with an implementation of the pinhole that rejects all out-of-focus light right before the detector. In TPF, moving further from the focused point causes a reduction in emitted intensity as $1/z^2$ meaning the emission occurs in the very concentrated region on the sample (**Fig. 2.2A**). The technique is often called “intrinsically confocal” due to no need for a pinhole in the system.

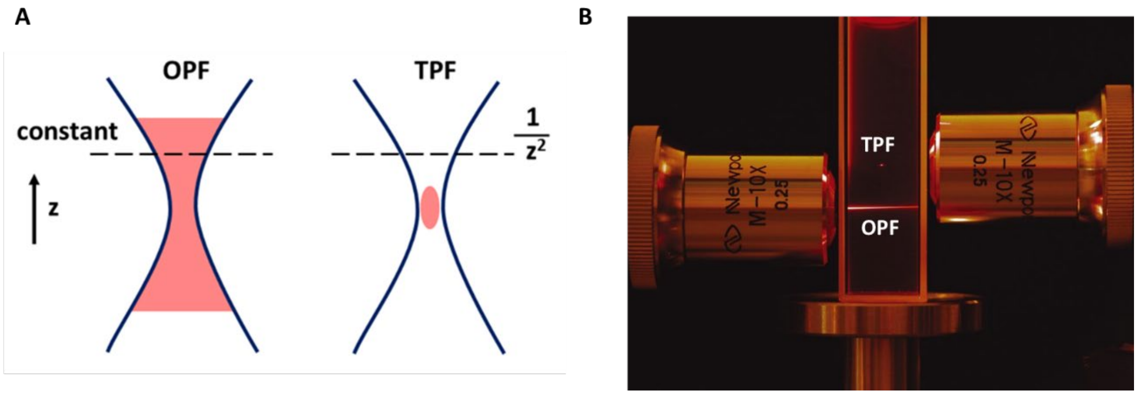

Figure 2.2 (A) Size of the excited volume in one-photon fluorescence (OPF) (left) and two-photon fluorescence (TFP) (right). In OPF, the emission is evenly distributed leading to the need for a pinhole to remove the out-of-focus signal. In TPF, the fluorescence emission is generated at the laser focus and out-of-focus light decreases as $1/z^2$ where z is the direction of the plane; **(B)** Comparison of OPF (lower beam) and TPF (upper beam) in a fluorescent dye cell (Adopted from https://www.newport.com/n/two-photon-microscopy).

TPF often uses NIR light for excitation that gives a better sample penetration depth, less tissue photo-damage, and less scattered light than for visible light used in OPF.

2.1.3 Biomedical Applications of Second Harmonic Generation and Two-Photon Fluorescence

SHG and TPF are label-free imaging techniques that do not require invasive staining and processing of the samples. The subcellular resolution and molecular specificity make multiphoton microscopy (MPM) suitable imaging modalities in many biomedicine applications, for example, in the improvement of the current cancer detection methods. Currently, diagnosis of cancer relies on histopathology, which evaluates morphological and molecular abnormalities in the tissue section [24]. In this process, the tissue is extracted in the process of biopsy that may introduce a risk of damage, especially in neurological tissue. Then, it undergoes several hours of histology sample preparation, in which the sample is fixed and stained with hematoxylin & eosin (H&E) before being examined by the pathologist. The process is not only time-consuming and labour-intensive, but due to *in situ* nature it introduces sampling error. The accuracy of diagnosis is further limited by the inability to compare tumour tissue with its healthy counterpart.

Multiphoton microscopy has the potential in improving cancer diagnoses by offering real-time imaging with no need for sample staining and sectioning. It uses near-infrared wavelengths that are less damaging to tissues and can achieve a deeper penetration range than in visible light [25, 26]. Such imaging modalities could be employed for intra-operative surgical guidance system, in which tumour margin detection could become rapid, real-time and at least minimally invasive. Hence, miniaturization and portability of the bulky, laboratory MPM setup to fit the clinical environment is a key requirement for translation.

TPF and SHG are generated by separate sources in biological tissue, cells, and extracellular matrix. NAD(P)H, flavins, retinol, tryptophan and elastin are the main sources of fluorescence emission [27], while collagen, which is the most abundant protein found in the human body [28] generates a strong SHG signal [4].

In disease diagnostics, reduction in SHG signal indicates lower collagen content and changes in its structure [5-7]. A quantitative analysis of the alignment of the collagen fibres in prostate cancer [8] or reduction in density and ordering of collagen fibrils in breast, bone, and skin cancers was used as a powerful diagnostic tool [9].

Similarly, TPF has been used in diagnosis of cancer in the skin [10], gastrointestinal tract [11], lungs [12], and colon [13]. In neuroscience, the characterization of intact neural tissues with TPF has been reported [29].

2.2 Hollow-Core Fibre for Endoscopy

An optical fibre is a cylindrical dielectric waveguide that operates at optical frequencies and is fabricated with transparent silica glass or plastic. It consists of the three main components – core, cladding, and jacket (**Fig. 2.3**). The light is guided through a core that is the most central part of the fibre and is embedded by the ring of a glassy layer called cladding.

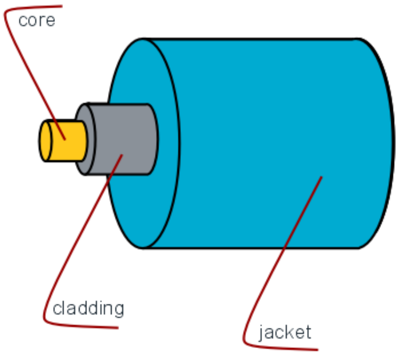

Figure 2.3 Structure of the optical fibre. It contains a guided light core in the centre, a layer of cladding, and a plastic jacket to help confine the signal inside the core and to protect fibre.

In the case of a classical structure, when a signal propagates along the core of the fibre, the presence of cladding is not necessary. However, for sufficient signal guidance in the core, an additional sheet of supporting material, that is, the cladding is required. Furthermore, cores without cladding in a fibre bundle can experience information crosstalk among one another. Finally, the outer part of the fibre, a jacket, is a coating made of an elastic-plastic buffer that gives further protection to the fibre and helps sustain light confinement in the core. [30].

2.2.1 Solid Core Fibre

The solid core fibre is entirely made of glass or plastic [31]. Light propagates in solid fibre based on the total internal reflection (TIR) phenomenon (**Fig. 2.4**).

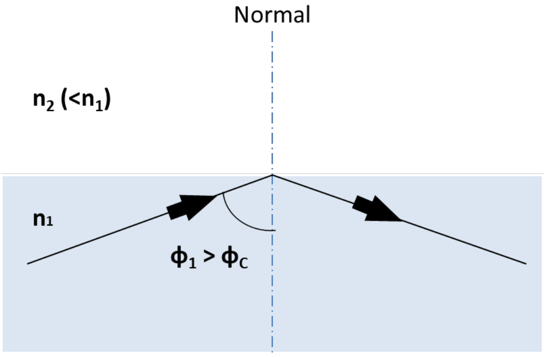

Figure 2.4 Process of total internal reflection. When the angle of incident φ_1 is greater than critical angle φ_c, the total light is reflected back into the original material with refractive index n_1 and does not enter the new material (refractive index n_2).

If the angle of incidence φ_1 of an incoming ray is greater than the critical angle φ_C, there is no refracted ray and all incident energy remains inside the propagation medium [31]. The light will undergo TIR inside the fibre bouncing back and forth off the edge between the core and cladding because the incident angle will be equal to the reflection angle so the light continues to be reflected. In order for TIR to happen, the incident ray has to enter the fibre at the minimum angle $\varphi_{min} > \varphi_C$ which can be determined from Snell's law [30]:

$$\sin\phi_c = \frac{n_2}{n_1} \tag{10}$$

where n_1 and n_2 is the refractive index of core and cladding. Refractive index is a dimensionless magnitude that describes how the light propagates in a given medium, and its value depends on materials. It can be calculated from:

$$n = \frac{c}{v} \tag{11}$$

where c is the speed of light in free space and v stands for the velocity of light in a given medium.

To sustain light propagation inside the core, the contrast in the refractive index between the core (n_1) and the cladding (n_2) is created by doping the silica glass with germanium so $n_1 > n_2$ [31].

An important parameter for optical fibres is its numerical aperture (*NA*) [31], which determines the maximum capacity angle for accepting and gathering the light, and is expressed by:

$$\boldsymbol{NA = \frac{1}{n_0}\sqrt{n_{core}^2 + n_{cladding}^2}} \tag{12}$$

n_0 is the refractive index of the medium around the fibre, which is close to 1 for air.

Solid core fibre can operate as a single or multimode waveguide [31]. The *V* parameter defines a number of modes that a fibre can guide.

$$\boldsymbol{V = \frac{2\pi a NA}{\lambda}} \tag{13}$$

For a core radius a, if $V < 2.405$ fibre operates as a single-mode and if $V > 2.405$ fibre operates in higher-order modes.

Solid core fibres can be categorized based on their structural differences [31].

a) Step – index single mode fibre (typical value) - Core diameter: 8 -12 µm/Cladding diameter: 125 µm

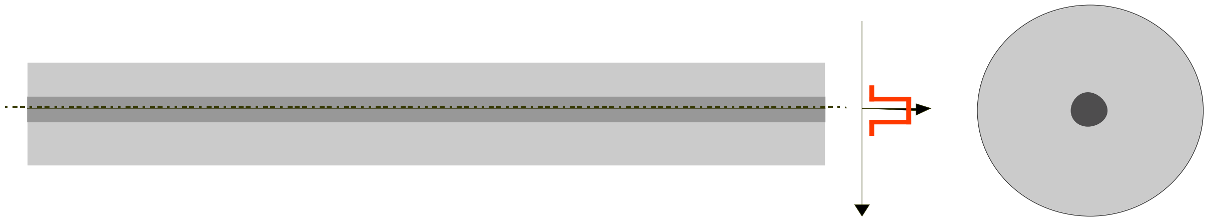

Figure 2.5 Ray path and cross-section in step-index single-mode fibre. It is characterized by a sudden change in the refractive index value at the transition point between core and cladding.

The refractive index shows uniformity for the whole length of the fibre, with a sudden change (like a step) at the cladding edge (the one proximal to the core). Due to a small core size, the fibre can support only one mode of propagation. Step-index, solid-core fibre is mostly used in long-distance communication and in optical sensors.

b) Step – index multimode fibre (typical value) - Core diameter: 50 - 200 µm/Cladding diameter: 125 - 400 µm

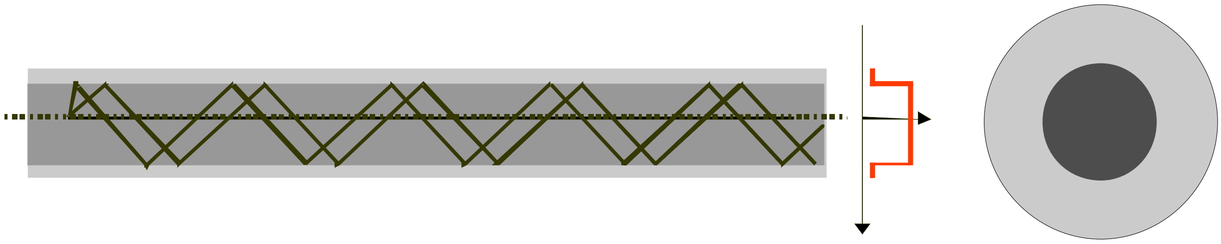

Figure 2.6 Ray path and cross-section in step-index multimode fibre. It is characterized by a sudden change in the refractive index value at the transition point between core and cladding.

This type of fibre is similar to the single-mode, although, the core diameter is larger thus it supports a higher modes number (**Fig. 2.6**). The larger core size allows for an easier optical power launching and facilitates the connection with similar fibre. However, the disadvantage of multi-mode fibre is intermodal dispersion, which causes different light rays to travel with different velocities resulting in various arrival times.

c) Graded - index multimode fibre (typical value) - Core diameter: 50 - 100 µm/Cladding diameter: 125 - 140 µm

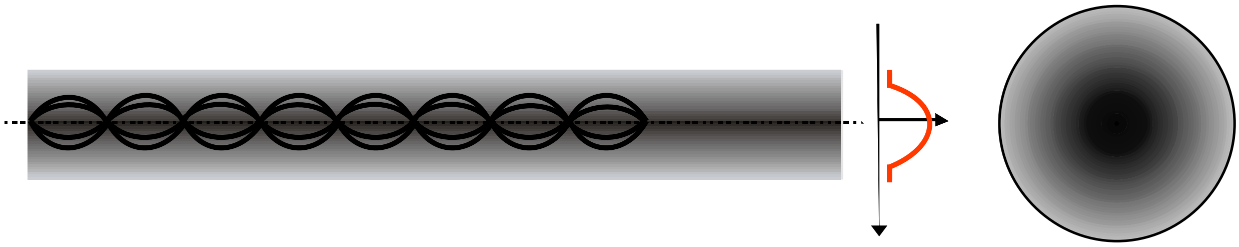

Figure 2.7 Ray path and cross-section in graded-index multimode fibre.

In this multimodal structure (**Fig. 2.7**), the refractive index will gradually decrease when moving away from the main axis of the fibre. This results in an increase in velocity of pulses with radial distance from the fibre axis (opposite to a decrease in the refractive index) and a reduction of the intermodal dispersion so that the travel time of different modes will be equalized [32].

In the 1990s, a new class of a solid core waveguide, Photonic Crystal Fibre (PCF), was developed by the group of Phillip St. J. Russell [33]. The structure of the PCF (**Fig. 2.8**) has air holes in the cladding to lower its “average” refractive index. The core is made of solid core with a higher refractive index than the surrounding medium.

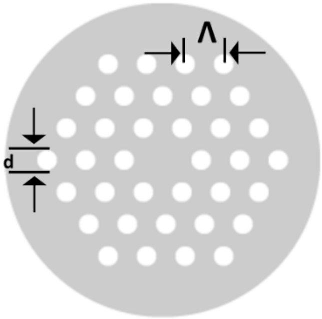

Figure 2.8 Schematic representation of structure of solid core photonic crystal fibre. Amendment of a diameter of capillaries *d* and the hole-to-hole distance *Λ* results in the control of fibre's modality and dispersion.

PCFs guiding properties are based on modified total internal refraction (MTIR). Diameters of the capillaries *d* and hole-to-hole distance *Λ* (or pitch) are important parameters because for $d/Λ < 0.4$, a PCF acts as an endlessly single-mode waveguide [34]. By changing *d* and/or *Λ* value, the dispersion can be controlled. Furthermore, the larger core area lowers the nonlinearity.

Before the discussion on hollow-core fibres technology, important factors that affect high power, ultra-short pulse propagation in solid core fibres and are crucial in fibre selection for multiphoton endoscopy are described below.

2.2.2 Dispersion

Different spectral components of a short pulse propagate with different velocities so that

$$\boldsymbol{\beta_2 = \frac{\partial \beta}{\partial \omega}} \tag{14}$$

where β_2 is a frequency-dependent propagation constant of the fibre that refers to a group velocity dispersion (GVD) parameter [32]. It is often expressed as a derivation with respect to wavelength. The dependence between GVD and dispersion D_λ is as follows:

$$\boldsymbol{D_\lambda = -\frac{2\pi c}{\lambda^2} \cdot \beta_2} \tag{15}$$

The opposite sign of D_λ and β_2 implies that a longer wavelength corresponds to a smaller frequency.

2.2.3 Nonlinearity

Nonlinearity relates to the increasing intensity of the applied electric field so that light interacting with the medium changes its properties but also its own propagation [31]. Another factor that will contribute to the formation of nonlinear effects in fibres is their structure itself [34].

The discovery of the laser has opened a new spectrum of applications for optical fibres. However, increasing laser power has brought nonlinear optical effects into the optical waveguides, which can modify information carrying signal pulses.

As SiO_2 is a symmetric molecule, hence, its lowest order nonlinearity is controlled by the third-order susceptibility $\chi^{(3)}$. Under these conditions an intensity-dependent refractive index (IDRI) $\tilde{n}$ will be:

$$\tilde{n} = \boldsymbol{n_0} + \boldsymbol{n_2 I} \tag{16}$$

where I is the instantaneous intensity of the optical field, n_0 is the linear refractive index, and n_2 in the nonlinear coefficient expressed as:

$$\mathbf{n_2} = \frac{\mathbf{3}}{\mathbf{8n}}\mathbf{Re}(\boldsymbol{\chi}^{(\mathbf{3})}) \tag{17}$$

In silica, $n_2 \approx 2.5 \times 10^{-16}$ cm^2/W.

The nonlinear parameter γ is defined as:

$$\boldsymbol{\gamma} = \frac{\boldsymbol{2\pi n_2}}{\boldsymbol{\lambda A_{eff}}} \tag{18}$$

where A_{eff} is the effective mode area. For typical single-mode fibre, $\gamma \approx 20$ W^{-1} km^{-1} [32].

The IDRI causes a self-phase modulation (SPM) that is concerned with the relation of refractive index and wavelength subject to high-power intensity [32]. Under low-power intensity, the refractive index of the material remains intact. However, growing power intensity will change the refractive index to a small degree, which is then multiplied over a long distance of fibre, and increased significantly. Eventually, by modifying the refractive index of the medium, a propagating pulse will experience changes in its phase, which depends on the refractive index of the medium.

SPM generates a nonlinearity phase shift ϕ_{NL} on the propagation pulse:

$$\Phi_{\boldsymbol{NL}} = \boldsymbol{n_2 k_0 L I} \tag{19}$$

The maximum phase shift that happens at the centre of the pulse after propagating distance z, is given by:

$$\Phi_{NL,max} = \gamma P_0 z \tag{20}$$

where P_0 is the peak power of the pulse.

Nonlinearity and dispersion can be responsible for the temporal and spectral modification of the pulse. The travel of the pulse in HCFs is comparable to free space light propagation, hence GVD and SPM have a very small effect on pulse spreading [35].

2.2.4 Nonlinear Pulse Propagation

Propagation of an ultra-short pulse with width ranging from ~ 10ns – 10fs, is described by Nonlinear Schrödinger (NLS) equation [36].

$$i\frac{\partial A}{\partial z} + \frac{i\alpha}{2}A - \frac{\beta_2}{2}\frac{\partial^2 A}{\partial t^2} + \gamma|A|^2 A = 0 \tag{21}$$

where A is a slowly varying amplitude of the pulse envelop. NLS equation describes changes in the pulse in time at a given distance under the effect of GVD (β_2), SPM (γ) and fibre losses (α).

2.2.5 Hollow-Core Fibres

There are three main types of hollow-core fibres (HCFs): hollow-core photonic band gap (HC-PBG) fibres, Kagome type fibres, tubular fibres including an anti-resonance negative curvature fibre (ARF). In HCFs refractive index of the core n_1 is lower than of the cladding n_2 ($n_1 < n_2$), thus the guiding mechanism is different to the conventional solid-core fibres, and it depends on HCF structure. HCFs offer light guidance in air-core making its propagation comparable with the free space transmission so that only up to 1% field propagates in silica material [37]. **Figure 2.9A** shows Kerr nonlinear coefficient as a function of optical attenuation for different fibres. For hollow-core photonic crystal fibre (PCF), the nonlinear coefficient is around 5 orders of magnitude smaller than in standard solid core optical fibre. Furthermore, dispersion in hollow-core PCF is independent from that measured in bulk silica and can be normal and anomalous with the zero dispersion wavelength (ZDW) at the centre of transmission window (**Fig. 2.9B**). HCF can endlessly operate as a single mode.

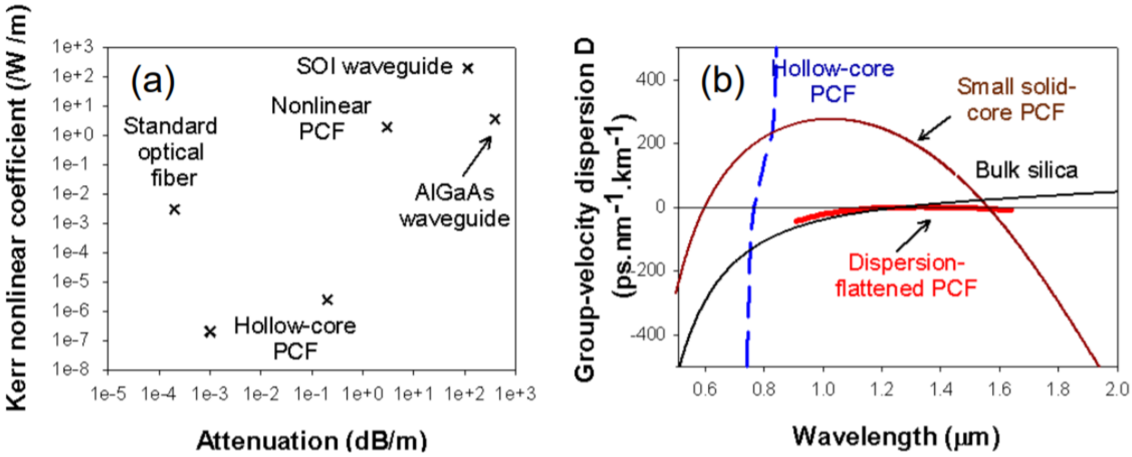

Figure 2.9 Nonlinearity **(A)** and dispersion **(B)** for different type of fibres. Kerr nonlinear coefficient is several orders of magnitude smaller for HC-PCF (**A**); HC-PCF has both normal and anomalous dispersion with the ZDW at the centre of the narrow transmission window (**B**). Adapted from [38].

In HC-PBG fibres, cladding consists of a periodic microstructure with a presence of a photonic bandgap for which light with well-defined wavelength and angles of incidence cannot travel (**Fig. 2.10A**). The total attenuation in HCF fibres is a combination of confinement losses (CL) and absorptive losses, or scattering surface loss (SSL), and losses induced by bending. HC-PBG are characterized by a very low CL due to a weak leakage from the core, and high SSL, which comes from the features of the thin glass struts in cladding microstructure [39]. The guidance in HC-PBG is intrinsically narrowband (typically < 100 nm) which puts limitations on their applications [40].

Kagome type fibres have larger losses (< 5 dB/m) than PBG fibres, but the low-loss transmission window is much broader (> 400 nm) [41]. Its periodical air/glass micro-structured cladding differs from HC-PBG and has a pattern that resembles a Star of David (**Fig. 2.10B**). The guiding mechanism in this fibre is based on the same principles as in tubular fibres, and it will be described in more detail in section 2.2.6.

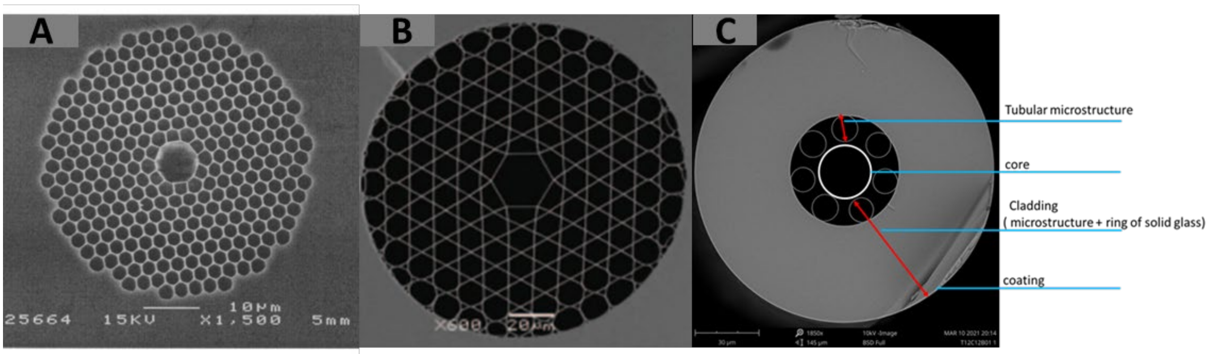
A
25664 15KU X1,500 10µm 5mm
B
X600 20µm
C
Tubular microstructure
core
Cladding
(microstructure + ring of solid glass)
coating

Figure 2.10 SEM micrographs of different hollow-core fibres; **(A)** A HC-PBG fibre [42]; **(B)** a Kagome lattice HC fibre [43]; **(C)** negative curvature anti-resonant hollow-core fibre (ARF), it contains a hollow- core in the centre, cladding (micro-structure with the ring of glass, and coating).

2.2.6 Anti-Resonant Negative Curvature Hollow-Core Fibre

The fibre investigated for nonlinear, label-free endoscopy in this work is a negative curvature anti-resonant hollow-core fibre (ARF). Its structure has three main components (**Fig. 2.10C**):

- Boundless hollow-core in the centre
- Cladding with a band of solid glass ring and a row of hollow capillaries (micro-structure) at the appropriate distance from one another
- Protective coating (not visible on the picture due to cleaving procedure)

ARF has a simple structure compared to other HCFs (**Fig. 2.10**), does not have a periodic cladding and its guiding light mechanism is not based on a photonic bandgap, which explains its leaky nature. There are close similarities between ARFs and Kagome fibres in multiple transmission bands and similar attenuation values at comparable wavelengths [35]. ARFs inherently have higher loss than HC-PBG fibres, broader transmission window and their main loss mechanism originate from CL (**Fig. 2.11**) [39].

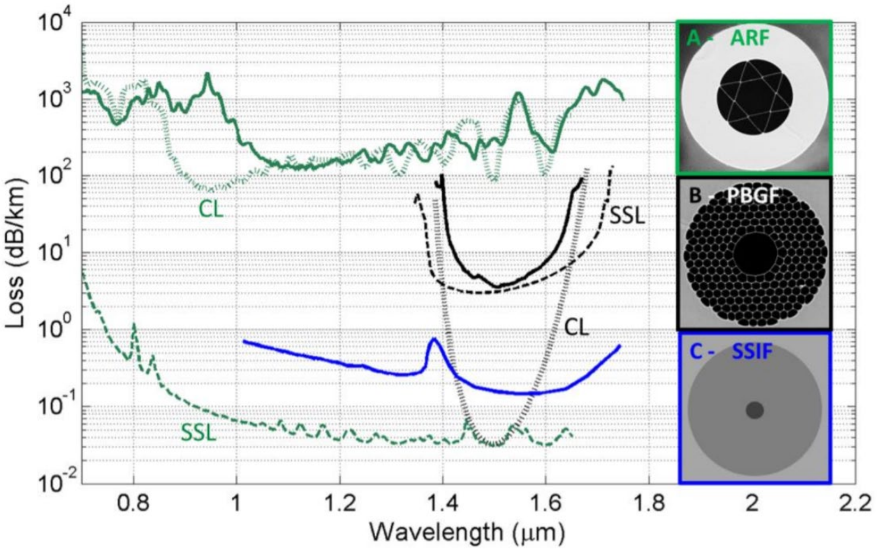

Figure 2.11 Attenuation comparison for three types of fibres: anti-resonant **(A)** photonic bandgap **(B),** and solid core **(C)**. The graph presents different sources of losses and CL – confinement loss, SSL- scattering surface loss. The solid line is measured data, while dotted/dashed lines are simulated data. The dominated losses in ARFs come from CL, while in PBGF from SSL [39].

Inhibited Coupling and ARROW Model

There are many similarities between Kagome and ARFs, in fact ARF appears like a simplified version of Kagome. When Kagome cladding is reduced to a single layer structurally, it becomes comparable with ARF. There are many views in the fibre optic community that the guiding mechanism of those two types of fibre is based on inhibited coupling (IC) and the anti-resonant reflection optical waveguide (ARROW) model.

In the IC, a strong mismatch between a high degree transverse field of core and cladding modes inhibits a coupling between them [44]. On the other hand, in the ARROW model, the cladding of the fibre is an array of high and low refractive index layers (**Fig. 2.12**) like in a Fabry – Perot (FP) resonator [44].

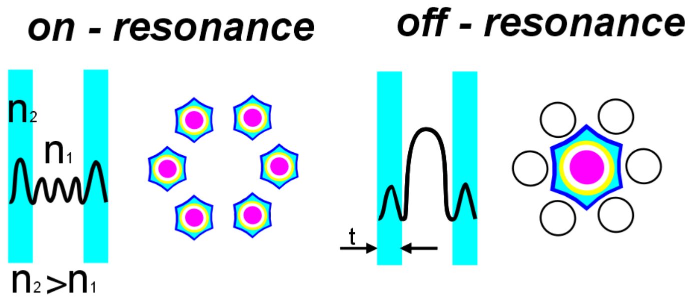

Figure 2.12 Principle of ARROW guidance, when the propagated light is in on resonance and off-resonance state.

In the resonance state, the light in the FP cavity interferes constructively with itself, leading to high transmission in the cladding. In the off-resonance state, cladding layers in the FP resonator experience destructive light interference, so the light will be strongly confined in the core of the fibre where the refractive index is at the lowest magnitude. In ARFs, light propagates in the core at the low-loss wavelengths and is in anti-resonance with the glassy tubes of the cladding, which causes very low SSL (**Fig. 2.11**).

One of the first designs of ARFs had cladding nodes, which were contact points between adjacent tubes [35]. They highly contributed to CL due to acting as independent and high lossy waveguides that reduced light confinement in the core. Presently, ARFs are fabricated with non-touching capillaries to avoid the creation of additional resonance and decrease CL [39].

In ARFs, the thickness of the capillaries controls the operational spectral region. The wavelength $\boldsymbol{\lambda_r}$ of the resonance corresponds to the thickness of capillaries, and it can be determined using the following formula:

$$\boldsymbol{\lambda_r = \frac{2t}{m}\sqrt{n^2 - 1}} \tag{22}$$

$\boldsymbol{m}$ is an integer related to the number of resonance, $\boldsymbol{t}$ is the thickness of the membranes. The refractive index $\boldsymbol{n}$ around the core and size of the tubes $\boldsymbol{t}$ can define the operational wavelength $\boldsymbol{\lambda}$ that propagates inside the core and is located in the middle of resonance λ_r-s of the fibre [35].

Dispersion and Nonlinearity

The hollow-core structure of ARFs affects the magnitude of nonlinearity and dispersion. The light is guided in air (or a gas), a non-dispersive medium, hence results in negligible material dispersion. ARFs are characterized by very low group velocity dispersion of <2.5 ps/nm/km across the whole transmission window [18]. ARFs do not experience intermodal dispersion because after a few 10-s of meters it shows fundamental mode purity and higher-order mode suppression [18].

The nonlinearity of ARF originates from the air inside the core and part of the cladding material. Kerr nonlinearity for air is three orders of magnitude lower than for silica. There is limited overlapping between core and cladding modes which reduces material nonlinearity to almost zero [35]. Furthermore, ARF's design has a Large Mode Area (LMA) that decreases a photon density and induction of nonlinear effects [18].

Future of ARFs and Their Applications

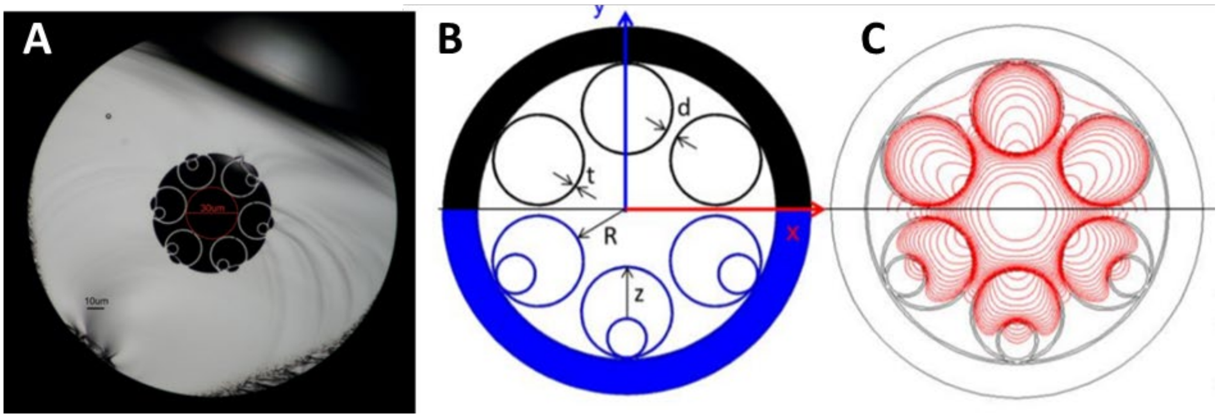

Figure 2.13 Optical microscope image of NANF cross-section **(A)**, comparison between ARF and NANF: structural **(B)** and confinement loss (CL) **(C)**. NANF has additional tubes that decreased CL [39].

The confinement loss (CL) in ARFs has been further reduced by adding additional nested tubes of the same thickness as the outer capillaries (**Fig 2.13A, B**) [39]. As the light is stronger confined in the core, leakage modes are decreased so the CL (**Fig. 2.13C**). The new structure is named Nested Anti-resonant Nodeless Fibre (NANF). The most recent NANF was fabricated in Prof David Richardson's group from the ORC Southampton University with a loss of 1.45 ± 0.15 dB km^{-1} at 850 nm and transmission spectrum 600 – 1100 nm [45]. The large spectral transmission range can be ideally suited for multiple spectroscopic techniques.

With the progress in anti-resonant fibre technology, ARFs have already found many applications in high power laser transmission [46, 47], gas hollow-core fibre lasers [48, 49], and medicine [50, 51].

Due to a high absorption coefficient of water molecules at 2.94 µm wavelength and mechanical flexibility, an Er:YAG fibre laser was proved a good choice for laser surgery. The HCFs were evaluated for mid-infrared surgical applications [50]. Applying HCFs instead of solid-core fibres in such a systems significantly increases the Laser Induced Damage Threshold (LIDT). The output energy delivery was higher for ARF, however HC-PBG performed better in bend loss experiments. Increasing coupling optimization could prevent HC-PBG from high power damages. In further research, output end of ARF was mounted with a solid sapphire endtip which increased capabilities of the fibre in delivering high power pulses for soft and porcine tissue ablation [51].

2.3 Towards Development of Endoscope for Multiphoton Microscopy

The transition of MPM to the clinical environment can be facilitated by the development of the endoscope probe. Its design must combine features that allow for safe and efficient operation of the miniature imaging device in clinical routine. The most important characteristic of such a probe is its miniature size reduced up to a few millimetres in diameter. Portability and flexibility is required for remote work and capability to enter hard-to-access areas of the body. The operation under the low electric voltage and current with maintaining high optical parameters (resolution, field of view, and frame rate) of the miniaturized device are additional desirable characteristics of its performance. Finally, its construction and operations must be in accordance with appropriate regulation.

2.3.1 Miniaturization

When designing instruments for a busy clinical environment, the restriction of available space imposes a limitation on device dimensions. The operational principles of endoscopy are similar to the lab-based bulky microscopy systems. However, the performance of MPM on the operating theatre will be feasible only by achieving miniaturization, compactness and flexibility of the endoscopic system.

The classification of the miniaturised imaging devices falls into three main categories: (i) portable microscope, (ii) rigid and (iii) flexible endoscope.

Portable Microscope

A portable MP microscope needs to be compact and lightweight and the ability to perform laser scanning imaging. Helmchen *et al.* were the first to demonstrate a TPF microscopy using a miniaturized system on a freely moving animal [52]. The scaled-down optical and scanning parts reduced the dimensions of the device to 7.5 cm long and a weight of 25 g. The study of brain activity in anaesthetized and awake animals using a head-mounted microscope provided data on dendritic morphology and calcium transients in neurons (**Fig. 2.14A**). Remote imaging without compromising the size of bulky optics is offered by a hand-held microscope (HHM), which is a portable, hand-operated device. HHM is less limited by its dimensions compared to the miniature head-mounted microscope described above that required a platform to carry it around.

The HHM prototypes for SHG and TPF for a dermatological applications were reported by Sherlock *et al.* in 2015, and 2018 [53, 54]. Using a single-mode photonic band-gap optical fibre, Sherlock *et al.* constructed a portable mini microscope with an axial motion compensation system for monitoring the position of the sample surface [53]. This device was further improved by employing ARF for free-of-background laser delivery, and a motion correction system that rectified a lateral image distortion created during the examination of living organisms [54].

In situ and *in vivo* chemical identification was achieved by the utilization of customized HHM for stimulated Raman scattering (SRS), which uses two laser beams for excitation (**Fig. 2.14B**) [55]. Lab-built objective lens, with half of the size of its commercial counterpart, helped in reduction of the HHM dimensions. The device was operated in a non-descanned (NDD) configuration that will be described in more detail in Chapter 3. An imaging rate of 8 fps allowed reducing image distortion generated by the movement of the hand.

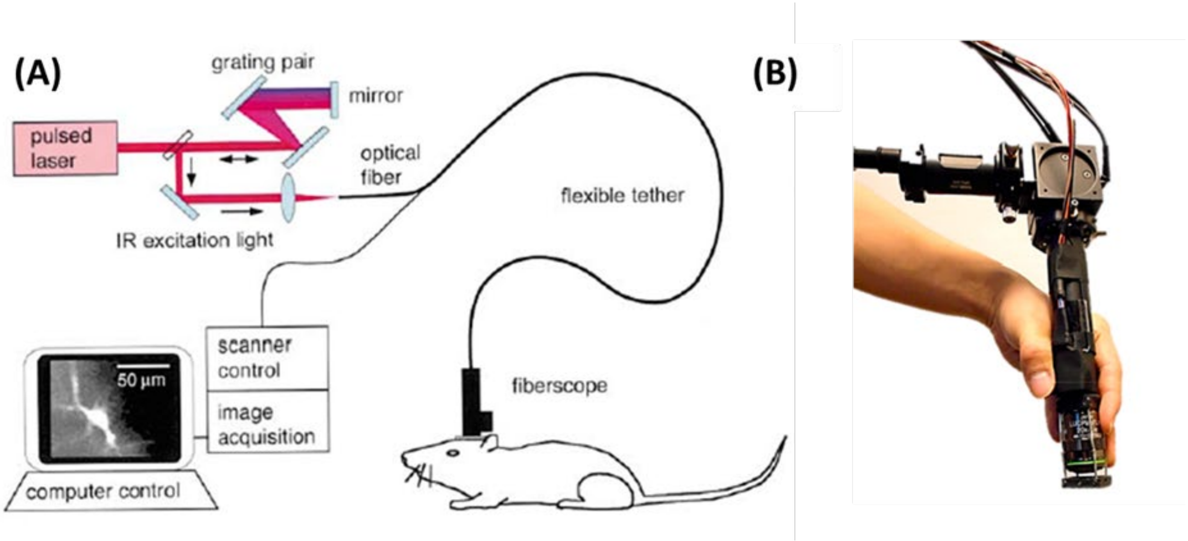

Figure 2.14 Portable microscopes; (**A**) Schematic representation of the setup with a portable microscope for imaging freely moving animal's brain [52]; (**B**) Digital image of a hand-held microscope [55].

Rigid Endoscope

The examination of non-tubular bodily structures like joint space or a cavity does not require instrument flexibility. Maintaining the miniaturization of the device's probe, the laser is directly coupled into the endoscope's head without the necessity for waveguide employment. It offers minimal pulse distortion and deep tissue imaging due to a longer length of the probe with the combination of several GRIN lenses [56]. A rigid endoscope for TPF has been reported with dimensions of 0.9-2.6 cm in length and 350 -1000 µm in diameter [57]. It can serve as an imaging tool for robot-assisted surgery [58].

Flexible Endoscope

An endoscopic probe with fibre can be lightweight and only few millimetres in diameter and thus, can find applications in imaging either epithelial tissue or internal organs such as the gastrointestinal tracts or cervix [56]. Due to its dimensions, it can be incorporated into a traditional endoscope. Its design provides mechanical flexibility and compactness. The endoscopic probe requires fibre for laser delivery, hence, dispersion and nonlinearity compensation methods had to be considered. Integration of a flexible nonlinear imaging micro-endoscope with existing endoscopic systems can make it a potent tool for surgical biopsy and early cancer diagnostics. Flexible endoscope constructions have been tested for SHG and TPF of 2.2 µm fluorescent beads [59], *Griffithsia* sea algae [60], and the rat tail tendon [61].

2.3.2 Portability – Ultra-Short Pulse Delivery

The emergence of pulse laser technology has allowed for nonlinear MPM wherein the signal intensity is inversely proportional to the pulse-width (pico-/femto-second pulses are typically used) [4]. In endoscopy, a laser beam has to be delivered to the sample by means of a waveguide. Fibre optics can guide signals over a long distance and its flexible structure enables easy manoeuvring. When high power, ultra-short laser pulse propagates in the solid core fibre material, it experiences dispersion and nonlinear effects, which change pulse characteristics in the temporal and spectral domain, respectively.

There can also be chromatic dispersion, which is a consequence of that different wavelengths of the pulsed light travel with different velocities and thus result in pulse broadening. It affects a transform-limited pulse by increasing its duration and introducing an instantaneous frequency variation known as a chirp [32]. To compensate for dispersion, the scheme of a pair of gratings for pre-chirping of the pulse has been demonstrated [14-16]. In order to compensate for positive dispersion and slow down the red-shifted leading edge occurring in the fibre, by using pairs of gratings or prisms, laser pulses are negatively chirped before entering the fibre.

Elimination of power-dependent optical nonlinearity in fibre for multiphoton endoscopy has been studied by several groups. One of the proposed solutions was light guidance in a 1 m long fibre so that it did not cause significant changes in the temporal and spectral pulse profile [17]. In another case, the selection of a large mode area (LMA) photonic crystal fibre [49, 50] helped to maintain low spectral broadening effects by decreasing the density of the wave energy.

The challenge in delivering an unaltered laser beam arose for MPM techniques like CARS that require multiple laser wavelengths for excitation. Four-wave mixing (FWM) signal is generated when guided in the fibre and also requires that the Pump and Stokes are temporally overlapped. Hence, both result in a new frequency from the sample. This will cause deterioration of CARS images quality due to the spurious contribution.

In another study Balu *et al.* a large mode area (LMA) fibre was used which helped to lower a high photon density that triggers the SPM process, still FWM signal was 10 times stronger than the collected CARS signal [62]. The excitation light had to undergo spectral filtering using a dichroic mirror before reaching the sample. A similar method was used to block the FWM background by implementing a micro-fabricated miniature optical filter that was attached to the distal end of the fibre [63].

In a different strategy proposed by Wang [64], the Pump and Stokes were coupled into a polarization maintenance fibre (PMF) that maintained the state of polarization (SOPs) of the lasers. The beams interaction was prevented by coupling them orthogonally along the slow and fast axes of the fibre. At the fibre outlet, the original SOP of beams was restored by dual wavelength wave-plate so that their polarizations became aligned. This scheme successfully reduced the FWM signal by up to ~99%.

Dispersion and nonlinearity compensation schemes presented above introduce additional complexity and bulkiness into the system which is not suitable for portability and miniaturization for easy manoeuvring.

The advent of hollow-core fibre technology brought the guidance of high power, ultra-short pulse laser free of dispersion and nonlinearity. Firstly, HC-PGBs were introduced as potential candidates for nonlinear endoscopy [65, 66]. Still, their too narrow spectral transmission window could not accommodate all multiphoton modalities. Tubular fibres are more promising candidates for multiphoton endoscopy due to free-space light guidance and broader transmission window (Section 3.2).

2.3.3 Remote Fibre-based Image Scanning Techniques

Remote imaging techniques can be divided into two main categories: proximal scanning, in which the scanner is placed at the near end of the fibre, and distal scanning in which scanning elements are at the fibre side close to the sample.

Proximal Scanning

In the proximal scanning scheme, the scanning mechanism is positioned at the entrance of the fibre. This is its main advantage since the head of the endoscope probe dimension is defined by the size of the focusing optics located at its distal end. The light intensity information is transmitted from one end of the waveguide to the other by a fibre bundle (FB), which can consist of thousands of step-index fibres accommodated in a tiny area from a few micrometres to millimetres [31]. Light that is coupled into individual fibres' cores, interacts with sample independently, and then the signal is collected backwards through the same fibres' area. Eventually, the final image is created from all points-fibres contained within the bundle. The resolution of the image is determined by the fibre's core size and the core-to-core distance between the waveguides. The downside of this technique is the honeycomb effect generated by the space between the subsequent fibre cores that represent the non-imaged area and contributes to less detailed image quality. To overcome this effect, one could use fibres with reduced cladding dimensions. However, smaller core-to-core separation leads to cross-talk between fibres and to image degradation due to light leakage from one waveguide to another. Additionally, fractured and broken singular fibres within FB may cause non-working/ turned- off pixels and non-signal gaps in the image [67].

Nevertheless, the FBs have been successfully applied in endoscopes for multiphoton microscopy [68-70]. Multimodal FB with a specially designed probe based on gradient-index (GRIN) lenses was proposed by Lukic *et al.* [69]. FB consists of 10,000 light-guiding cores ranging from 2.2 to 3.7 μm (**Fig. 2.15**) was successfully applied to image a skin tissue using CARS/SHG/TPF modalities.

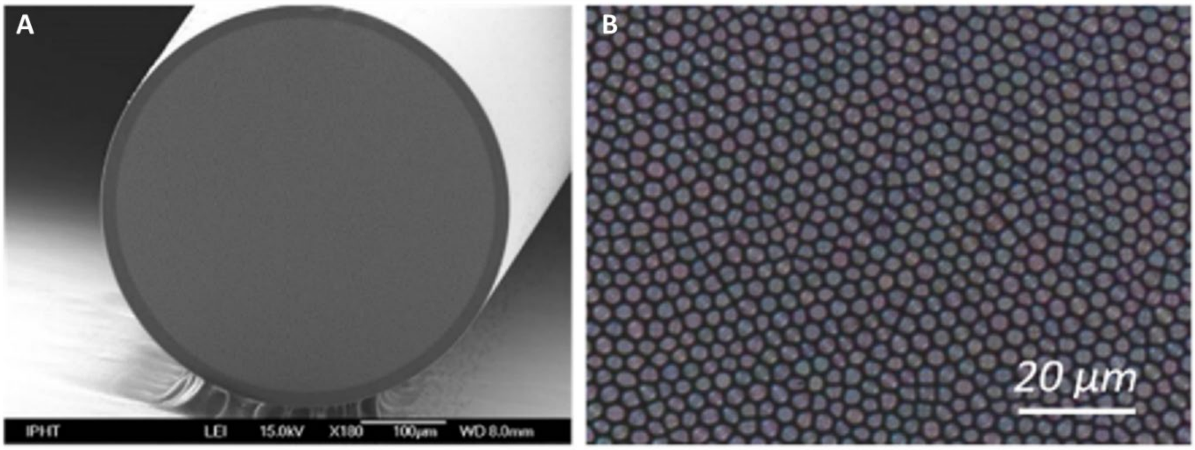

Figure 2.15 Fibre bundle; (**A**) SEM image; (**B**) microscope image with hundredold magnification [70].

Distal Scanning

Distal scanning endoscopy system contains scanner components located at the end of the fibre close to the specimen that allows moving the light over the sample area. The laser beam is either scanned by a set of mirrors or fibre acts as a cantilever beam resonating by means of an actuator. The probe consists of a single fibre for illumination delivery through a core area and a double-clad for signal collection. In some designs, additional fibres are deployed around illumination fibre to receive back-scattered photons from the sample.

Microelectromechanical system (MEMS) scanning mirror allows rapid beam movement over the sample, better miniaturization of the probe thanks to a small size (0.5 mm – 2 mm), high reliability and flexibility of scanning pattern (**Fig. 2.16A, B**). MEMS scanners are fabricated through the material etching and deposition process [61]. They rely on electrostatic or electrothermal actuation and are driven by a low voltage, which can achieve angular rotation up to 30 degrees. They scan the light that emerges from the fibre and guides it to micro-optical components (**Fig 2.16C**). MEMS mirror scanners offer high resolution images however, it increases the probe dimensions. The laser beam, after leaving the fibre, must be collimated before it enters a MEMS-based scanner, then it is focused on the sample. This requires the usage of additional optics. Furthermore, MEMS scanner has to be fixed at an angle to the rest of components in the probe (**Fig. 2.16C**). Nevertheless, applications of MEMS mirrors has been demonstrated in label-free, nonlinear endoscopy for a rat esophagus tissue [71], and chondrocyte [72].

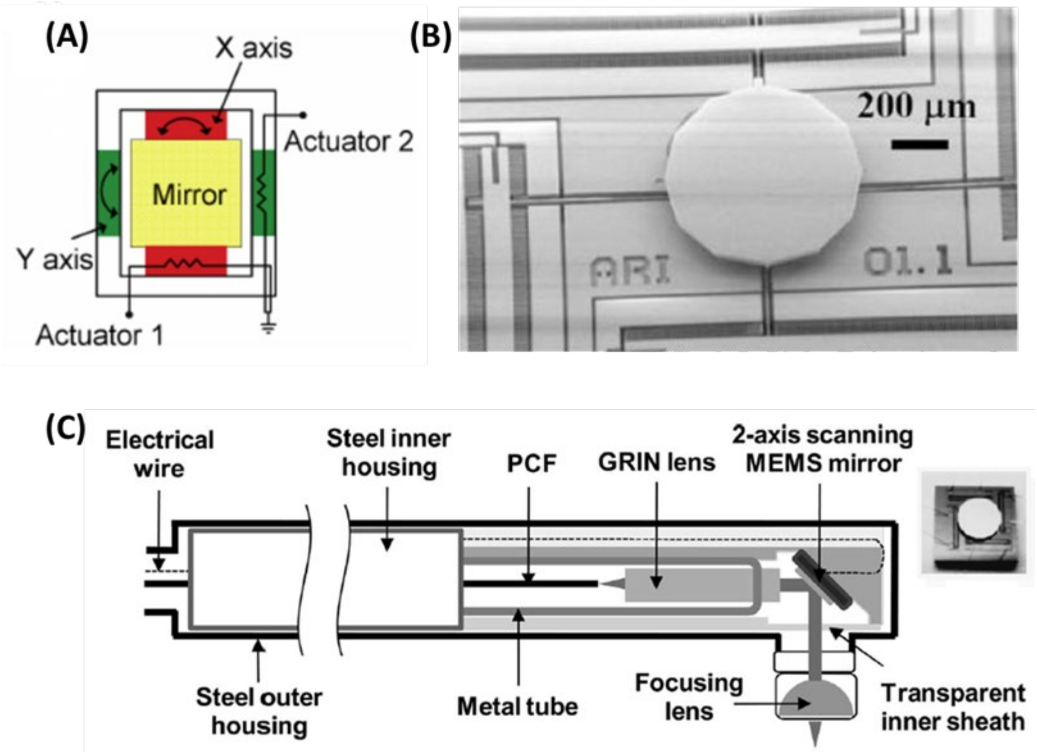
(A)
X axis
Actuator 2
Mirror
Y axis
Actuator 1
(B)
200 µm
ARI
01.1
(C)
Electrical wire
Steel inner housing
PCF
GRIN lens
2-axis scanning MEMS mirror
Steel outer housing
Metal tube
Focusing lens
Transparent inner sheath

Figure 2.16 Microelectromechanical system (MEMS) scanning mirror; (**A**) schematic representation of MEMS [61]; (**B**) a MEMS actuator with a 600µm diameter mirror [73]; (**C**) Location of 2-axis scanning MEMS mirror inside the probe [72].

Piezoelectric-actuator is applied when further miniaturizations of the endoscopic head is needed. Fibre is fixed a few millimetres from its distal end inside the actuator. The protruding part of the fibre acts as a cantilever beam. The whole system should be driven near a mechanical resonance frequency of the fibre end. This will give the highest free-standing fibre tip displacement at a low voltage. Depending on the piezoelectric actuator dimensions, different 2D scanning trajectories can be generated (**Fig. 2.17**).

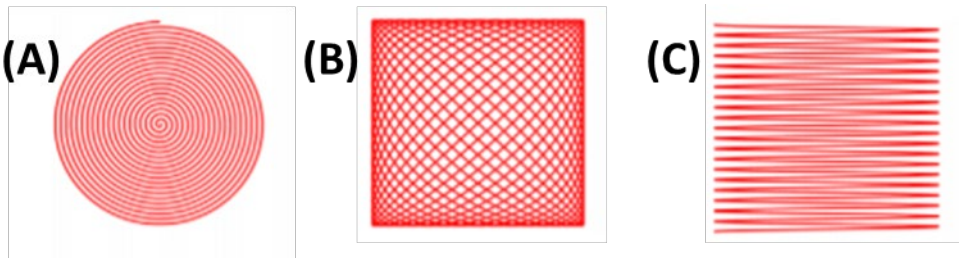

Figure 2.17 Graphical reconstruction of three main scan pattern modes: (A) spiral; (B) Lissajous; (C) raster [74].

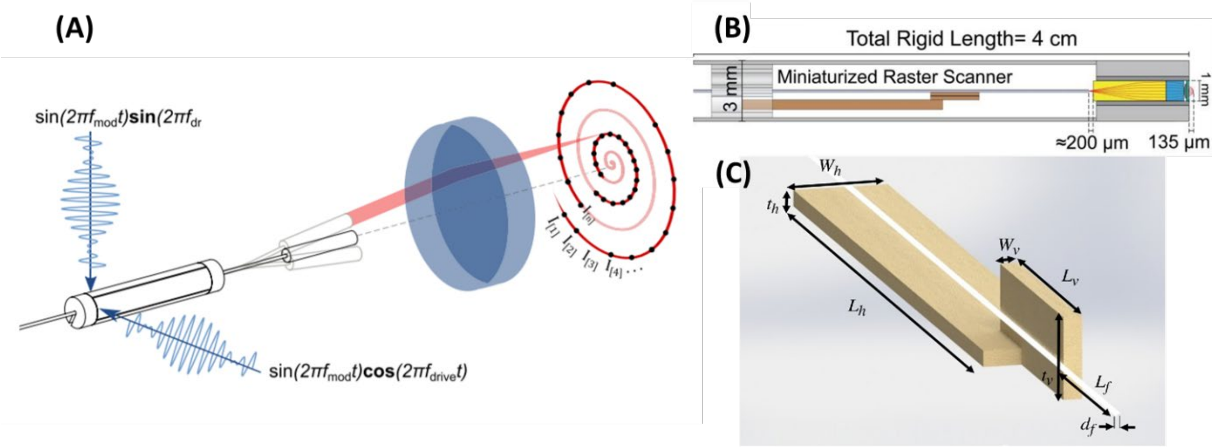
(A)
$\sin(2\pi f_{mod}t)\sin(2\pi f_{dr}$
$\sin(2\pi f_{mod}t)\cos(2\pi f_{drive}t)$
$I_{[0]}$
$I_{[1]}$ $I_{[2]}$ $I_{[3]}$ $I_{[4]}$ …
(B)
Total Rigid Length= 4 cm
Miniaturized Raster Scanner
3 mm
1 mm
≈200 µm
135 µm
(C)
W_h
t_h
L_h
W_v
L_v
t_v
L_f
d_f

Figure 2.18 Various types of piezo actuators; (**A**) tubular piezo scanner based on resonant scan [75]; (**B**) The miniaturized fibre raster scanner driven by high-performance two-layer piezoelectric actuators or bimorphs [78]; (**C**) fibre actuator with two orthogonally placed piezoelectric bimorph cantilevers for a multiple-pattern generation [74].

The generation of the spiral scan (**Fig. 2.17A**) is accomplished by a tubular quadratic piezoelectric scanner (PZT) with two pairs of electrodes that are driven with two independent amplitude modulated sine waves at 90° phase shift (**Fig. 2.18A**) [75]. Due to the geometrical similarity between fibre and cylindrical PZT, identical resonance frequencies are used in the generated spiral scan which makes this method easy and straightforward in adaptation. Its main drawback is non-uniform scanning density along a radial axis of fibre displacement [74]. Lissajous pattern (**Fig. 2.17B**) characterized with a higher scan regularity can overcome this issue. Generating a Lissajous scan with PZT [76], however, is a more complex process than spiral scanning as it requires two resonance frequencies for each axis. However, it helps to remove photodamage that can appear at the centre of the image, caused by oversampling, during spiral scanning mode.

Raster scan (**Fig. 2.17C**) can prove advantageous over a spiral and Lissajous scan pattern due to its uniformity and pixel dwell time throughout the sample [74]. Do et al. accomplished non-resonant fibre raster scanning by controlling scanning speed and scanning area by adjusting PZT actuator driven voltages [77]. Rivera *et al.* achieved raster scanning by orthogonally attaching two piezoelectric bimorphs to a fibre, which was driven resonantly in the fast lateral axis and non-resonantly in the slow vertical axis (**Fig. 2.18B**) [78]. This solution requires a much higher operation voltage for the non-resonant fibre deflection direction than the resonant direction. Tekpinar *et al.* presented a piezo actuator of analogous geometry to Rivera's scanner (**Fig. 2.18C**) [74]. However, they performed all three fibre scan patterns with one device that facilitated an easy switch between the scan modes depending on imaging requirements.

2.3.4 Nonlinear Multiphoton Endoscopy

The advance in the development of micro-scanning imaging devices has allowed for the implementation of nonlinear multiphoton endoscopy for examination of biological tissue. A few examples of its application are presented in this section.

Miniature high-speed (3.3 frames per second (fps)) PZT scanning head with a conventional double-clad fibre made the entire endomicroscopy system a plug-and-play unit that is ready to work immediately upon its connection to computer [79]. However, to compensate for the temporal pulse broadening, a HC-PBG fibre was used for negative prechirping. The system obtained SHG imaging of rat tail tendon and depth-resolved TPF imaging of rat oral tissue stained with acridine orange. Although the system is still in the experimental stage it could be a potential tool for direct visualization of collagen-related diseases.

A custom-made air-silica double-clad photonic crystal fibre was implemented with a PZT scanner to conduct an *in vivo* study of a healthy rat kidney [80]. **Figure 2.19A, B** presents SHG (in green) and TPF (in red) images of the collagen of the capsule and the intracellular flavins of epithelial cells of the kidney tubules with different FOV (scale bars 50 µm) and 30 mW power on the sample. The system performed depth -resolved imaging inside the tissue with a high frame rate of 8 fps in an *in vivo* study.

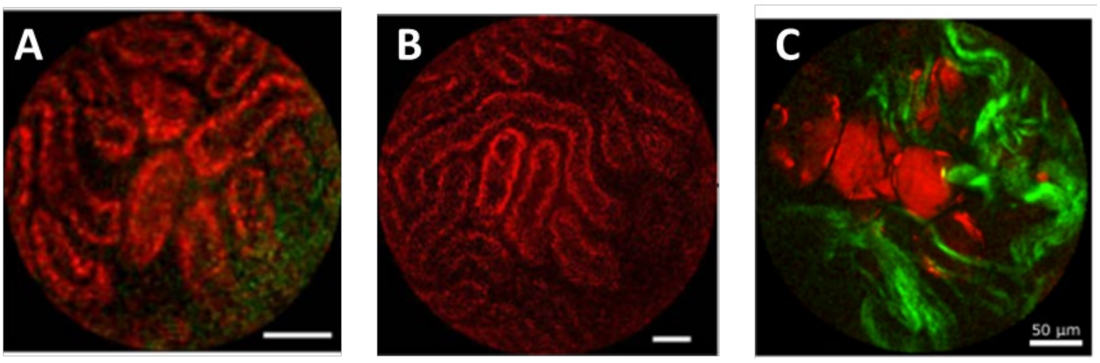

Figure 2.19 Multiphoton endoscopy; (**A, B**) Label-free in vivo examination of rat kidney with SHG (green) and TPF (red). Images (**A, B**) presents the different size of FOV. Scale bars 50 µm. [80]; (**C**) images of human colon SHG (green), CARS (red) pump/stocks power P = 20/10 mW, SHG power P =60 mW [81].

Examination of a human colon using PZT based endoscope with double-clad Kagome fibre was tested by Lombardini [81] (**Fig. 2.19C**). The images illustrated a good signal level of SHG and CARS and required no need for sample staining. The system benefits from distortion-free laser delivery and epi (backward) signal collection by implementing a hollow-core fibre with custom designed cladding area for bidirectional light transmission. Although DC Kagome fibres overcome pulse alteration arising from dispersion and non-linearity, its fabrication can be laborious due to complex microstructure.

2.4 Conclusions

This chapter introduced a fundamental theory that underlies nonlinear, label-free multiphoton microscopy and hollow-core fibre technology. Thanks to properties like label-free, subcellular resolution, and molecular specificity, MPM is a powerful tool that is used in the study of biological material. The ability to perform it in a clinical environment would revolutionize the examination of the tissue samples for many diseases. However, the key to the transition of bulky, laboratory equipment to that suitable for the clinic or an operating room requires the miniaturization and portable operation of endoscopic instrumentation. Furthermore, for the excitation of multiphoton processes distortion-free pulse laser is required to be delivered to the sample. This chapter described the main characteristics that need to be considered for building an optical fibre-based micro-endoscope device for MPM. The next Chapters will show the implementation of these requirements through the construction of a hand-held microscope and an endoscope with a double-clad ARF, new type of hollow-core fibre.

Chapter 3 Fibre Optics for Label-free Multiphoton Endoscopy

3.1 Introduction

Optical fibre selection for label-free, multiphoton endoscopy (MPE) is governed by its capacity to deliver high-power, ultra-short pulse to the sample with as close to the original characteristics of a laser beam. The goal is to achieve a distortion-free pulse transmission in fibre near to free-space propagation. As described in Chapter 2 (2.2.2 and 2.2.3), dispersion and nonlinear processes change features of the ultra-short pulse propagating in the solid core fibre leading to weaker excitation on the sample. Hollow-core fibres can be a promising replacement for their solid-core counterparts for MPE application by recreating free-space propagation conditions inside the core. This chapter presents the study on the suitability of new generation hollow-core, tubular, double-clad anti-resonant fibre (DC-ARF) for nonlinear label-free endoscopy. The effect of DC-ARF on high-power ultra-short laser pulse properties are investigated in a series of tests such as polarization, autocorrelation, nonlinearity, beam quality factor M^2, and attenuation. Furthermore, this section contains the comparison of DC-ARF performance with single-clad anti-resonant fibre (SC-ARF), which has a similar geometry as the DC-ARF, and single-mode solid core fibre (SCF) based on nonlinear effects, dispersion and SHG imaging in different signal collection configurations.

3.1.1 Aim and Objectives

Aim: To establish the suitability of new hollow-core fibre DC-ARF for nonlinear, multiphoton endoscopy.

Objectives:

1. Characterization of DC-ARF for its NA, transmission, and bend loss.
2. Comparison of DC-ARF with two waveguides (solid core fibre, single-clad ARF) in a series of tests like transmission, spectral broadening, dispersion, and imaging to determine their suitability in multiphoton endoscopy.

3.2 Characterisation of Double-Clad Anti-Resonant Fibre

DC-ARF is a promising candidate for nonlinear endoscopy (***Table 1***, **Fig. 3.1**). DC-ARF, which cross-section is presented in **Figure 3.1A**, contains a hollow core surrounded by seven capillaries and a ring of glass that construct the cladding section of the fibre.

The DC-ARF was designed and produced in the ORC Southampton University in a stack and draw fabrication method [31] using Heraeus F300 high purity fused silica glass tubes, and then coated by applying a low refractive index (n = 1.376 at 852 nm) polymer jacket, PC-373-AP. The main function of the coating is to protect the fragile glass fibre from damage. Therefore the majority of waveguides with the capacity to confine the light in the core area are coated with a high refractive index plastic jacket that allows the light coupled to the cladding to radiate out and is less expensive. Since the DC-ARF's design was customized to match nonlinear endoscopy requirements, the fibre was coated with the low refractive index jacket to create the contrast with the cladding and gives the cladding the capacity to transmit the signal. This results in DC-ARF capability to guide the light in the core by glass anti-resonances (section 2.2.6) and cladding area based on total internal reflection (TIR) (section 2.2.1) (**Fig. 3.1A**). Hence, by mimicking conditions prevailing in free space, the hollow-core delivers undisturbed laser pulse to the sample and the cladding collects backward sample emission due to its large surface area (12700 μm^2) and high NA. Furthermore, the implementation of a single waveguide for bi-directional (sample excitation and signal collection) operation allows for better miniaturization of the micro-endoscopic system. **Figure 3.1B** shows the optical images of light confined solely in the core and cladding of DC-ARF.

DC-ARF component	Diameter
Core	**26.3 ± 0.3 μm**
Membrane thickness	**349 ± 8 nm**
Tube spacing	**4.5 μm**
Glass inner cladding	**49.5 μm**
Glass outer cladding	**137 μm**
Total with coating	**279 μm**

Table 1. Measured geometry of the DC-ARF main components.

The NA of the core of 0.029 was experimentally measured using a scanning-slit optical beam profiler (B2 290 -VIS, Thorlabs). The light was launched into the DC-ARF core and for a known distance the output beam diameter at 1/e^2 of the maximum intensity was determined. The literature reports similar NA results for tubular fibres such as 0.036 for a 22 μm core diameter fibre [82] and 0.038 for a 15 µm core diameter fibre [46]. The NA of the cladding was determined to be 0.45 and it was calculated from the refractive index difference between core and cladding (formula 12).

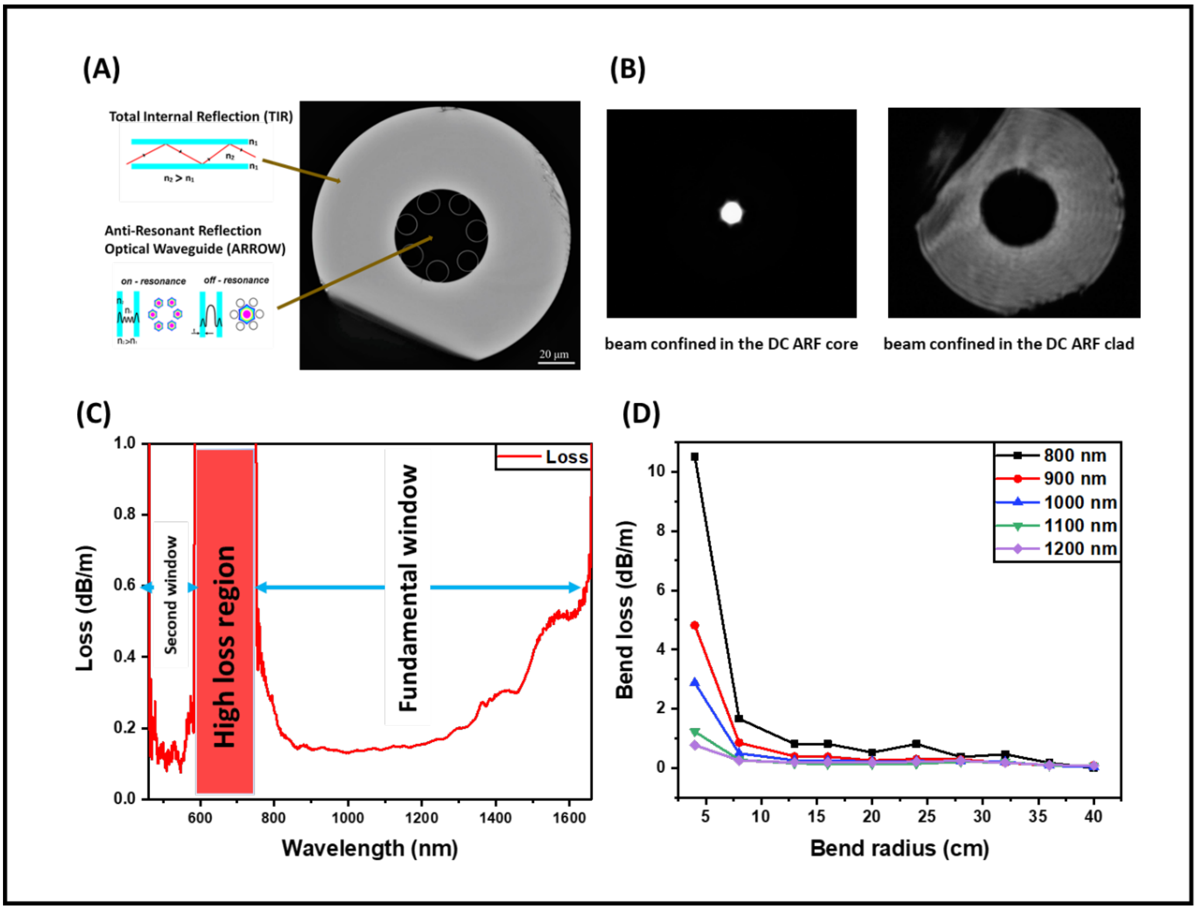

Figure 3.1 DC-ARF with its transmission and bend loss characterization; **(A)** The optical image of the DC-ARF cross-section. Thanks to low refractive index coating (not visible on the image due to fibre cleaving) light can be guided in the core by glass anti-resonance and in glass cladding based on total internal reflection (TIR); **(B)** Image of the light confined in hollow-core and cladding of the DC-ARF; **(C)** Attenuation spectrum of the DC-ARF obtained in cut-back test, highlighting fundamental window with loss <0.2dB/m over 500 nm wide band, high loss region and second transmission window; **(D)** Bend loss of DC-ARF for different bend radii and wavelengths.

3.2.1 Attenuation Measurement

The DC-ARF attenuation was measured in the cut-back technique for 10 m and 40 m fibres. The study was conducted with a white light source (WLS) that was coupled to the DC-ARF through a launch fibre (SMF-28) to achieve a fundamental mode core light coupling. An optical spectrum analyser (OSA; Ando AQ – 6315A) recorded transmission spectra within a spectral range of 400 – 1750 nm for both fibre pieces, and the attenuation is plotted against spectral range in **Figure 3.1C**. The widest, anti-resonant fundamental window is a range of around 750 nm to beyond 1750 nm, and the second transmission window covers part of the visible light spectrum between ~ 425 nm to 600 nm. A low loss of < 0.2 dBm^{-1} (~3.3% per meter) is maintained over the 500 nm window between 800 nm – 1300 nm to satisfy the requirements for NIR excitation wavelength for multiphoton microscopy [22]. The high loss region (**Fig. 3.1C**) represents wavelengths that are in resonance with the thin glass layer of the tubes, cannot remain confined in the hollow area and leak away through the glass of the membranes. Depending on the application, the transmission broadband of the ARF can be controlled and adopted by the thickness of its capillaries [18]. Using longer segment of DC-ARF will increase the transmission loss significantly (for 3m, attenuation is 9.9%) , however, recently the ORC Southampton University fabricated NANF with h a loss of 1.45 ± 0.15 dB km^{-1} (0.024% per meter) at 850 nm and transmission spectrum 600 – 1100 nm [45].

3.2.2 Bend Loss Measurement

An endoscope typically requires a fibre that is several meters long to allow remote applications and operational flexibility [23]. This introduces bends that will induce additional attenuation to the signal transmission causing loss in DC-ARF [31]. In order to investigate this problem, transmission spectra from a 3 m fibre of different bend radii were studied and are shown in **Figure 3.1D** for five different wavelengths across the NIR . As a reference point, multiple measurements of the signal transmission were taken for the Ø40 cm bend radius fibre expecting no loss of power/transmission. Results (**Fig. 3.1D**) show an abrupt increase in transmission loss for bend radii below 10 cm of shorter wavelengths while for longer wavelengths bend loss is unnoticeable until going down to 5 cm radii. Presented results have a similar bend loss pattern to the ones reported in the literature [83-85] and account for phase matching induced by interaction of core mode and hollow capillaries modes.

3.3 Suitability of Fibre Characteristics For Multiphoton Endoscopy

Evaluation of the waveguide for nonlinear, multiphoton endoscopy can be conducted based on three primary criteria: transmission range, spectral broadening of the pulse caused by optical nonlinearities, and dispersion that increase the pulse time. Following these examinations, the effectiveness of delivering distortion-free laser pulses to the sample can be determined. Furthermore, the fibre should have the ability for backward collection of the nonlinear signal with the maximum achievable coupling efficiency within the visible spectral range, and then guide it to the detector. Here, based on those characteristics, the DC-ARF is compared with the "regular" ARF of very close dimensions to DC-ARF, and solid-core fibre (SCF). Additionally, polarization-maintaining properties and M^2 value (formula 25) were also investigated.

The main characteristics of DC-ARF have been described earlier in this chapter. The "regular" ARF was coated with a high refractive index polymer jacket so its transmission capacity is only in the hollow-core. Hence in this project, for clarity, this fibre is named as single-clad ARF (SC-ARF). The following are the main geometrical features of SC-ARF: seven tubes, core ≈ 25 µm, cladding outer diameter (OD) ≈ 130 µm, coated OD ≈ 275 µm. Its loss at 800 nm is around 0.6 dB/m.

The second selected waveguide for comparing with the DC-ARF was a commercial single-mode fibre SMF-28-J9 from Thorlabs with a core diameter of 8.4 µm and a cladding diameter of 125 µm. Its transmission band ranged between 1260 - 1625 nm, and cut-off wavelength was at 1260 nm. Comparison of the dimension of the main parts for three fibres is shown in ***Table 2***.

Fibre	Core diameter [µm]	Cladding diameter [µm]	Coating diameter [µm]
SCF	8.4	125	242
SC-ARF	25	130	275
DC-ARF	26.3	137	279

Table 2. Comparison of the geometry of the main components for three fibres: SCF, SC-ARF, and DC-ARF. HCFs have a very close dimension.

Tubular fibres are characterized by the strong single-mode light confinement after tens of meters of propagation [18]. In this work, experiments were performed on shorter fibre lengths (≤3 m), which allows for single-mode propagation, however, some small contribution from the LP11 mode can be expected. Therefore, there is a modal match between ARFs and SMF-28 due to its multimode character within the wavelength range (800 – 1000 nm) used in this project.

3.3.1 Optical Transmission

Spectral transmission range in all three fibres was measured with the same setup that was used for cut-back characterization (section 3.2.1). Thus, tested fibre was connected to a white light source via a launch fibre (SMF-28) to increase the fundamental mode light confinement in the core. The optical spectrum analyzer received the signal guided by the tested fibre and showed its transmission range. The graph in **Figure 3.2A** contains the optical transmission plots of the core for all three waveguides (green, blue, and red curves) and the cladding transmission plot for DC-ARF (black curve). There are very good transmission properties in the core between 800 – 1000 nm for all three fibres. Both ARFs can guide the signal in similar wavelength windows, and their high loss regions where light is in resonance with the silica glass overlapped between 600 -750 nm. Although, SC-ARF and SCF cannot transmit in the cladding area, still some wavelengths of multiphoton emitted signals can be accommodated in their core. Moreover, since SCF and DC-ARF cladding are made of the same material, their transmission spectra show similarity. The ability of DC-ARF cladding to guide the light in the broadband optical region is clearly demonstrated in this investigation.

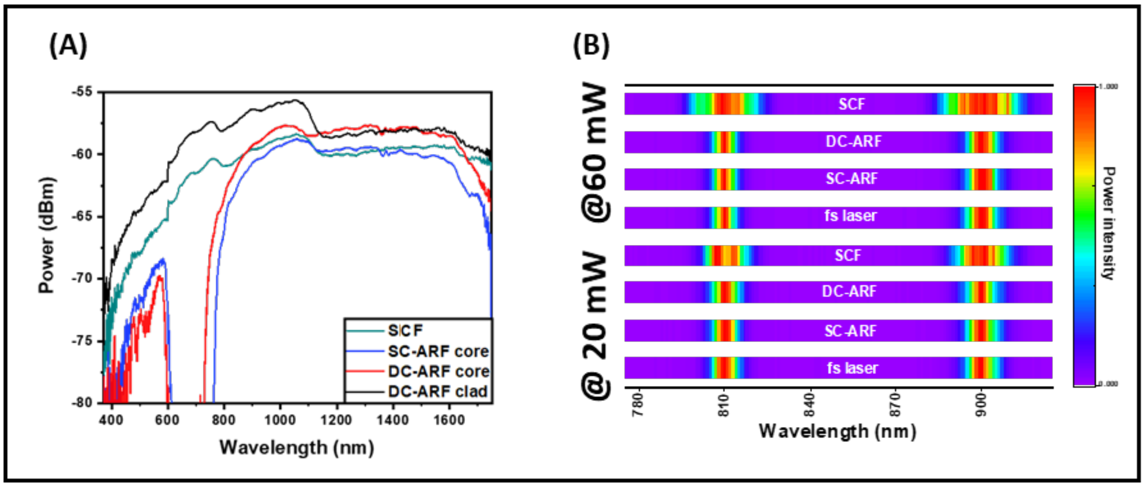

Figure 3.2 Comparison study of SCF, SC-ARF and DC-ARF; **(A)** Measured transmission spectra in the core and cladding for all three fibres that show their strong guiding properties between 800 - 1000 nm in the core required for excitation light, and DC-ARF transmission capacity in the cladding; **(B)** The effect of optical nonlinearity on pulse laser propagation in all three fibres taken at 810 nm and 900 nm for 20 mW (bottom four rows) and 60 mW (top four rows). Increased power has no effect on spectra in two HCFs, and it caused strong spectral broadening for SCF.

3.3.2 Nonlinear Spectral Effects

Nonlinear spectral effects caused the broadening of the spectrum that is proportional to the peak power [4]. The effect of nonlinearity in pulse laser propagated in three fibres was investigated for two wavelengths: 810 nm and 900 nm, and two average laser power inputs of 20 mW and 60 mW. Experimental parameters (wavelength and power) were selected based on SHG imaging requirements. Using an optical spectrometer (Ocean Optics Red Tide 650) and 116 fs Ti:Sa pulsed laser, spectra before and after propagation in all three fibres were obtained and analysed. **Figure 3.2B** shows spectra of the laser pulses at 810 nm and 900 nm, for two powers of 20 mW and 60 mW, measured after free-space delivery and after its delivery though 3 m long fibre (SCF, SC-ARF, and DC-ARF). The original bandwidth at full-width-half maximum (FWHM) of the fs pulse laser travelled in free-space is ~ 10nm. For the SC-ARF and DC-ARF, no spectral broadening is observed meaning that the nonlinearity related to optical power did not affect laser beam guided in HCFs. On the contrary, spectra of the SCF shows significant dependence on the increasing power level resulting in broadening and splitting of the optical spectrum even at 20 mW.

3.3.3 Dispersion

Dispersion of the laser pulse after propagation in all three fibres was studied by collecting intensity autocorrelation trace for 20 mW average power at 810 nm, 850 nm, 900 nm, and 950 nm. The measurement was conducted at the laser source and at the input and output of 3 m long fibre using pulse check (The Modular Autocorrelator, APE) and Ti:Sapphire laser (116 fs, 80 MHz, MaiTai, Spectra physics). Pulse duration τ (***Table 3***), group velocity dispersion (*GVD*) and its parameter *D* (***Table 4***) for all three fibres at different *λ* was determined from intensity autocorrelation measurements, using a method similar to that reported previously by other studies [32, 82].

	τ (fs)			
	810 nm	**850 nm**	**900 nm**	**950 nm**
SCF	2659	2638.2	2553.2	2035.4
SC-ARF	168	156.3	133.2	117.2
DC-ARF	180	144	128	119

Table 3. Pulse duration of 116 fs laser measured directly at the fibre output for SCF, SC-ARF, and DC- ARF. FWHM of the autocorrelation function was divided by deconvolution factor corresponding to the pulse shape. For Gaussian beam, it was 1.41.

	D (ps $*nm^{-1} * km^{-1}$)			
	810 nm	**850 nm**	**900 nm**	**950 nm**
SCF	- 103 (± 0.29)	- 90.7 (± 0.23)	-78.3 (± 0.31)	-56 (± 0.26)
SC-ARF	0.163 (± 0.56)	0.404 (± 0.45)	1.45 (± 0.48)	2.13 (± 0.39)
DC-ARF	-0.48 (± 0.29)	1.1 (± 0.44)	1.81 (± 0.41)	1.8 (± 0.35)

Table 4. Dispersion in fibres. Dispersion parameter (*D*) for group velocity dispersion (*GVD*) calculated for SCF, SC-ARF, and DC-ARF. ± - Standard Error of the Mean (SEM).

Results presented in ***Tables 3*** and ***4*** show a small increase in pulse duration and near to zero dispersion for both HCFs in the spectral range 800-1000 nm, while SCF pulse duration extended by one order of magnitude from 116 fs to 2659 fs at 810 nm causing significant contribution anomalous dispersion. Furthermore, based on fibre geometry and experimentally obtained loss in transmission, the computational simulations were conducted for SC-ARF and DC-ARF. Here, the predicted value of dispersion parameter D as a function of wavelength between 800 – 1000 nm for SC-ARF (**Fig. 3.3A**, black curve) and for DC-ARF (**Fig. 3.3B**, black curve) is presented versus measured and calculated results (red curves) for both waveguides. Simulation results are in agreement with experimental data and any discrepancies could have their origin in fibre imperfection due to the production process. At 810 nm, SC-ARF does not follow the predicted dispersion parameter *D* value.

This can be explained by operating close to the edge of the transmission window where higher-order modes can be excited with group delays and a higher value of chromatic dispersion different from that in the fundamental mode.

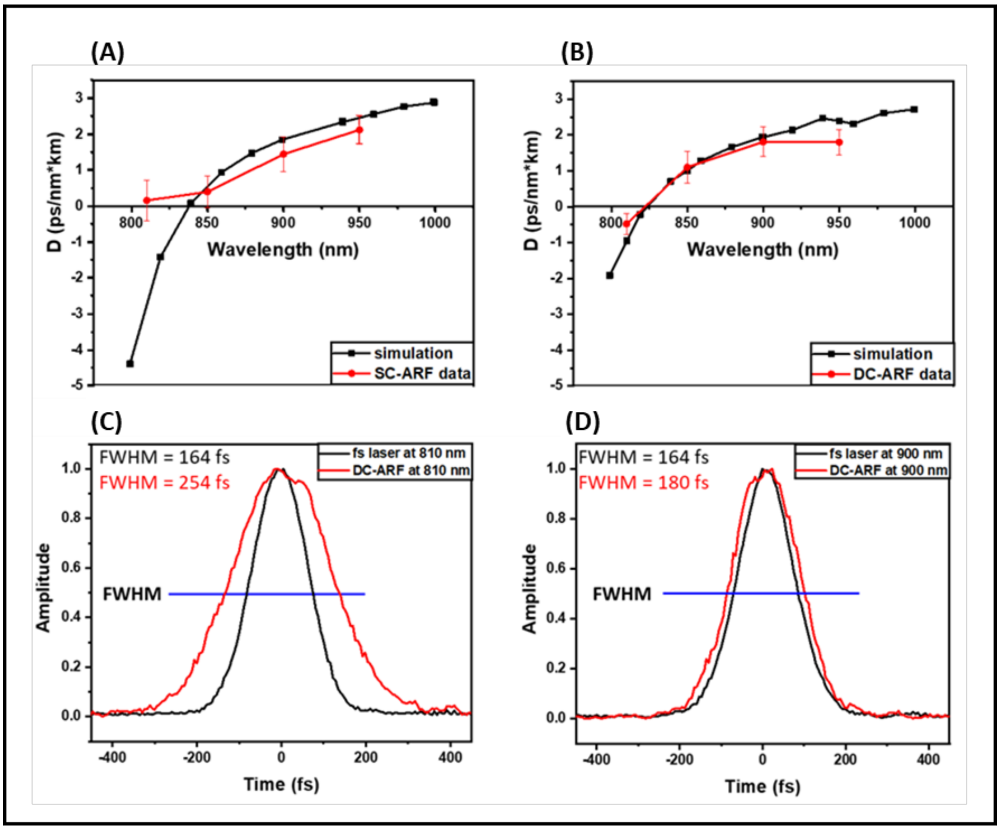

Figure 3.3 Dispersion in ARFs **(A, B)** comparison of *GVD* simulated data (black) with measured results (red) for SC-ARF and DC-ARF; **(C, D)** Intensity autocorrelation traces of the transform-limited fs laser pulses (116 fs Ti:Sa) measured at the input and output of the 3 m DC-ARF at 810 nm and 900 nm and 20 mW power.

Figure 3.3C, D presents the intensity autocorrelation trace of the fs transform-limited laser pulse at the input and output of DC-ARF at 810nm (**C**) and 900nm (**D**). For shorter λ (**Fig. 3.3C**), pulse broadening is greater and could be related to intermodal dispersion rather than spreading the pulse caused by optical nonlinearity, which was not detected for DC-ARF (**Fig. 2.2B**).

From these measurements it shows that the dispersion effect with hollow-core fibres (HCFs) is very small and should not change pulse characteristics. This is a desirable outcome since multiphoton microscopy (MPM) signals are inversely proportional to the pulse width [4].

3.3.4 Polarization

SHG is a polarization-sensitive technique and the agreement in orientation between the excitation state of polarization and SHG active structure will increase the intensity of the emitted signal [23]. Due to the circular symmetry of the fibre, vertical and horizontal polarization modes travel with the same phase velocity. However, the fibre core is slightly elliptical rather than circular, and its dopant concentration is never uniformly distributed. Fibre will exhibit a small amount of birefringence, which causes the refractive index of the material to be dependent on the polarization and direction of the propagated electric field. As a result, the cross-talking between vertical and horizontal polarization modes will change the net state of wave's polarization [30, 31].

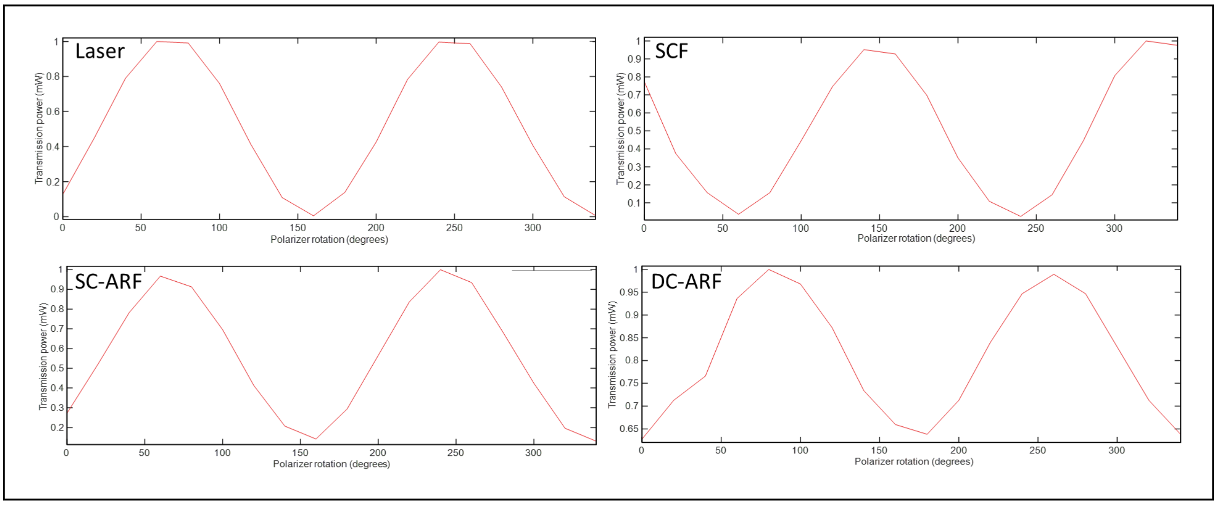

Figure 3.4 Dependence of transmission power behaviour on the different degree of polarization for pulse laser propagated in free-space, SCF, SC-ARF, and DC-ARF. The results demonstrate the polarization-maintaining properties of ARFs.

The state of polarization was measured in all three fibres and then it was compared with free-space laser propagation. Presented graphs in **Figure 3.4** show transmission power level as a function of polarization rotation degree for free-space fs laser, SCF, SC-ARF, and DC-ARF. From these results, it can be concluded that HCFs have no effect on the orientation of polarization, the direction remains similar to the initial state of polarization of the laser. However, the behaviour of the laser polarization changes during propagation in the SCF indicating a lack of polarization-maintaining property of the fibre. As a result, this will create a mismatch between the orientation of fibres collagen and the oscillating electric field leading to lower signal excitation on the sample and missing lots of important information about biological tissue.

3.3.5 M^2 Measurement

Beam quality factor or propagation factor (M^2), is a common technique used in the evaluation of the quality of a laser beam [86]. The M^2 of the ideal Gaussian beam is equal to 1, and the focus spot is diffraction limited. The M^2 value close to 1 indicates the proximity of the laser to single-mode TEM_{00} (fundamental transverse mode) propagation and implies high capability to focus a collimated laser to a tight spot. According to ISO Standard 11146 [87], M^2 for stigmatic beams is defined as:

$$M^2 = \frac{\pi}{\lambda}\frac{d_{\sigma 0}\theta_{\sigma}}{4} \tag{25}$$

where $d_{\sigma 0}$ is the beam radius at the beam waist,

θ_σ is the half-angle beam divergence.

Using a scanning-slit optical beam profiler (B2 290 – VIS, Thorlabs), the diameter of the beam at various positions around the focal point was taken for all the fibres, and the free-space propagating laser and plotted as a function of its position along the X and Y axes with the hyperbolic fit (**Fig. 3.5**).

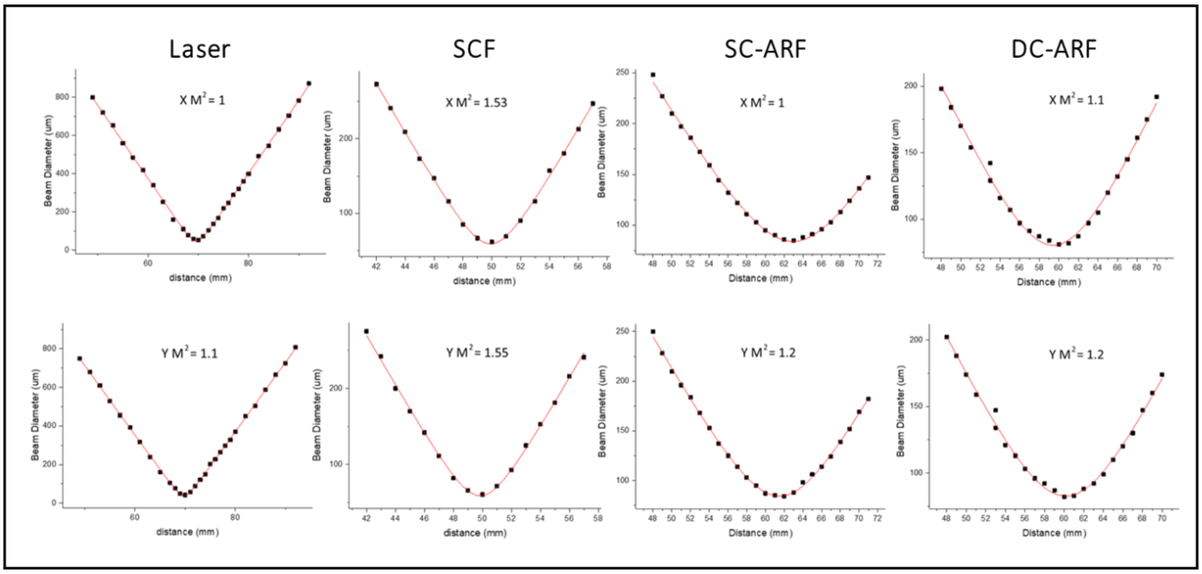

Figure 3.5 M^2 results for three studied fibres and the laser pump. Guiding light in the SC-ARF and DC-ARF maintained a high focusing capacity that is supported by M^2 results close to 1.

M^2 results demonstrate a small effect on laser beam focusing ability when propagating in HCFs. The M^2 value for SC-ARF and DC-ARF was measured as 1.1, an increase by 0.1 from the value of the free-space laser propagation. In the SCF, the M^2 value increased to 1.55. This increase in M^2 value for SCF may suggest the excitation of higher-order modes in this fibre and worsen the ability to focus the light.

3.3.6 Second Harmonic Generation Imaging

Using the Second Harmonic Generation (SHG) technique of MPM, all three fibres were tested under two experimental epi-detection imaging configurations presented in **Figure 3.6** and are named as non-descanned detection (NDD) and the de-scanned detection (DD) configurations. In NDD, fibre is used only for the delivery of the femtosecond laser, while in DD, fibre has a multifunctional performance, which is guiding the excitation light and collecting back-scattered signals. Both configurations can be used in multiphoton endoscopy, however, the ultimate endoscopic probe should be suitable miniaturization. The utilization of a single fibre for laser delivery and signal collection (DD), therefore, represents a better solution in which the bulky detection unit of the system is not a part of the probe and can be accommodated at the proximal end of the fibre.

However, for comparing the performance, SHG imaging measurements were carried out in both the NDD and DD configurations as shown schematically in **Figure 3.6**. 1m and 3 m long SCF, SC-ARF, and DC-ARF were used at 810 nm and 900 nm wavelengths in NDD and DD configurations. The SHG images of barium titanate crystals and mouse tail tendon from different areas of the same sample are presented in **Figures 3.7** and **3.8**. Furthermore, **Figure 3.9** shows control SHG images of barium titanate crystals and mouse tail tendon from different areas of the same sample obtained at 810 nm and 900 nm wavelengths when the laser was free-space delivered to the imaging system. All images were taken with an average power on the sample of 20 mW, and pixel dwell time 10.7 μs for 1 frame (NDD) and 27 μs for 10 frames (DD). The shift in the field of view of the images was caused by the protocol of the experiment that required the installation of each of the fibre separately in the setup. To keep consistency between imaging measurements with each of the fibre, power levels on the sample were measured and kept similar to the extent possible.

Non-Descanned Detection (NDD)

In NDD (**Fig. 3.6A**), fs laser pulse generated in tunable Ti:Sapphire oscillator (116 fs, 80 MHz range 710 – 990 nm, Spectra-Physics, Mai Tai) after passing a Faraday isolator was coupled into each of the fibres (SCF, SC-ARF and DC-ARF). The light was delivered to the home-built multiphoton microscope (a Leica DMRB upright microscope frame) that contained galvanometric scanning mirrors (Cambridge instruments) to perform laser beam scanning. The excitation laser beam was then directed to the microscope objective (Nikon 20x, 0.75 NA) through a dichroic mirror (Semrock, FF458-Di02; 458 nm long pass), and focused on the sample plane. In backward detection, nonlinear scattered light was collected by the same objective and orthogonally reflected by the same dichroic mirror to the photomultiplier tube (PMT) (Hamamatsu, H10722-01). Before entering the detector, the signal underwent additional filtering using a band pass filter at 405 ±5 nm (Thorlabs, FBH405-10) for 810 nm excitation and at 450 ± 5 nm (Thorlabs, FBH450-10) for 900 nm excitation. Image reconstruction was performed in ScanImage 2016b software operated by MatLab [88] and connected with the hardware by a DAQ card (PCI 6110, National Instruments), which gathered position data from the Galvo scanners and signal intensity from PMT.

PMT is most common single point detector used in laser scanning microscopy, however, it has poor detective quantum efficiency (~ 25%), which determines probability for every entering photon to generate an electron that is measured by the detector. If a detector has a quantum efficiency of 60%, for 100 photons that are striking its surface, average only 60 electrons will be generated, and 40 will be lost. The alternative to PMT is avalanche photodiodes (APDs), which is based on semiconductor material and “impact ionization“ process. Its quantum efficiency is ~90% in green region of the spectrum, but its drops ~30% in the blue region. On the other hand, it overheats if run too fast that gives advantage to PMT that can operate at the high speed without thermal effects.

Images in NDD configuration for 1 m long fibre (**Fig 3.7A** and **3.8A images (1, 3, 5, 7, 9, 11)**) are of higher quality compared to images for 3 m long fibre in NDD arrangement (**Fig 3.7B** and **3.8B images (1, 3, 5, 7, 9, 11)**) due to the shorter propagation distance of the laser inside the waveguide. The effect of the fibre length on the image quality is especially observable for SCF (**Fig 3.8A, B**, images **1** and **7**). Images taken with 1m of SCF illustrate a much higher signal level than that with 3 m long SCF. Furthermore, optical nonlinearity and dispersion caused pulse broadening of delivered excitation light in SCF so that the images show low signal excitation and emission with high noise. In the case of images taken with 1 m and 3 m of HCFs (**Fig 3.7** and **3.8,** images **3, 5, 9, 11** for NDD), they are of high quality with good visualization of structural features of the samples which is comparable with the imaging results from the free space coupled laser (**Fig. 3.9**).

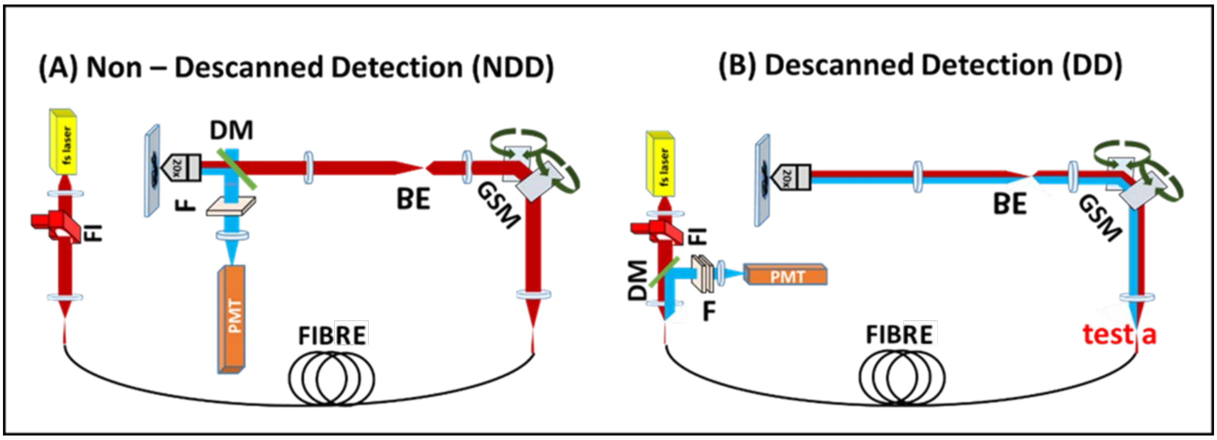

Figure 3.6 Schematic representation of SHG system working in non-descanned detection (NDD) (**A**) and descanned detection (DD) (**B**) signal collection configuration. The red thick line represents the excitation path and the blue thick line - signal collection path. FI – Faraday isolator, GSM – Galvanometric scanning mirrors, BE – Beam expander, DM – Dichroic mirror, F – Filter, PMT – Photon multiplier tube.

Descanned Detection (DD)

In the DD (**Fig. 3.6B**), the signal detection was at the proximal end of the fibre hence the system was rearranged so that the dichroic mirror, filters and the PMT were located now at the input of the fibre tip. At the distal end of the fibre, the signal was back-coupled into the core and cladding area of the fibre using the same lens which was applied in the excitation path. To evaluate the level of signal available for back-coupling, the SHG signal was measured before the galvanometric mirrors (**Fig. 3.6B)**, position “test a” located on the schematic representation of the DD setup) and it was ~10 times weaker from that detected in the NDD scheme. 1m and 3 m long SCF, SC-ARF and DC-ARF were tested for the capability to couple and deliver back enough of the SHG signal to reconstruct the image.

Although all three fibres could guide the light in the core between 400 – 500 nm (**Fig 3.2A**), the core's small surface area and low NA were insufficient to collect the minimum detected signal level needed for the image construction for SCF and SC-ARF (**Fig. 3.7** and **3.8** images **2, 4, 8, 10**). In those images, no sample features were present with high background noise. However, the DC-ARF with the ability to transmit the light in the core and cladding area could collect enough of the scattered signal for detection and visualization (**Fig. 3.7** and **3.8,** images **6** and **12**). Images of barium titanate crystals and mouse tail tendon produced in descanned detection prove the potency of a two-way waveguide DC-ARF in an endoscopy-like scheme (**Fig. 3.7** and **3.8,** images **6** and **12**).

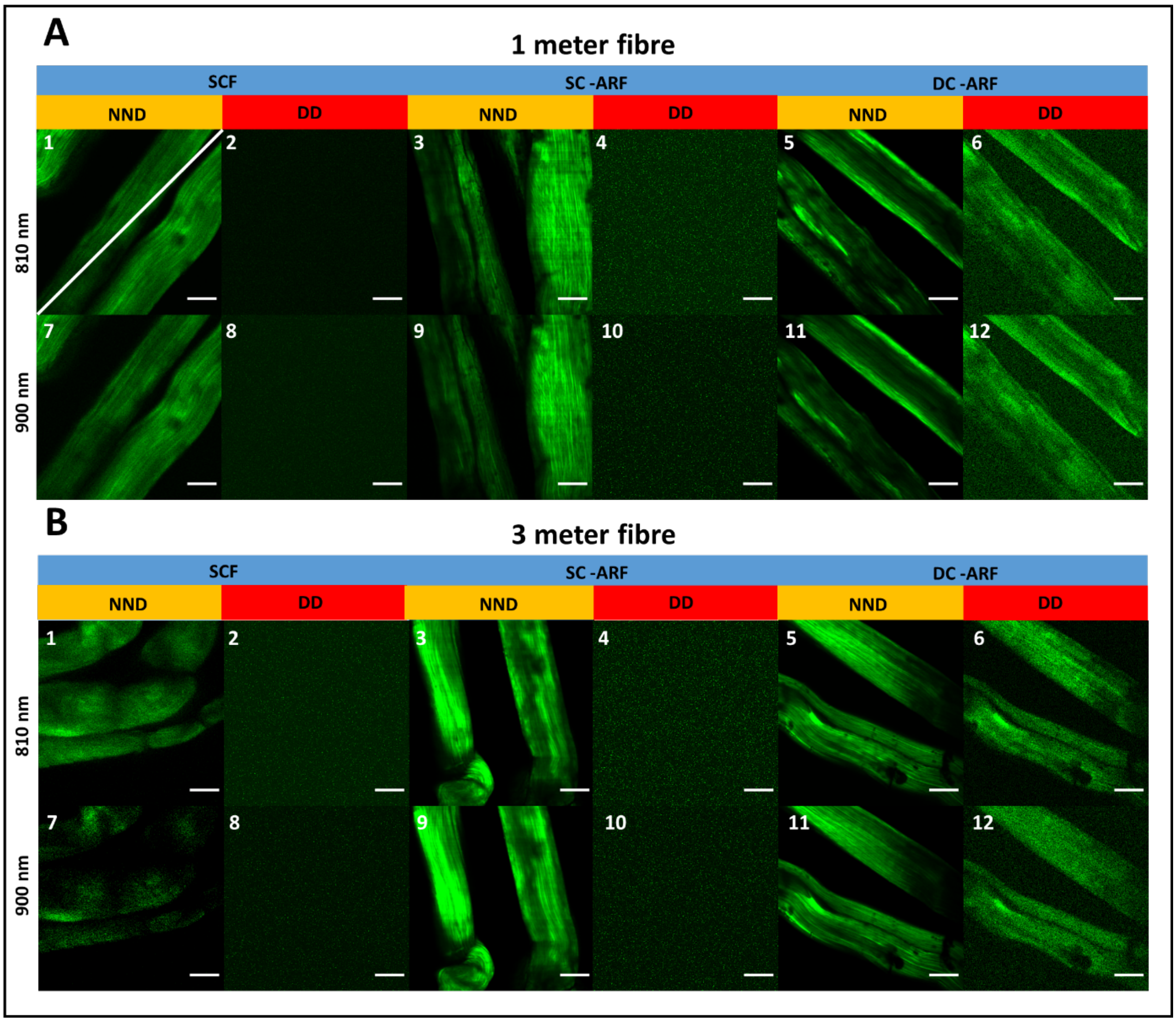
A
1 meter fibre
SCF
SC -ARF
DC -ARF
NND
DD
NND
DD
NND
DD
810 nm
900 nm
1
2
3
4
5
6
7
8
9
10
11
12
B
3 meter fibre
SCF
SC -ARF
DC -ARF
NND
DD
NND
DD
NND
DD
810 nm
900 nm
1
2
3
4
5
6
7
8
9
10
11
12

Figure 3.7 SHG images of mouse tail tendon taken in non-descanned detection (NDD) and descanned detection (DD) configuration using 1 m (**A**) and 3 m (**B**) SCF, SC-ARF and DC-ARF at 810 nm and 900 nm excitation wavelength are shown. The images were obtained from different areas of the same samples; (NDD: 20x objective, zoom 3, 341 pixels, 10,7 µs dwell time, ~20 mW power; DD: 20x objective, zoom 3, 341 pixels, 27 µs dwell time, ~20 mW power, average 10 frames). Scale bar = 50 µm.

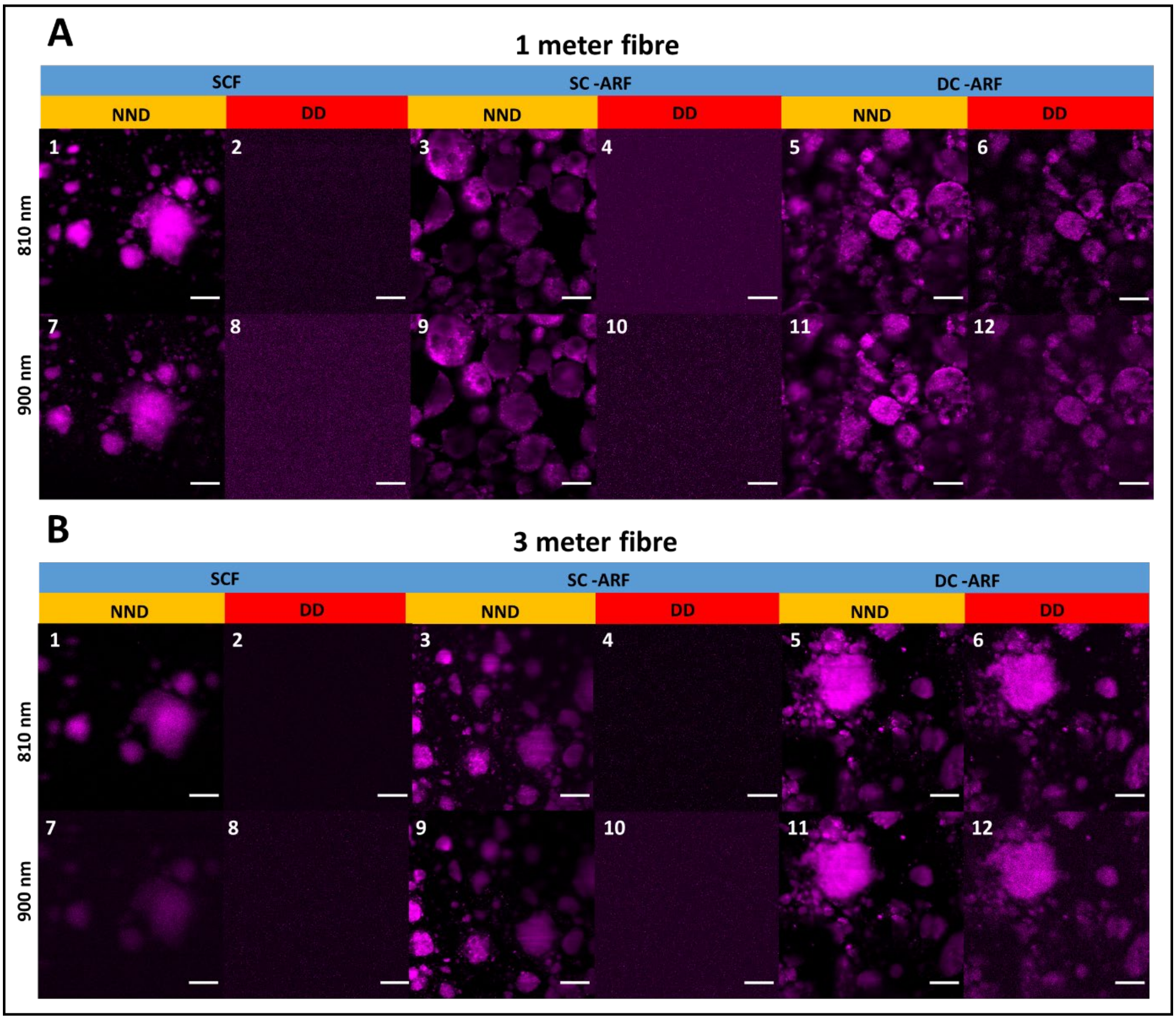
A
1 meter fibre
SCF
SC -ARF
DC -ARF
NND
DD
NND
DD
NND
DD
810 nm
900 nm
1
2
3
4
5
6
7
8
9
10
11
12
B
3 meter fibre
SCF
SC -ARF
DC -ARF
NND
DD
NND
DD
NND
DD
810 nm
900 nm
1
2
3
4
5
6
7
8
9
10
11
12

Figure 3.8 SHG images of barium titanate crystals taken in non-descanned detection (NDD) and descanned detection (DD) configuration using 1 m (**A**) and 3 m (**B**) SCF, SC-ARF and DC-ARF at 810 nm and 900 nm excitation wavelength are shown. The images were obtained from different areas of the same samples; (NDD: 20x objective, zoom 3, 341 pixels, 10,7 µs dwell time, ~20 mW power; DD: 20x objective, zoom 3, 341 pixels, 27 µs dwell time, ~20 mW power, average 10 frames). Scale bar = 50 µm.

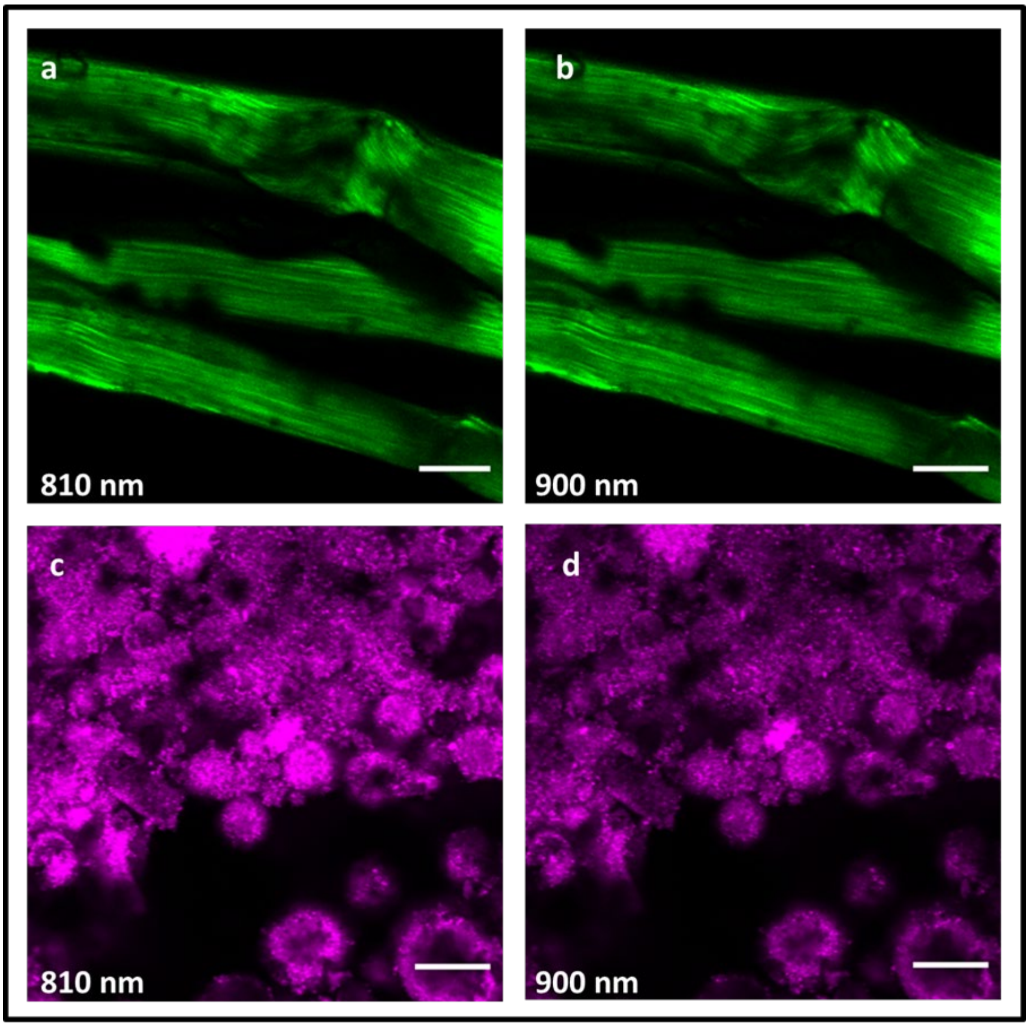

Figure 3.9 SHG images of mouse tail tendon (**a, b**) and barium titanate crystals (**c, d**) taken using a free-space propagated laser at 810 nm and 900 nm excitation wavelengths. The images were obtained from different areas of the same samples; (20x objective, zoom 3, 341x341 pixels, 10.7 µs dwell time, ~ 20 mW power). Scale bar = 50 µm.

Signal-to-Noise Ratio (SNR)

The overall image quality can be determined by the signal-to-noise ratio (SNR). The source of the noise in microscopy can originate from the background, optical components or sample itself [23]. For quantitative analysis using Fiji software [89], the average grey value was taken from a blank area of the image; this gave the mean value for noise. SNR was calculated by dividing the grey value taken along a line–profile drawn across the image (**Fig. 3.7A1**) by the mean value of the noise**.** **Figures 3.10** and **3.11** present graphs of SNR vs distance along the line-profile for all SHG images of mouse tail tendon and barium titanate crystals presented in **Figures 3.7** and **3.8** (images 1, 3, 5, 7, 9, 11) in NDD configuration and free-space imaging (**Fig.3.9**). Four curve colours represent different laser delivery methods so that black is for free-space, green is for SCF, blue is for SC-ARF, and red is for DC-ARF.

The results demonstrate the increase in SNR for 3 m fibre compared to 1 m fibre (**Graphs A, B, Fig. 3.10** and **3.11**) in NDD. Moreover, for 3 m ARFs the SNR level is comparable to images taken with the free-space propagating laser. However, the effect of laser pulse broadening caused by dispersion and nonlinearity in SCF is displayed in the very low SNR of the images taken with this fibre. Furthermore, an almost 7 times drop in signal is observed between 1m and 3m long SCF and shown in **Figure 3.12**, which presents the grey value plots for SHG barium titanate crystals images (**Fig. 3.8 A, B** images 1). Three plots of SNR for barium titanate (**Fig. 3.11A, B, C**) show unexpected high level of SNR for SCF. This may be explained by more distinct signal and blank area in images taken with SCF compared to images obtained using two ARFs (**Fig. 3.8**). Furthermore, it was expected that transmission in HCFs would generate less noise due to free-space like condition inside the core.

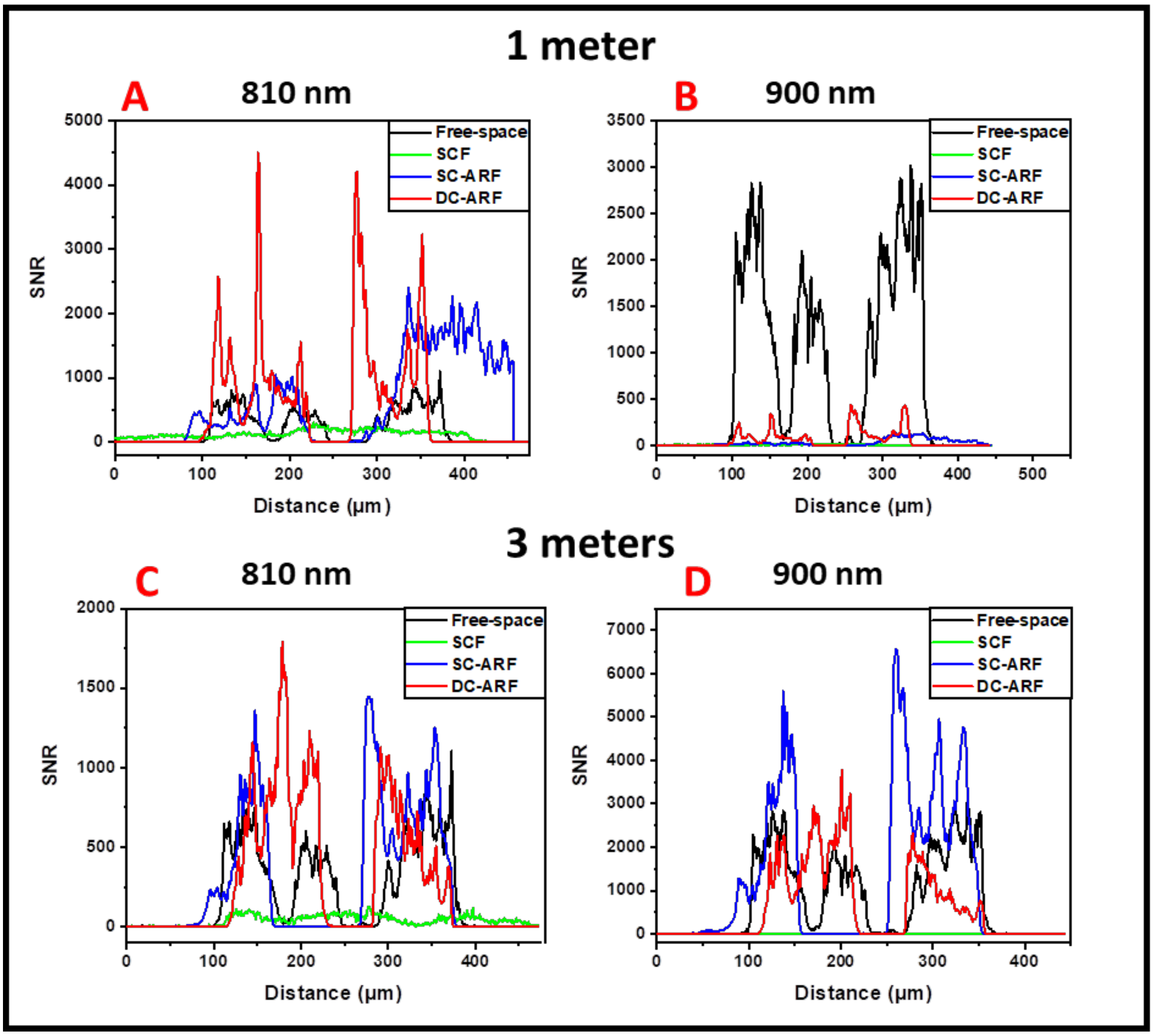

Figure 3.10 The analysis of the SNR for mouse tail tendon images taken in non-descanned detection (NDD) configuration. Images obtained in NDD for 1 m (**A, B**) and 3 m (**C, D**) long SCF, SC-ARF, DC-ARF presented in **Fig. 3.7** underwent SNR examination and the average SNR for the signal profile (**Fig. 3.7A1)** vs distance was plotted. The noise level was reduced for light propagated in 3 m fibre and is comparable with free-space laser propagation (black and red profile on the graphs).

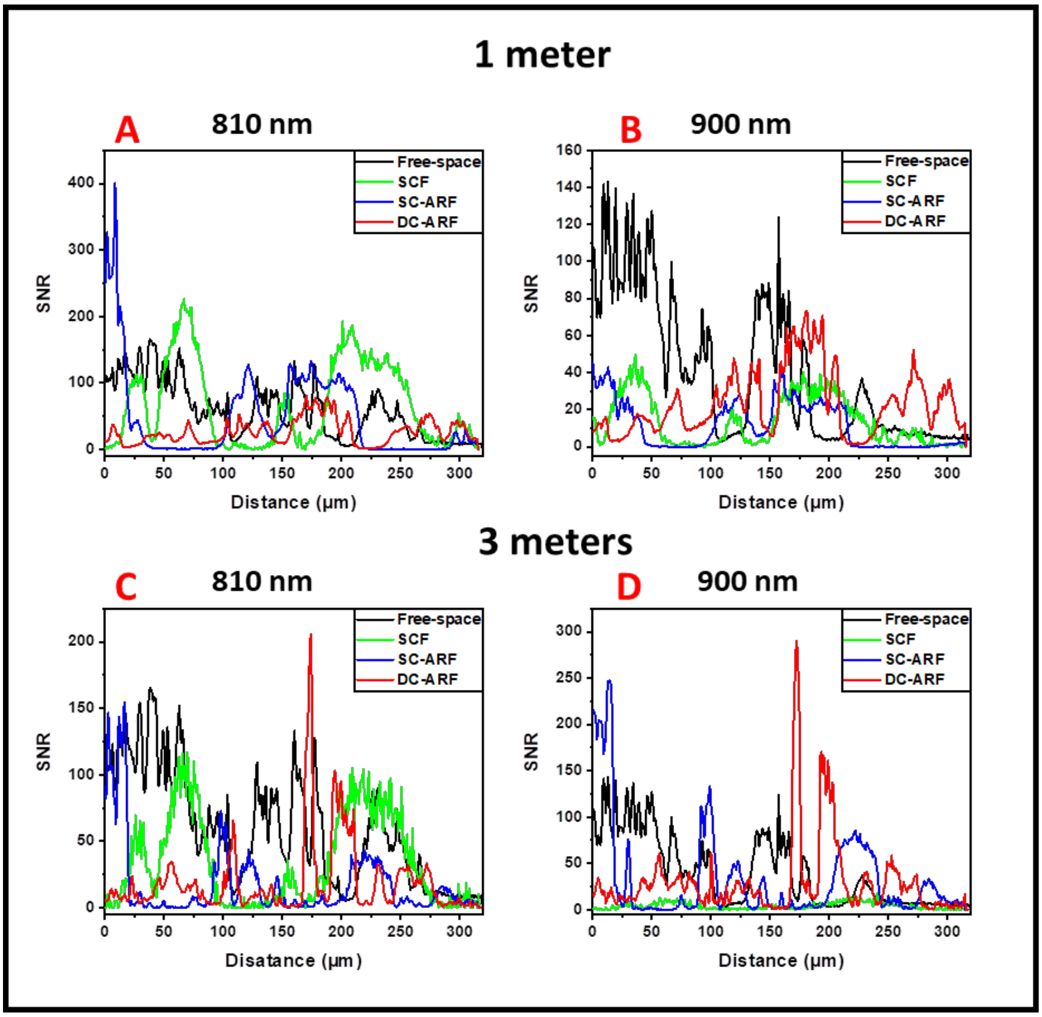

Figure 3.11 The analysis of the SNR for barium titanate crystals images taken in non-descanned detection (NDD) configuration. Images obtained in NDD for 1 m (**A, B**) and 3 m (**C, D**) long SCF, SC-ARF, and DC-ARF presented in **Fig. 3.8** underwent SNR evaluation and the average SNR (**Fig. 3.7A1)** vs distance along the line-profile is plotted. The noise level was reduced for light propagated in 3 m fibre and is comparable with free-space laser propagation (black and red profile on the graphs).

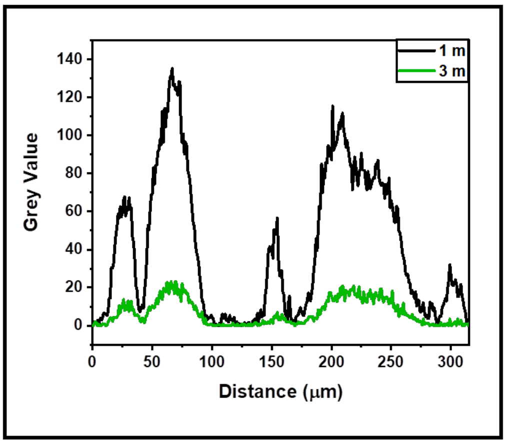

Figure 3.12 Measured grey values as a function of distance on the image for SHG barium titanate crystals images (**Fig. 3.8 A, B** images 1). The decrease in signal intensity between 1 and 3 m long solid core fibre (SCF) is mainly caused by anomalous group velocity dispersion (GVD) and nonlinearity.

Figure 3.13 presents the SNR graphs (A, B, C, D) for SHG images of mouse tail tendon and of barium titanate crystals (**Fig. 3.7 and 3.8 A, B** images 6 and 12) taken with 1m and 3 m DC-ARF in DD configuration, and example images are placed in the middle panel of **Figure 3.13**. Its level is sufficient enough to see the structural details of the barium titanate crystals and mouse tail tendon sample. The SNR measurement was done along line-profile (shown as white, solid line) in **Fig. 3.13**, (images in the middle panel). The noise suppression for 3 m DC-ARF is observable (red line **Fig. 3.13C, D**).

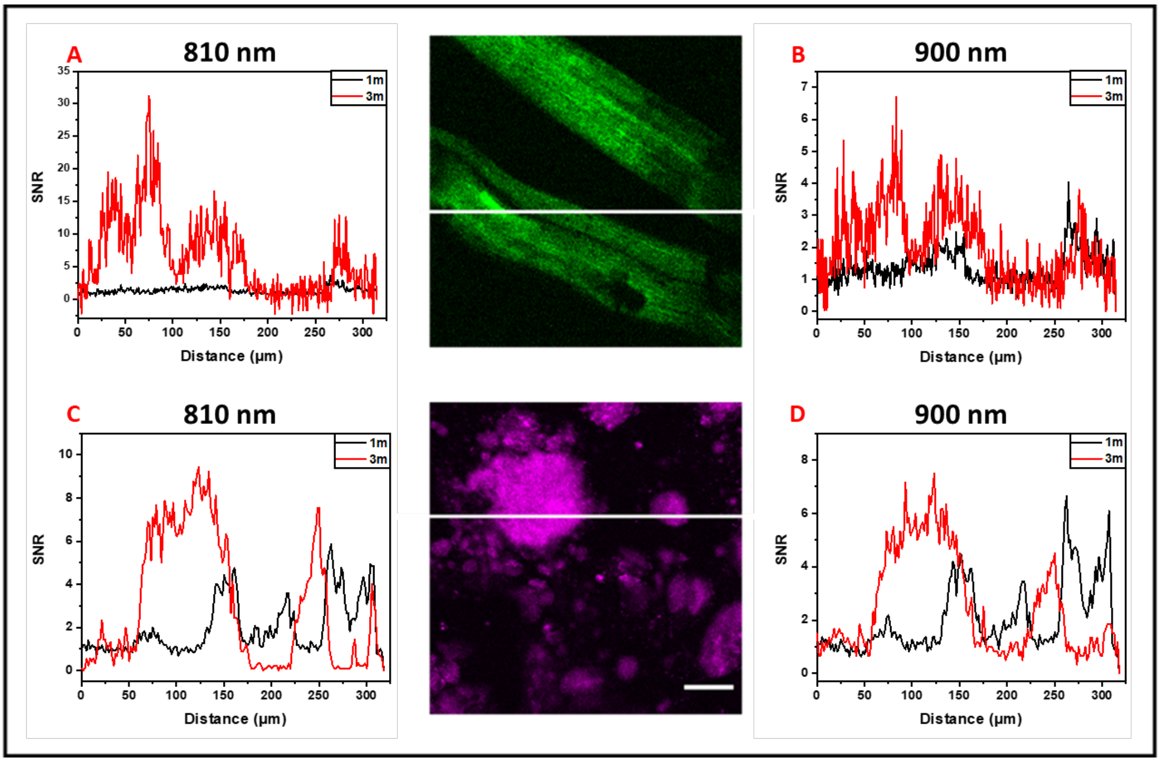

Figure 3.13 SNR analysis performed for mouse tail tendon and barium titanate crystals samples captured with descanned detection for 1m and 3 m long DC-ARF. The graphs of SNR vs distance are for mouse tail (**A, B**) and barium titanate crystals (**C, D**) measured along the line-profile (white line on the images in the middle) for images 6 and 12, **Figures 3.7** and **3.8 A, B** images. There is noticeable noise suppression for 3 m DC-ARF leading to similar SNR for two fibres lengths (red line profile).

3.4 Conclusions

This chapter investigated a new type of tubular, hollow-core fibre DC-ARF for a multiphoton, label-free endoscopy system. Its customised design allows for signal guidance in dual direction operation due to the adaptation of cladding areas for signal transmission. The capacity of the DC-ARF for delivering distortion-free high power, ultra-short laser pulse were compared with two different waveguides (SC-ARF and SCF). The main investigation was concerned with the effect of dispersion and nonlinearity on laser beam propagation in the fibre. Finally, all three fibres were incorporated into an SHG imaging system (laser scanning microscope) by coupling the laser into their core before entering the microscope. Mouse tail tendon and barium titanate crystals samples were imaged using SHG technique in non-descanned (NDD) and descanned (DD) configuration. Although, all three fibres had the ability to guide the signal in the core within the emission range of the samples, only DC-ARF transmitted enough SHG signal to reconstruct the image due to the guiding property of its cladding.

The analysis of SNR for the images suggested that the implementation of longer fibre leads to noise suppression. Current results demonstrated that DC-ARF is a strong candidate for label-free, multiphoton endoscopy. The next chapters would present work on miniaturized imaging devices in which remote operation and flexibility will be achieved by the incorporation of DC-ARF into the system.

Chapter 4 Hand-Held Microscope with Double-Clad Anti-Resonant Hollow-Core Fibre

4.1 Introduction

Advances in the development of miniaturized fibre-optic imaging devices has allowed for new biomedical studies and clinical treatments. The instrumentation range stretches from portable microscopes to ridged and flexible endoscopes [55, 57, 61]. The fundamental motivation for their development is to miniaturise the imaging device. Regardless of the construction approach, it is usually a trade-off between small and compact dimensions and its imaging performance that needs to be taken into account. The physical dimensions of the imaging device depend on the clinical application, hence, for example, portable and lightweight devices are needed for the examination of the human skin [54], while a small diameter probe (mm) that interfaces with a biopsy probe is needed for optical biopsy of internal organs or to enter hollow organs, and to be compatible with existing biopsy protocols [59]. Functional imaging visualization of brain activities and their structural dynamics in freely moving animals has been done with a miniaturized microscope mounted on their head [52] and therefore had to be appropriately small (cm) and lightweight.

Portability and miniaturization are the main requirements in terms of the operational mode and dimensions of imaging devices. The optical fibre serves as a waveguide to deliver illuminating light such as a laser to the sample to allow remote function and portable operation of the microscope. The suitability of double-clad anti-resonant hollow-core fibre (DC-ARF) for application in nonlinear endoscopy was studied in Chapter 3. It demonstrated the ability of the DC-ARF to deliver femtosecond laser beam free of distortions originating from nonlinear effects and dispersion in the fibre. Furthermore, this fibre can transmit the light in the cladding area, which can be used for the collection of signals and eliminate the utilization of additional fibres.

This chapter will describe the construction of a miniaturized laser-scanning microscope for non-linear imaging coupled to DC-ARF for remote illumination and detection. The non-linear imaging techniques of second harmonic generation (SHG) and two-photon fluorescence (TPF) were demonstrated with the microscope. The imaging device contains the scanner, and optical components (lenses, beam expander, and microscope objective), similar to a conventional laser scanning microscope [23]. Its “L” shaped construction and compact size allow for hand-held operation and hence, it is named as ‘hand-held microscope’ or HHM.

In this work, the performance of the assembled imaging device was characterized based on the power delivery to the sample and signal collection level in three different configurations such as free-space non-descanned detection (fNDD), free-space descanned detection (fDD), and descanned detection (DD) via DC-ARF. All three scanning configurations were tested with SHG imaging using samples of mouse tail tendon and barium titanate crystals. Both SHG and TPF imaging was performed using the HHM on biological samples. Finally, the impact of miniaturization on device performance was evaluated and compared with a stationary conventional laser-scanning microscope setup.

The aim of the work in this chapter was to help the transition towards building a micro-endoscopic system for label-free nonlinear imaging using hollow-core fibre technology.

4.1.1 Aim and Objectives

Aim: To establish a hand-held microscope (HHM) configuration with DC-ARF for non-linear microscopy.

Objectives:

1. Test and optimise different laser delivery and signal collection configurations.

2. Test the performance of the HHM with the non-linear microscopy technique of second harmonic generation (SHG) on standard and biological samples.

In this chapter, different detection arrangements are studied in order to investigate the loss of detected signal especially due to the placement of the signal sensor. In particular, 3 configurations were tested with the HHM: (1) laser excitation through fibre and signal collection directly with a non-descanned detector, that is, the free-space non-descanned detection configuration (fNDD); (2) laser excitation through fibre and signal collection directly with a descanned detector, that is, the free-space descanned detection configuration (fDD) and (3) laser excitation as well as signal collection through fibre, that is, the descanned configuration with DC-ARF (DD). In addition, the quantitative evaluation of images obtained in these scanning configurations will be demonstrated.

4.2 The Experimental Setup

The design of the HHM is shown in **Figure 4.1**, and it presents a schematic depiction of the experimental setup **(A)**, together with the assembled HHM illustrated in Fusion 360, Autodesk software and photographed **(B, C)**. Different configurations of the signal collection showed in **Figure 4.1A** will introduce additional optical parts to the HHM system and will be discussed later in more detail. Red letters D and P in **Figure 4.1A**, stand for distal and proximal end of the fibre, respectively.

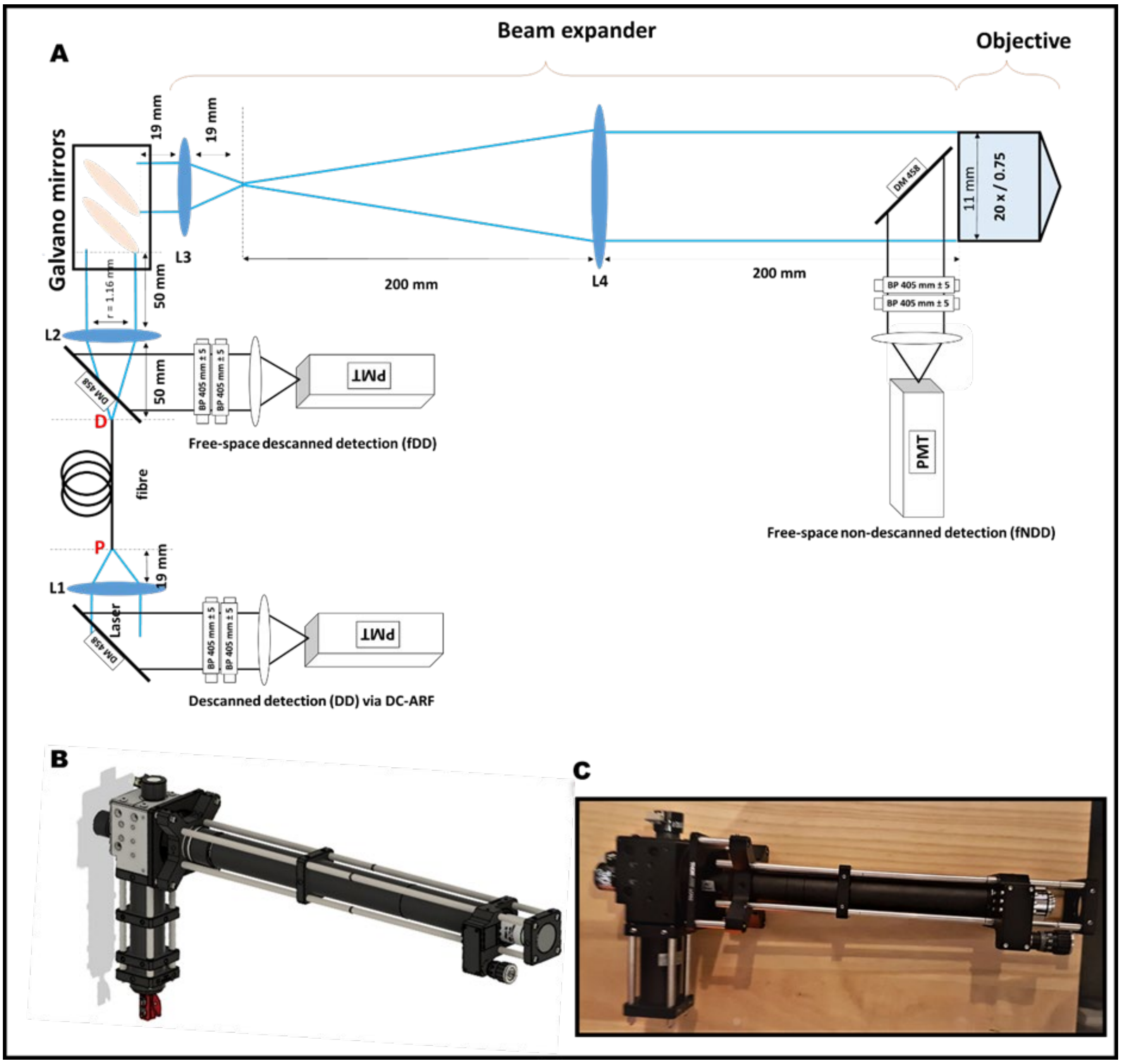
A
Beam expander
Objective
Galvano mirrors
19 mm
19 mm
L3
r = 1.16 mm
50 mm
200 mm
L4
200 mm
DM 458
11 mm
20 x / 0.75
BP 405 mm ± 5
BP 405 mm ± 5
L2
DM 458
50 mm
BP 405 mm ± 5
BP 405 mm ± 5
PMT
D
Free-space descanned detection (fDD)
fibre
PMT
Free-space non-descanned detection (fNDD)
P
19 mm
L1
Laser
DM 458
BP 405 mm ± 5
BP 405 mm ± 5
PMT
Descanned detection (DD) via DC-ARF
B
C

Figure 4.1 HHM; **(A)** Schematic representation of the experimental design shows the main parts of the HHM: fibre, Galvano mirrors, beam expander, and optical objective; the HHM was tested with different detection configuration, that are presented on a diagram (fNDD, fDD, DD); **(B)** Assembled presentation of the HHM executed in Fusion 360, Autodesk software; **(C)** Photo of the HHM.

A femtosecond laser (λ=810 nm) is delivered to the HHM using 1 m of DC-ARF, collimated with lens L2 (ThorLabs, AC254-050-AB Achromatic Doublet) and scanned by two galvo mirrors (ThorLabs, GVS002 - 2D Galvo System, Silver-Coated Mirrors) to raster scan the beam on the sample. Then, a beam expander (BE) made of two lenses (ThorLabs, Achromatic Doublets: L3 = AC127-019-AB, L4 = AC254-200-AB) magnifies the incoming laser beam diameter x10 to match the back aperture of the objective lens (Nikon, 20x Mag, 0.75 NA) that is used to focus the laser on the sample. The collected signal travels back through the BE, scanner to the fibre, where is coupled to the DC-ARF. Although **Figure 4.1A** shows the detector placed in three different locations, the ultimate detection configuration of the HHM was with descanned detection (DD) via DC-ARF. In DD, the signal detection unit is located at the proximal end of the fibre and contains a band pass filter at 405 ±5 nm (Thorlabs, FBH405-10) for 810 nm excitation, and a photomultiplier tube (PMT) (Hamamatsu, H10722-01). Synchronization of the image acquisition and position data obtained by Galvano mirrors movements is controlled by a DAQ card (PCI 6110, National Instruments) and ScanImage 2016b software operated by MatLab [88]. The glass cap mounted at the distal end of the HHM serves to protect the objective from direct contact with the sample and sets its working distance.

The HHM is made of two arms mounted orthogonally with the Galvano mirrors. The longer segment of the HHM is approx. 40 cm in length resulting in an undesirable increase in the dimension of the whole device. This long HHM segment contains lenses that construct the beam expander to expand the beam to match the size of the back aperture of the objective to allow the full numerical aperture of the lens to be used and thus obtain a diffraction-limited spot. The laser beam diameter increased almost 10 times from 1.16 mm to 11mm (**Fig. 4.1A**). Implementation of a smaller objective would reduce the need for 10x beam magnification and the 40 cm BE length. Thus the whole device could easily be reduced in its dimensions.

4.2.1 Detection Configurations

The HHM system was tested in three detection configurations (**Figure 4.1A**): free-space non-descanned detection (fNDD), free-space descanned detection (fDD), and descanned detection (DD) via DC-ARF.

In free-space non-descanned detection (fNDD), the dichroic mirror (Semrock, FF458-Di02; 458 nm long pass) is placed before the objective in the path of the incoming laser beam and orthogonally reflects the collected signal below 458 nm to the PMT via two band pass filters and focusing lens (L5).

In free-space descanned detection (fDD), the dichroic mirror (Semrock, FF458-Di02; 458 nm long pass), two band pass filters, a focused lens (L5) and a PMT sensor, are placed right before the distal (marked by letter **D** on **Fig. 4.1A**) end of the DC-ARF.

In descanned detection (DD) via DC-ARF, the dichroic mirror (Semrock, FF458-Di02; 458 nm long pass), two band pass filters, a focused lens (L5) and a PMT sensor, are placed right before the distal (marked by letter **P** on **Fig. 4.1A**) end of the DC-ARF.

4.3 Performance of the Multiphoton Hand-Held Microscope

For any imaging system working with biological samples, a fundamental issue is to have sufficient laser power on the sample enough for a signal to be generated for detection yet ensure that it is below the damage threshold, to prevent its irreversible destruction [90]. When working with biological samples, a medical or clinical examination should not cause irreparable harm to the studied subject.

When using a standard imaging system with multiphoton microscopy, typically 10-30 mW of laser power is easily available and sufficient. Furthermore, such systems operate based on non-descanned type of detection that allows signals to be collected with less losses due to the proximity of the detector to the sample signal source [19].

The construction of portable imaging devices based on optical fibres encounters many challenges in power delivery. First, the employment of fibre-optic in the system results in laser power loss as the transmission efficiency does not reach its maximum 100% due to fibre attenuation, bend losses, scattering at the point of fibre entry or coupling conditions [34].

In this work losses due to the fibre as well as due to other optical components in the imaging system were encountered. The DC-ARF used in this work, has the capacity to confine the light to the core and the cladding, whose surface area is larger than the hollow area of the core. This imposes certain inconvenience in terms of coupling procedures into the core because light will enter the larger cladding surface area. Losses in laser power is also expected when propagated through the imaging device upon encountering optical components [32]. Such an evaluation was performed for the HHM, and a large drop in the laser power (up to 50%) was measured for the light passing the beam expander (BE). This has a significant effect on the sample excitation and hence, signal generation. Ultimately, the HHM must operate in descanned detection (DD) mode, which means due to the placement of the PMT on the proximal (the opposite end to the sample) there will be 50% loss of signal that will be induced by the beam expander (BE) optics.

4.3.1 Free-Space Non-Descanned Detection

Free space, non-descanned detection (fNDD) configuration provides the least distance between the generation of the signal and the detector (**Fig. 4.1A**). Even though collection optics are in the signal path there are always losses when propagating through a medium (air, glass). The non-descanned detection configuration minimises these losses and thus ensures the highest back scattered signal detection. **Figure 4.2** presents the fNDD arrangement applied in the HHM system. The term "free-space" indicates that scattered light travels back in free space (air). The dichroic mirror (Semrock, FF458-Di02; 458 nm long pass) is placed before the objective in the path of the incoming laser beam and orthogonally reflects the collected signal below 458 nm to the PMT via two band pass filters and focusing lens (L5). The HHM was evaluated using the second harmonic generation (SHG) technique in the imaging process of mouse tail tendon and barium titanate crystals samples at 810 nm wavelength (**Fig. 4.3**). The average power on the sample was ~20 mW. The obtained images are of good quality with high signal level (**Fig. 4.10 graph 2**). Since the free-space detection minimizes the loss of signal the images taken here with the HHM represent the maximum possible signal-to-noise ratio for this setup. Hence, they provide a benchmark for the other configurations that were tested with the HHM setup.

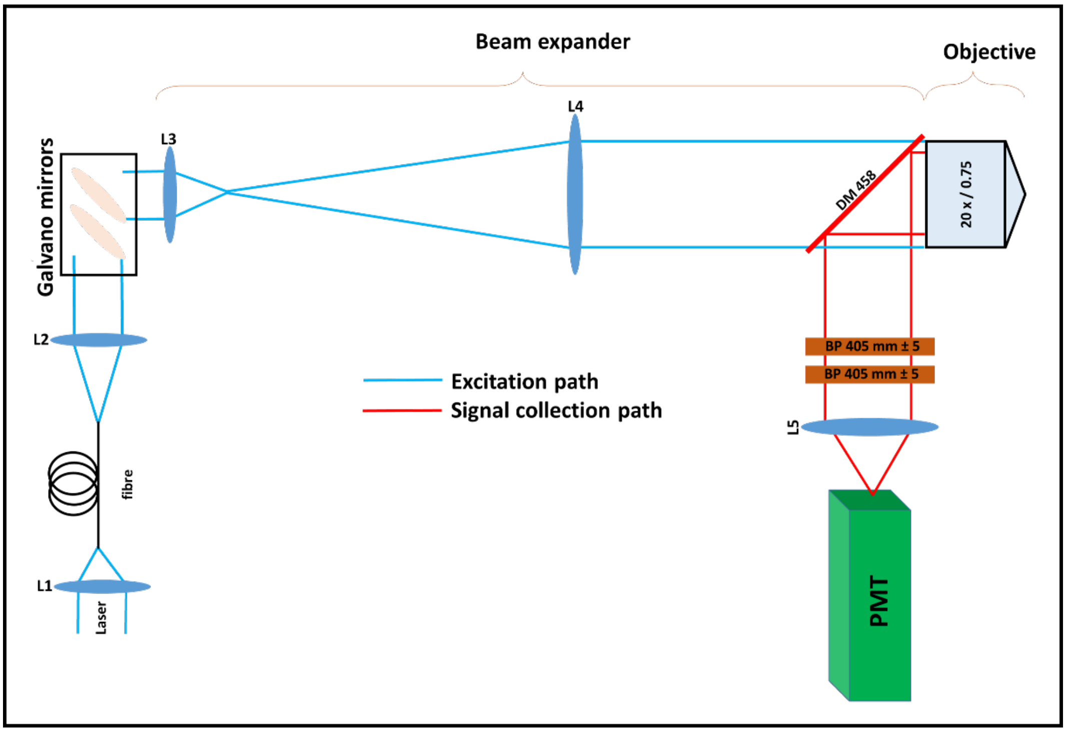
Beam expander
Objective
L4
L3
Galvano mirrors
DM 458
20 x / 0.75
L2
BP 405 mm ± 5
BP 405 mm ± 5
Excitation path
Signal collection path
L5
fibre
L1
Laser
PMT

Figure 4.2 Experimental HHM setup for free-space NDD. In this configuration the detection section (band pass filters, L5 lens and the PMT) is placed just behind the microscope objective. The dichroic mirror (DM 458) separates the signal from the excitation.

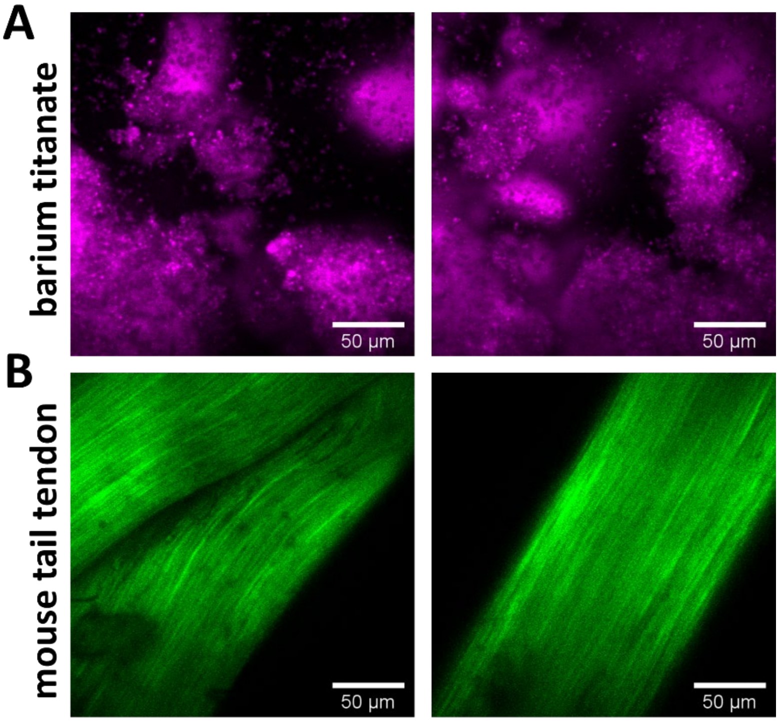

Figure 4.3 Images acquired with the HHM operating with the free-space NDD configuration of (**A** – top row) barium titanate crystals and (**B** – bottom row) mouse tail tendon samples using the SHG modality. Two different areas are shown for the same sample. Image parameters: 20x objective, pixels – 512 x 512, dwell time 32 µs, optical zoom x 3, ~ 20 mW average power on the sample.

4.3.2 Free-Space Descanned Detection

The excitation power experiences a huge drop upon passing through the beam expander in the HHM setup. Hence, it is to be expected that the collected signal strength will diminish on being collected in the back-reflection geometry encountering the beam expander and other optical components. The term "free-space descanned detection" (DD) indicates that scattered light is scanned on its way back to the detector and it travels in free space (air). Here, the detection unit that contains a dichroic mirror 485 (Semrock, FF458-Di02), two band pass filters, a focused lens (L5) and a PMT sensor, is placed right before the distal end of the DC-ARF (**Fig. 4.4**). The results obtained in this fDD configuration establish the decrease of the signal due to the length of the optical path and optical components. In addition, this data gives an indication of expected losses on coupling back to the fibre in the DD with a detection unit placed on the proximal end of the fibre, which is the operational configuration of the HHM that is aimed for this work.

The images were taken in fDD, using mouse tail tendon and barium titanate samples in SHG (**Fig. 4.5**), showed a decrease in the signal level compared to that obtained in NDD (**Fig. 4.3**). Nevertheless, the structural features of the samples are still recognizable, although, images look grainy due to a lower signal-to-noise ratio level caused by a longer detection path with more optical parts in on it.

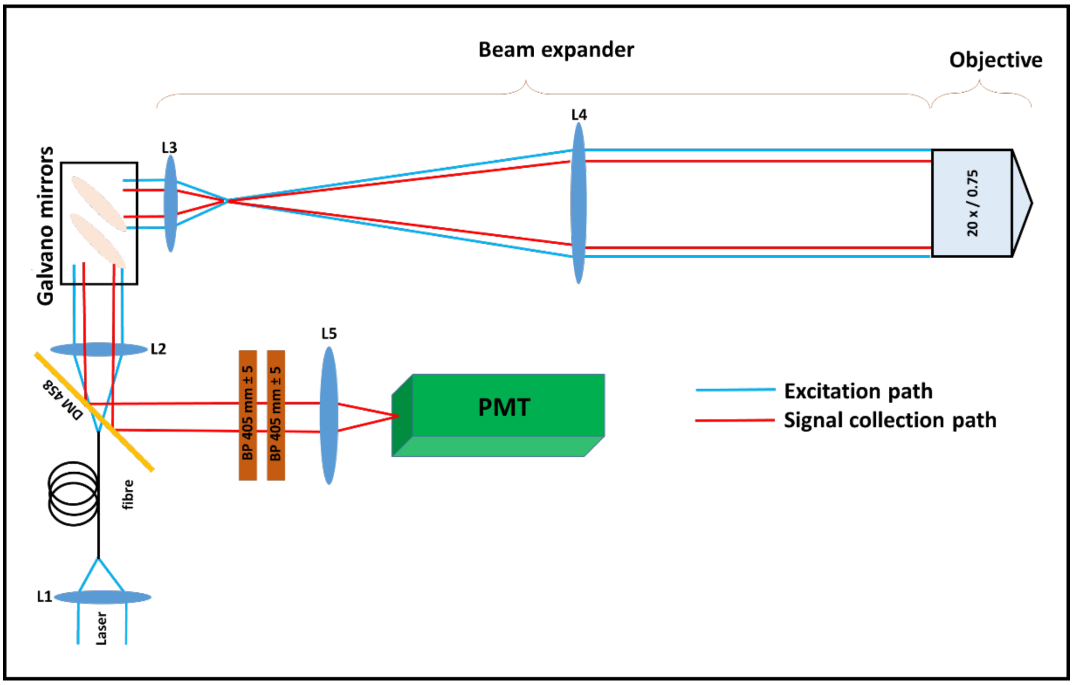
Beam expander
Objective
L4
L3
Galvano mirrors
20 x / 0.75
L2
L5
DM 458
BP 405 mm ± 5
BP 405 mm ± 5
PMT
Excitation path
Signal collection path
fibre
L1
Laser

Figure 4.4 Experimental HHM setup for free-space DD illustrates part of detection path (band pass filters, L5 lens, and the PMT) placed at the distal end of the fibre. The dichroic mirror (DM 458) separates the signal from the excitation light.

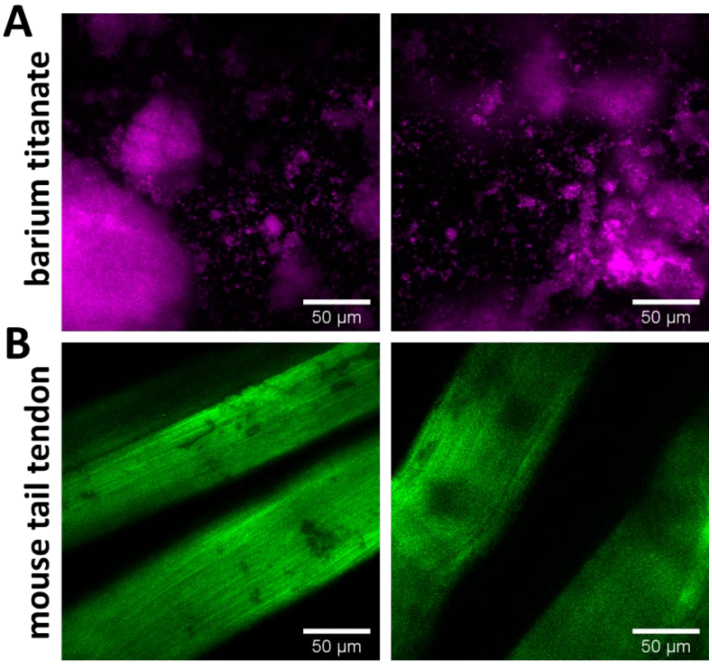
A
barium titanate
50 µm
50 µm
B
mouse tail tendon
50 µm
50 µm

Figure 4.5 Images obtained in the HHM operating with fDD mode of (A – top row) barium titanate crystal and (B – bottom row) mouse tail tendon samples using the SHG modality. Two different areas are shown for the same sample. Image parameters: 20x objective, pixels – 512 x 512, dwell time 32 µs, optical zoom x 3, ~ 20 mW average power.

4.3.3 Descanned Detection via Double-Clad Anti-Resonant Hollow-Core Fibre

Figure 4.6 presents DD via DC-ARF where the signal detection unit is placed at the proximal end of the fibre. Its main challenge is the optimization of the signal coupling to the fibre. The collection of the signal via the DC-ARF is not affected by dispersion or nonlinearity as well; similar to that observed with laser pulses. Hence, the only issue in the signal collection through the DC-ARF is the coupling efficiency related to a surface area of the waveguide and coupling conditions such as choice of the optical components. Here, supplementary lenses had to be added to the HHM setup in order to increase signal confinement upon its entry to the distal end of the DC-ARF. Therefore, the system configuration presented in **Figure 4.1A** had to undergo modifications to maximize signal coupling efficiency into the DC-ARF. Two additional lenses were employed in the system L6 (f = 19 mm), which collimated the light, and L7 (f = 25 mm) that formed a beam expander BE2 with L2 (**Fig. 4.6**). On comparison of the configurations shown in **Figures 4.1A** and **4.6**, it was found that higher signal is detected for the arrangement presented in **Figure 4.6**. However, added lenses (L6, L7) had an impact on the excitation beam. By creating a second beam expander BE2 with L2 and L7, the beam diameter increased from 1.16 mm to 1.5 mm, which affected the value of lenses (L3 and L4) required for building the first beam expander BE1. The new magnification of BE1 should be decreased from x10 to x7.3. Although the HHM setup configuration with two BE-s (**Fig. 4.6**) gave greater signal detection than that with one BE (**Fig. 4.1**) still challenges arose for this system arrangement. When the expended laser beam filled the back-aperture of the objective, obtained images showed a very low level of the signal. On the contrary, when the laser beam underfilled the back-aperture of the objective, it generated higher signal level images but with a restricted field of view (FOV).

The uneven illumination intensity may originate from the increased movement of the laser spot and beam clipping at the objective back aperture [19]. As the pathway for laser delivery and signal collection overlapped, the optical design of the HHM in this configuration became more complex thus requiring further consideration and an engagement of additional tools such as a computer simulation and more customized components.

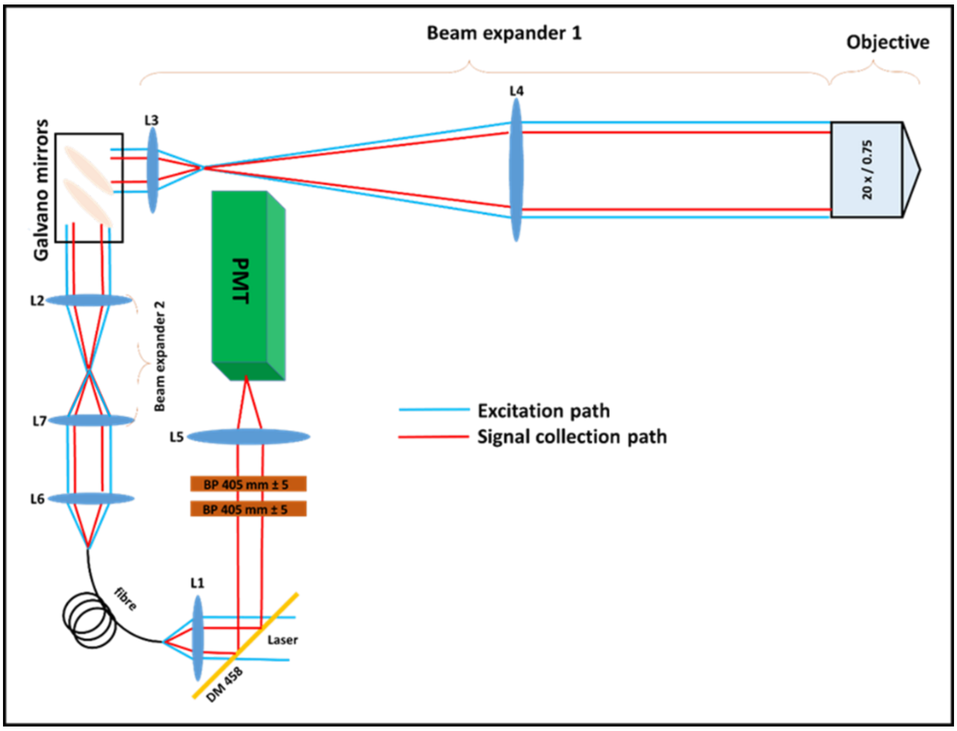
Beam expander 1
Objective
L4
L3
Galvano mirrors
20 x / 0.75
PMT
L2
Beam expander 2
L7
L5
Excitation path
Signal collection path
L6
BP 405 mm ± 5
BP 405 mm ± 5
L1
fibre
Laser
DM 458

Figure 4.6 Experimental HHM setup for DD via DC-ARF has detection section parts (band pass filters, L5 lens and the PMT) placed at the proximal end of the fibre. The dichroic mirror (DM 458) separates the signal collection path from the excitation path. Two additional lenses (L6, L7) were added for higher nonlinear signal coupling efficiency.

SHG images of barium titanate crystals (row A) with a single frame acquisition and mouse tail tendon (row B) with 3 averaged frames, all processed using Fiji software [89] are shown in **Figure 4.7**. To obtain high image quality, the mouse tail tendon sample required acquisition of multiple frames, which was not needed in the case of barium crystals sample that gives a stronger signal. The lower resolution of images are likely due to underfilled objective that leads to a lower effective NA.

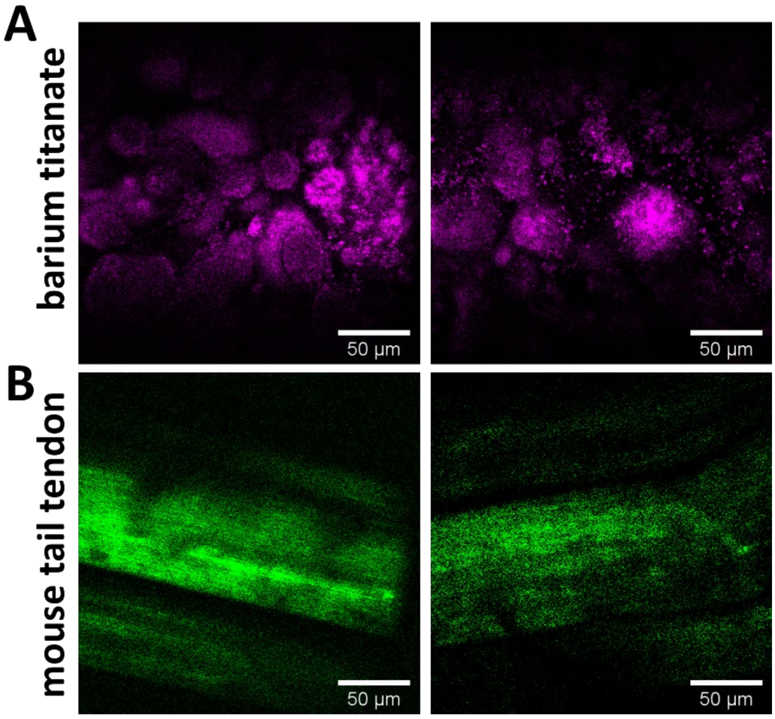

Figure 4.7 Images obtained with the HHM operating with DD via DC-ARF mode based of (**A**) barium titanate crystals (a single frame) and (**B**) mouse tail tendon (3 average frames) samples using the SHG modality. Image parameters: 20x objective, pixels – 512 x 512, dwell time 32 µs, optical zoom x 3, ~ 20 mW average power.

4.3.4 Comparison of Different Detection Configurations for Hand-Held Microscope

In this section the three detection configurations are compared on the basis of signal–to–noise ratio (SNR). SNR was estimated as per the method described in detail in Chapter 3.2.6. A well-distinguished signal from the noise is a key factor in evaluating new imaging devices and gives information on the quality of the system, proper alignment, and its sensitivity [23]. **Figures 4.8** and **4.9** present SHG images of barium titanate crystals and mouse tail tendon, respectively, taken using different signal detection arrangements (fNDD – **images A** , fDD – **images B**, and DD via DC-ARF – **images C, D**) with the same average power on the sample of ~20mW. All images were taken as a single frame, except for the mouse tail sample, which needed additional frames in DD via DC-ARF. A weaker SHG signal was observed in the DD via DC-ARF configuration, therefore 2 additional frames were included (**Fig. 4.9C**). The SHG images for mouse tail tendon samples are shown in **Figure 4.9** for 3 average frames **(C)** and 1 frame **(D)**. Gradual fall in the signal level is observed with fNDD and fDD; however, for DD via DC-ARF, it shows a dramatic drop (around 10 times).

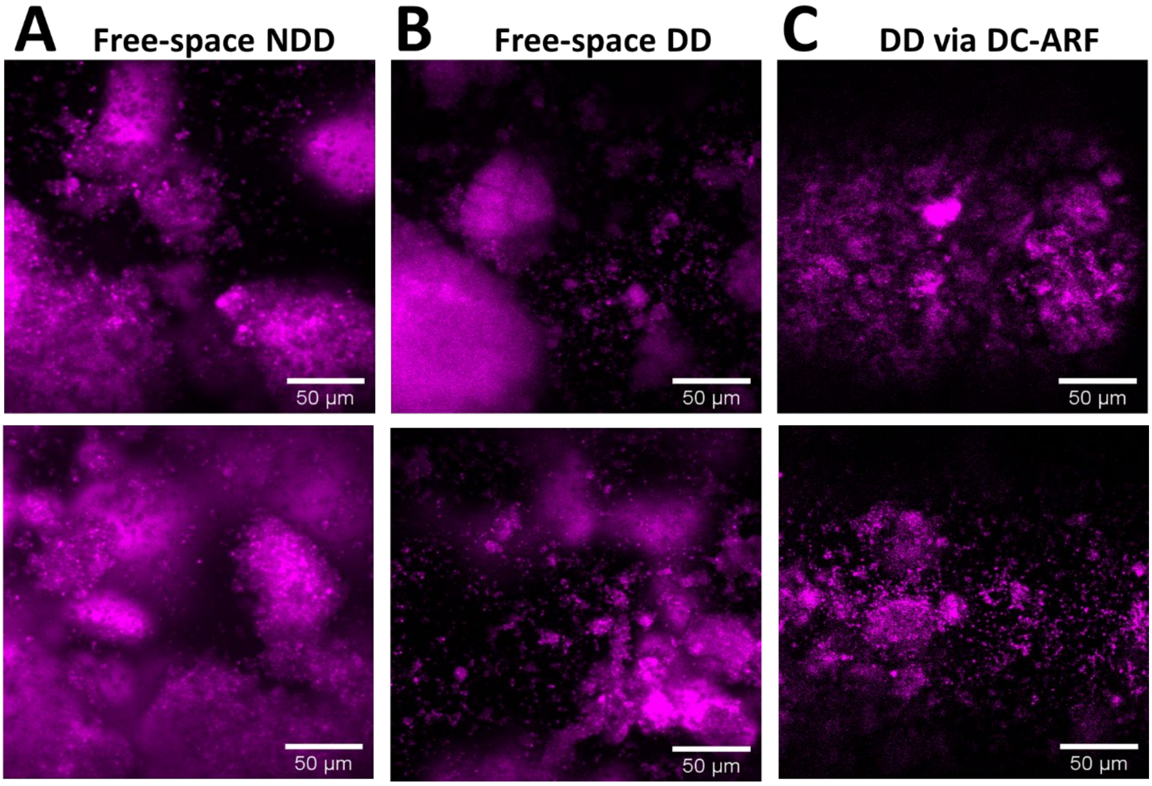
A
Free-space NDD
B
Free-space DD
C
DD via DC-ARF
50 μm
50 μm
50 μm
50 μm
50 μm
50 μm

Figure 4.8 SHG images of barium titanate crystals taken with the HHM system under three different types of detection configuration (**A**) fNDD, (**B**) fDD, and (**C**) DD via DC-ARF. Two representative images of different areas on the sample are shown for each configuration.

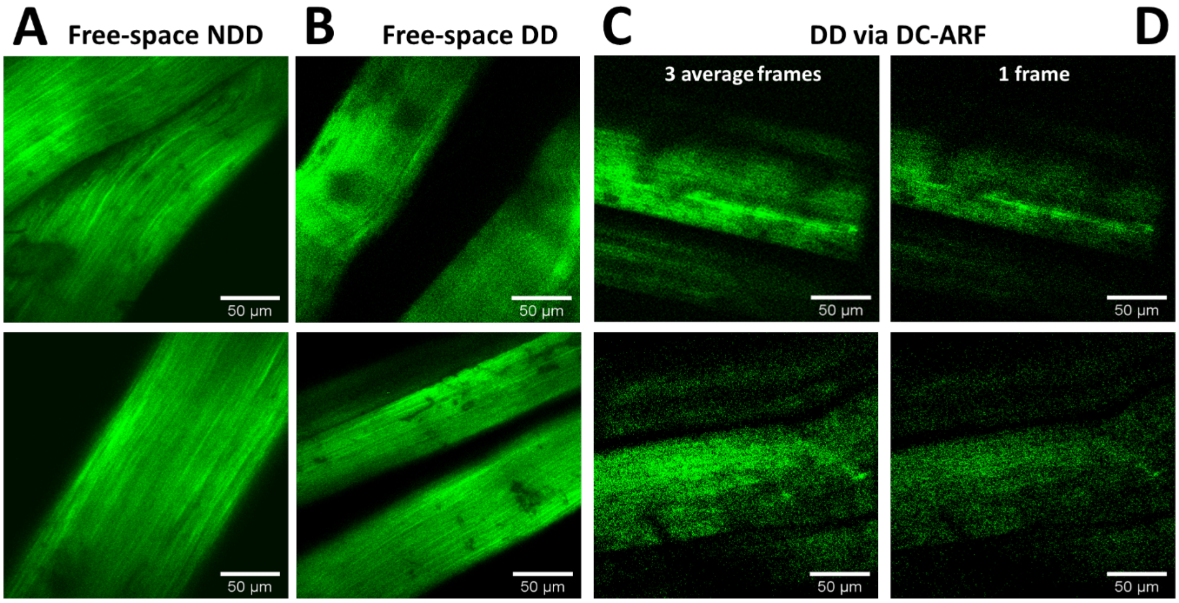
A
Free-space NDD
B
Free-space DD
C
DD via DC-ARF
D
3 average frames
1 frame
50 μm
50 μm
50 μm
50 μm
50 μm
50 μm
50 μm
50 μm

Figure 4.9 SHG images of mouse tail tendon taken with the HHM system under 3 different configurations: (**A**) fNDD, (**B**) fDD, and (**C**, **D**) DD via DC-ARF. Two representative images of different areas on the sample are shown for each configuration. For fNDD (**A**) and fDD (**B**) a single frame was acquired. For DD via DC-ARF images with 3 averaged frames (**C**) and 1 frame (**D**) are shown.

A quantitative comparison of the SNR for the three types of detection configurations (fNDD, fDD, and DD via DC-ARF) is shown in **Figure 4.10**. Images of mouse tail tendon taken from different regions of the sample with acquisition of a single (**image 1, 2, 3**) and 3 averaged frames (**image 4**) are shown. They were chosen such that they had clear signal and blank areas. Line profiles (white lines across images) are plotted in graphs A and B (**Fig. 4.10**). The grey value (**graph A**) and SNR (**graph B**) for fNDD (black curve) and fDD (red curve) are high and of comparable level, while DD via DC-ARF for 1 frame (green curve) and 3 average frames (blue curve) present over 100x signal loss for grey value (**graph A**) and 2x lower SNR (**graph B**) compare to the two other detection arrangements. Grey values for fDD (red curve, **graph A**, **Fig. 4.10**) indicate a good signal level at the entrance to the fibre, which gives an opportunity for higher signal coupling efficiency with carefully selected optics [31]. The main design of the system was based on the excitation path however, for overlapped excitation and collection path there are more parameters that need to be considered.

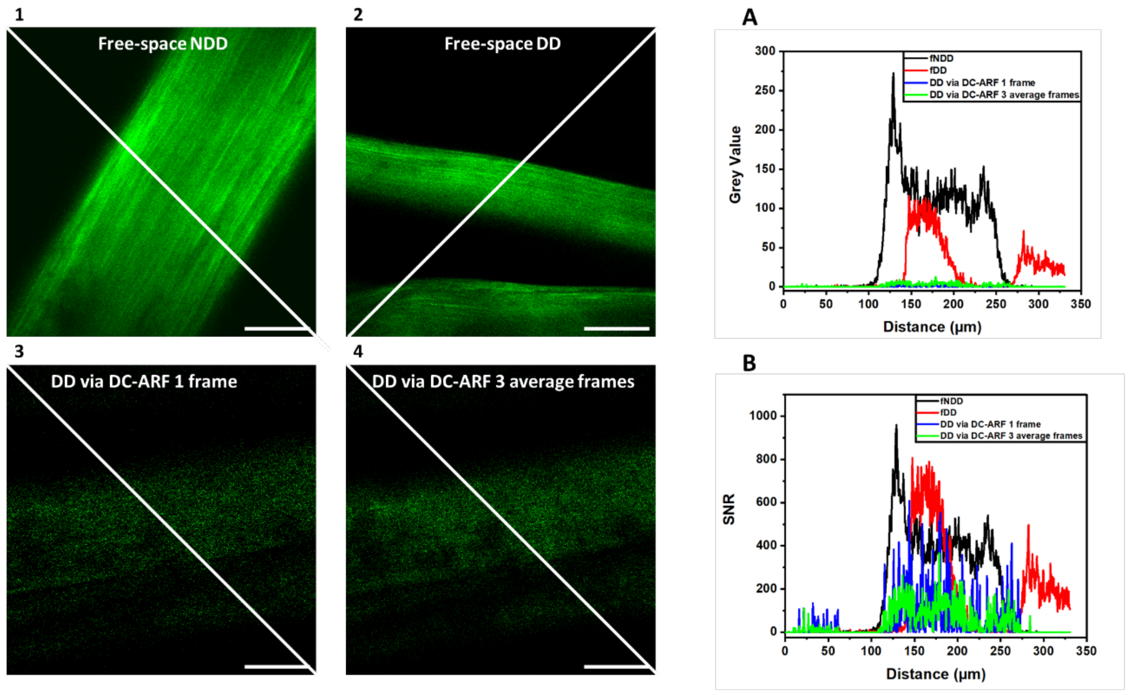

Figure 4.10 SNR analysis of four images of mouse tail obtained using HHM system in fNDD, fDD, and DD via DC-ARF signal collection configuration from different areas of the sample. **Images 1, 2, 3,** were taken with single frame acquisition, **image 4** was obtained with 3 averaged frames. **Graph A** presents grey value as a function of distance acquired along a white profile line seen on images. From these results in the **graph A**, SNR was calculated (**graph B**). Scale bar = 50 µm.

4.3.5 Hand-Held Microscope for Multiphoton Microscopy

The HHM system was investigated for different multiphoton microscopy MPM modalities. Here, the two-photon fluorescence (TPF) technique combined with SHG was explored using mouse bone and lung specimens (**Fig. 4.11**). Simultaneous performance of SHG and TPF provides different information of studied samples because they target different endogenous sources of signal in biological tissues. The main sources of fluorescence are NAD(P)H, flavins, retinol, and tryptophan found inside cells while elastin and collagen are responsible for TPF and SHG emission from the extracellular matrix [5, 6, 27].

Due to the limitation of the waveguide transmission window of the DC-ARF starting from ~790 nm, the applied excitation wavelength had to be above this wavelength, at the same time the 458 DM used in the detection unit of the system, restricted the collected signal to below 458 nm (**Fig. 4.11**).

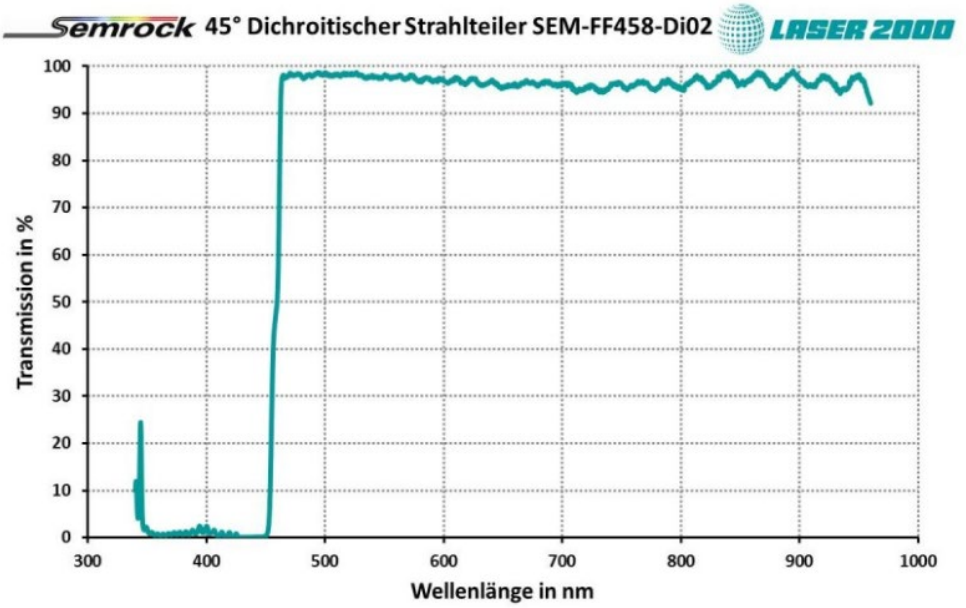

Figure 4.11 Transmission range of 458 nm long-pass filter (Semrock, FF458-Di02) used in the HHM system. The transmission band of DM affected the selection of TPF signal that could be collected from biological tissue.

These setup conditions allowed for imaging collagen in mouse bone and lung samples. Since both imaging techniques were targeting collagen, it was important to separate the SHG and TPF signal originating from the studied samples. Hence, for SHG excitation wavelength was chosen to be 810 nm and the signal was collected at 405 nm. In the case of TPF for collagen, the excitation wavelength can range between 820 – 900 nm, while the signal emission is at 450 nm [91]. Therefore, the chosen excitation wavelength for TPF was at 835 nm, and the 450 ± 5 nm (Thorlabs, FBH450-10) filter was used to separate out the signal for detection. **Figure 4.14** presents SHG and TPF images of collagen present in mouse bone (**A**) and lung samples (**B**) obtained from different area on the samples. Images were taken separately in the fNDD configuration (**Fig. 4.12 A1,2** and **B1,2**) and then merged (**Fig. 4.12 A3** and **B3**) using Fiji software and false-coloured (green for SHG, red for TPF) for distinguishing sample features targeted by these imaging techniques. The average power on the sample was ~ 30 mW.

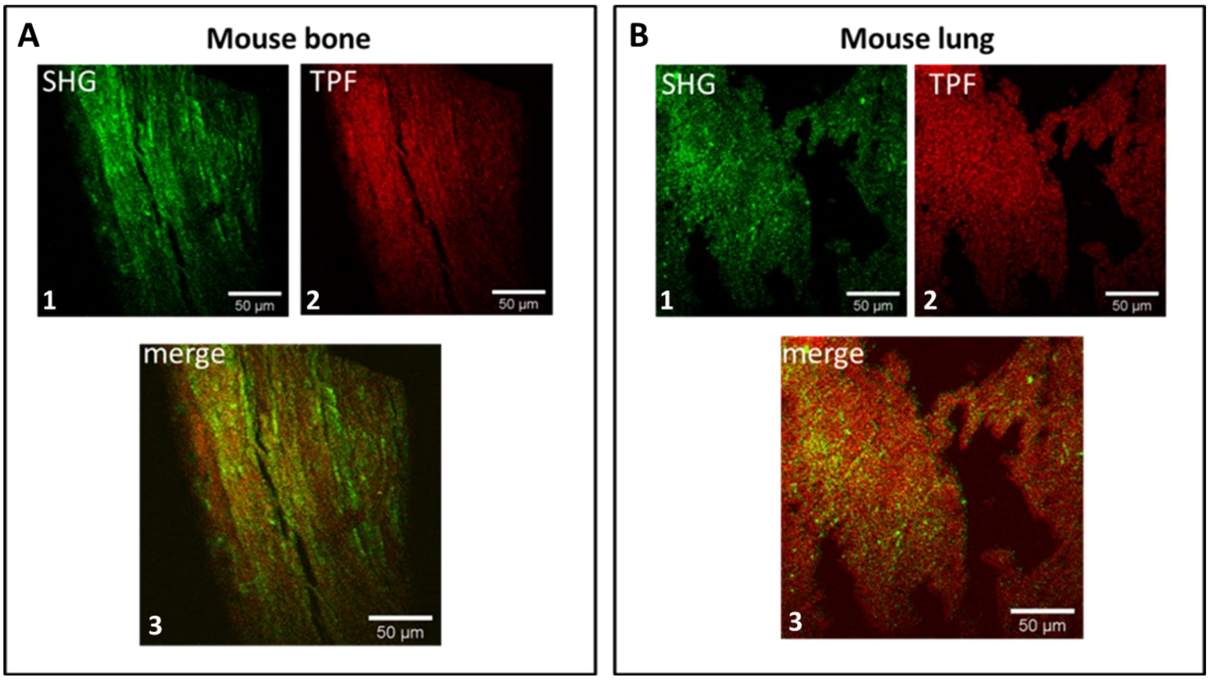

Figure 4.12 SHG and TPF images of mouse bone tissue (**A**) and mouse lung tissue (**B**) (separate (**1, 2**) and merged (**3**)). Excitation wavelength SHG – 810 nm, TPF – 835 nm; signal collection SHG – 405 nm, TPF – 450 nm; Power on the sample ~ 30 mW; Obj. 20x/ NA 0.75; Pixels 512 x 512; Dwell time 32000 ns; optical zoom 3.

4.3.6 Comparison of Hand-Held Microscope Performance with a Traditional System for Multiphoton Microscopy

Miniaturization and portability of the HHM comes with a trade-off in its performance compared to a standard benchtop microscope system. To benchmark the performance of the HHM system, SHG images of barium titanate crystals (**Fig. 4.13A**) and mouse tail tendon (**Fig. 4.13B**) were taken and compared with our lab-based laser scanning microscope for MPM. Although images taken with the HHM show higher SNR and lower resolution, they still present a high quality and recognizable collagen fibre structures. For reliable assessment comparison, two systems had to operate under the same imaging conditions, that is, similar detection configuration, objective, power on the sample, and even ambient noise background. Thus, the fNDD and Nikon (20x/75) objectives were utilized. In terms of power level on the sample, 20 mW was used in previous HHM tests, however, here 15 mW was selected. When higher power was used images were oversaturated when acquired with the benchtop setup and made them unsuitable for evaluation. On the other hand, 15 mW was not optimal power and more was required for the HHM system. The images seen in **Figure 4.13** for the HHM system show a decrease in signal level, higher noise captured in the process, and lower resolution. Further analytical evaluation of the SNR is demonstrated in **Figure 4.14**. Images of mouse tail were obtained from different areas of the sample using our benchtop microscope (**Fig. 4.14A**) and the HHM system (**Fig. 4.14B**) with the SHG technique. The grey value and SNR obtained along line profiles (white lines across images) are plotted in graphs 1 and 2 (**Fig. 4.14**). Although visual inspection of images taken with benchtop microscope and the HHM (**Fig. 4.13**) were less indicative it can be seen from **Figure 4.14** that the grey values and SNR for benchtop setup is at least 8x (**graph 1**) and over 25x (**graph 2**) better, respectively, than the HHM system. However, due to the power level mismatch for each setup the evaluation reports an overperformance of the benchtop system and underperformance of the HHM. Grey values for the HHM with fNDD configuration presented in **Figure 4.10** are around 150 for 20 mW power while here for 15 mW it dropped to 50. This is partly due to the non-linear nature of the process which is highly dependent on intensity.

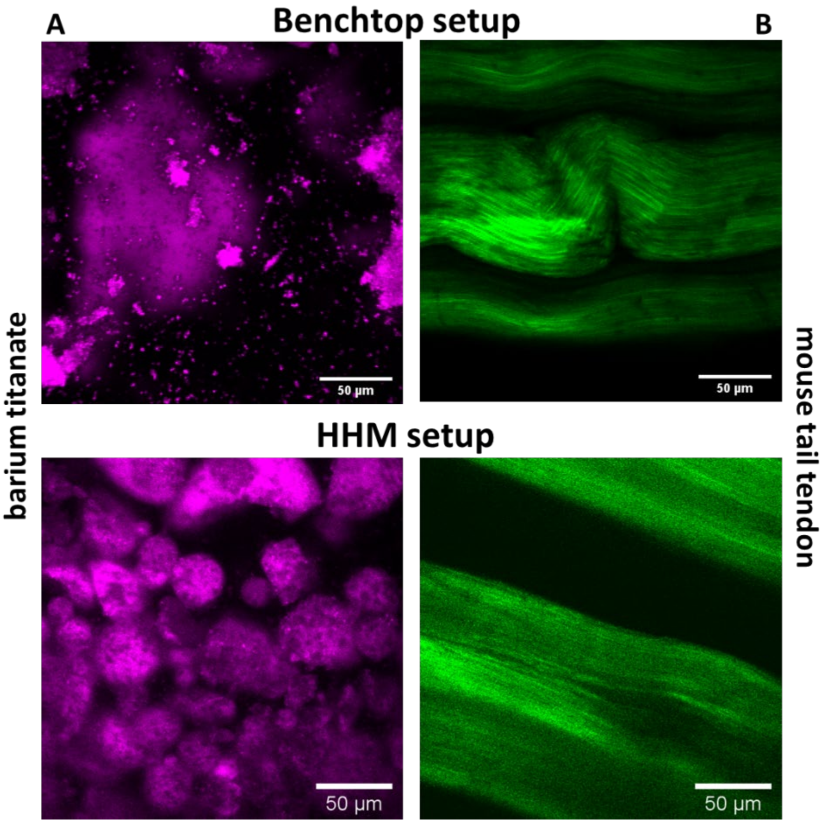

Figure 4.13 Comparison of HHM performance in fNND configuration with benchtop microscope system using barium titanate crystals (**A**) and mouse tail tendon (**B**) samples. Two representative images of different areas on the sample are shown for each setup. Technique SHG; Excitation wavelength 810 nm; signal collection 405 nm, Power on the sample ~ 15 mW; Objective 20x / NA 0.75; Pixels 512 x 512; Dwell time 32000 ns; Optical zoom 3.

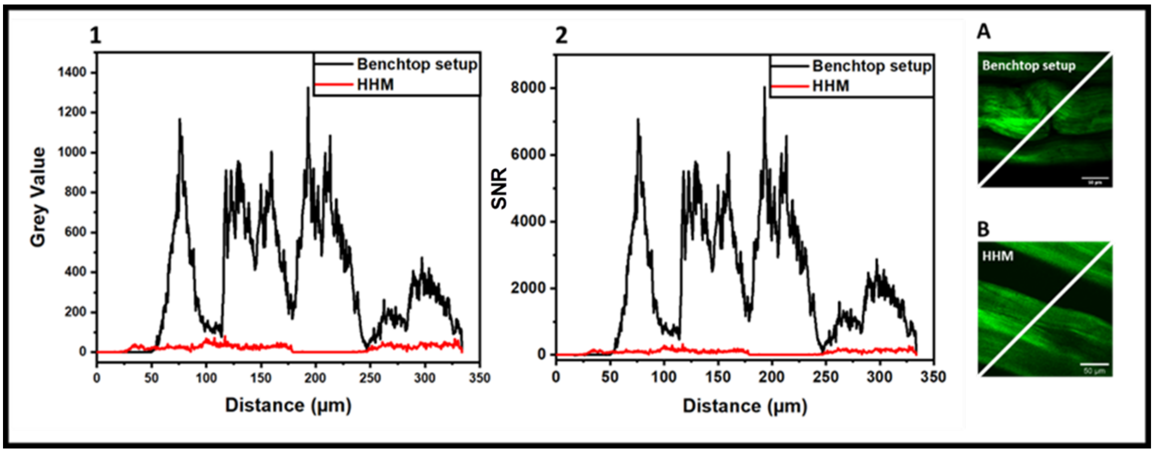

Figure 4.14 SNR analysis of SHG mouse tail images obtained using benchtop multiphoton microscopy system (**A**) and HHM system (**B**) in fNDD, detection configuration with average power on the sample ~15mW. Graph 1 presents grey values as a function of distance acquired along a white profile line seen on images. The SNR calculated from these imaging results is shown in graph 2.

4.4 Conclusions

This chapter presented the work on the development of a handheld fibre microscope for nonlinear label-free imaging, in which DC-ARF was used for laser pulse delivery and signal collection. Its design was based on a standard laser scanning microscope. The imaging device is lightweight, miniature, and can operate remotely. Performance of the HHM system in three detection configurations (free-space NDD, free-space DD, and DD via DC-ARF) was evaluated using a variety of samples such as collagen in mouse tail tendon, or bone, with SHG and TPF imaging techniques, and SNR analyses. The study demonstrates the ability of the HHM system to acquire high-quality images using low power in free-space NDD and DD. SNR was severely deteriorated in the DD via DC-ARF configuration by 11 times and 9 times compared to free-space NDD and DD configurations respectively. This was primarily attributed to coupling related losses both for the excitation and the signal. Although the objectives of this chapter were achieved, the DD via DC-ARF configuration (preferred operation mode of HHM) requires further development in terms of higher signal coupling efficiency. Computer modelling and customized optical components will be helpful to optimise the system further. Nevertheless, the knowledge and experience on the miniaturization and portability of the imaging system will be adopted and developed further in the next chapter. It will describe the construction process of a micro-endoscopy system with DC-ARF for multiphoton, and label-free imaging.

Chapter 5 Probe for Multiphoton Endoscopy with Double-Clad Anti-Resonant Hollow-Core Fibre

5.1 Introduction

This chapter presents the work on the development of the probe for multiphoton endoscopy (MPE) with the Double-Clad Anti-resonant Hollow-Core Fibre (DC-ARF). In endoscopy, the usage of fibre optic allows for remote and portable operation of the device. Over the course of this project, the DC-ARF underwent various tests that were designed to evaluate its suitability for multiphoton micro-endoscopy. The undistorted pulse laser delivery to the sample was assessed in measurements of dispersion and nonlinearity, while signal collection in epi-detection was investigated in experiments with descanned detection using a traditional microscope setup. Here, as the final stage of this project, the process of construction of the micro-probe will be described and discussed. When designing a micro-probe, one should consider basic requirements for *in-vivo* endoscopy that are its miniaturized dimensions, flexibility with portability, large field of view, high spatial resolution, and frame rate. These features constrain the selection of micro-parts of the probe such as a scanning mechanism, and an optical focusing system. The above were taken into consideration to build an endoscope probe along with the hardware and software to control the motion of the scanner and reconstruct an image.

The second part of this chapter is concerned with the evaluation of the micro-endoscopic system for label-free nonlinear imaging of biological samples using the second harmonic generation (SHG) technique. To maintain consistency with the previous results presented in this thesis, mouse tail tendon and barium titanate crystals samples were utilized as imaging targets. The evaluation of system performance was carried out on the basis of signal-to-noise ratio and resolution. Furthermore, due to ununiformed sampling point’s distribution, Not a Number (NaN) values appeared leading to poor image quality. This work also presents the methods for decreasing the effect of such artefacts (due to NaN values).

5.1.1 Aim and Objectives

Aim: To construct micro-probe for multiphoton endoscopy with DC-ARF.

Objectives:

1. Build the head of the probe and develop control software for micro-endoscopic system
(i) Mounting and calibration of the piezo tube actuator,
(ii) Selection and assembly of the micro-objective,
(iii) Development of the imaging system code in the Labview for control of the scanning process, optical signal measurement, and image reconstruction.
2. Evaluation of micro-endoscopic system for nonlinear imaging
(i) Acquisition of SHG images of biological and non and evaluation using SNR and resolution,
(ii) Implementation of methods to reduce the effect of NaN values on image quality.

5.2 Development of the Probe for Multiphoton Endoscopy

5.2.1 Fibre Scanner

The central part of the probe for the multiphoton endoscopy (MPE) constitutes a fibre scanner (FS) that is made of fibre optic and piezoelectric actuator placed concentrically with the optical axis at the distal tip of the endoscope. The resonating device employs a single optical fibre that guides the excitation light, collects the signal, and acts as a laser scanning source. Here **(Fig. 5.1)**, the DC-ARF was threaded through the piezoelectric tube (PZT) scanner, and its free-standing part was deflected by the resonated PZT driven by an electric voltage at the fibre resonance frequency. To increase fibre alignment with the optical axis of the probe, 3D printed adaptors were installed on both ends of the PZT. The fibre was positioned through 0.4 mm holes drilled in the adaptors had drilled holes of 0.4 mm, leaving over 0.1 mm extra space between the fibre and the opening. The fibre was fixed inside the adaptor using a commonly available clear nail varnish. This allowed for building and testing multiple fibre scanner (FS) assemblies without damaging the PZT when changing from one fibre to the other.

Four wires were soldered to the PZT electrodes to deliver waveforms that would move the FS in a given scan pattern. Undisturbed FS resonance was achieved by implementing a 3D printed collar fixed at the proximal end of the PZT. The final design of the probe will contain the external tube to provide stability and protect internal parts from damage.

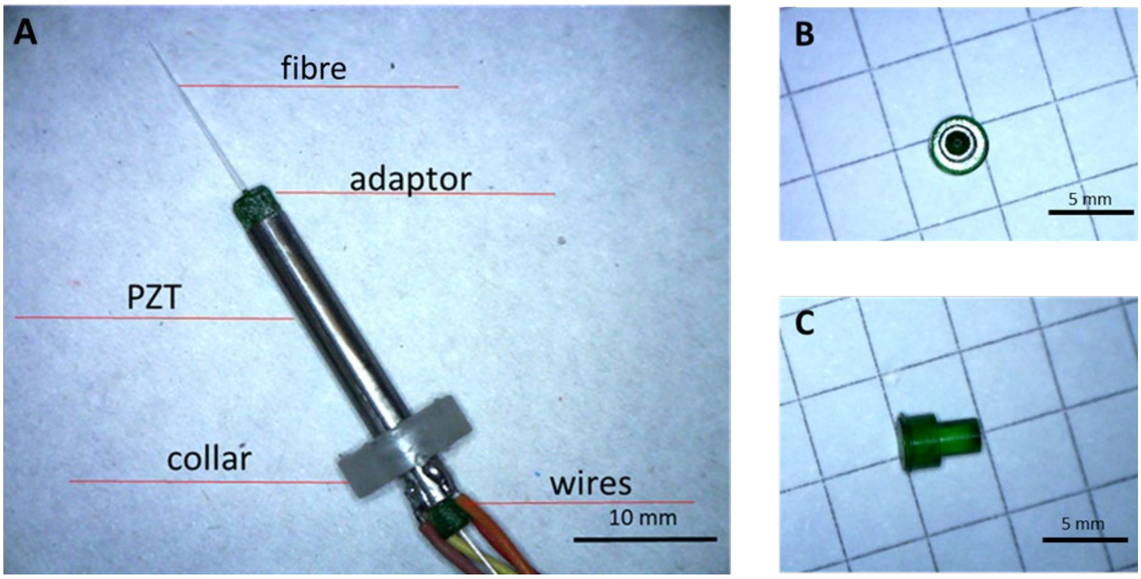

Figure 5.1 (A) An assembled scanner. The main components are: PZT, fibre optic, adaptors, wires, and collar; **(B-C)** 3D printed adaptors used to increase fibre alignment with the main axis of the probe (top and side view).

Piezoelectric Actuator

The scanner used in this work, was a piezo tube (PT230.94, Physik Instrumente (PI)) of the following dimension: length 30 mm × outside diameter 3.2 mm × inside diameter 2.2 mm. The material used for its production was the ceramic type PIC255 (a modified Lead Zirconate Titanate). The four metal film bands of electrodes (**Fig. 5.2A** a, b, c, and d) made of CuNi and Au on the outer surface of the PZT enable deflection in two lateral directions. The inner electrode **(Fig. 5.2 Ae)** inside the PZT serves as ground.

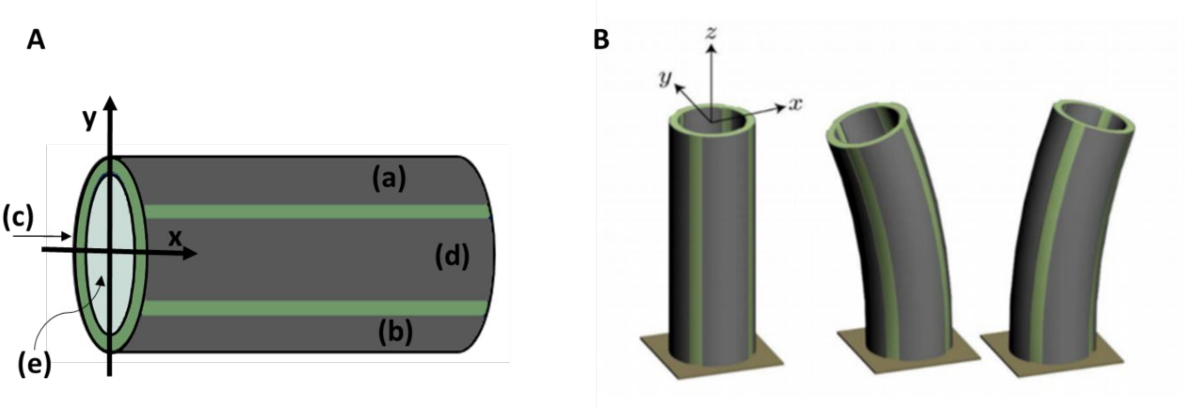

Figure 5.2 (A) The structure of the piezoelectric tube contains four isolated electrodes (a-d) on its external surface, and the inner electrode (e) serves as ground; **(B)** Deflection of the PZT in response to the applied external voltage (adapted from https://www.piezodrive.com).

The PZT's displacement results from the applied external voltage that is transformed into mechanical strains of the actuator. Two opposite pairs of electrodes (a-b) and (c-d) can be compressed or expanded depending on the signal configuration voltage **(Fig 5.2B)**. One electrode in each pair receives positive voltage $V_x(t)$ while the other has negative voltage $-V_x(t)$ so that the actuator will undergo deflection in one orthogonal direction. PZT displacement can be calculated for different voltage levels along the x-axis using the formula given below (23) [92]:

$$\Delta x(t) = V_x \frac{2\sqrt{2}d_{31}L^2}{\pi D h} \tag{23}$$

Where:

$\Delta x(t)$ - the deflection on the x-axis,

V_x – the applied voltage,

d_{31} - the piezoelectric strain constant ($d_{31} = 180$ pC/N for the PIC255 ceramic),

L - the length of the tube (30 mm),

D – the outside diameter (3.2 mm),

h - the tube thickness (1 mm).

According to the PZT technical specification, at maximum operational voltage ± 250 V, the maximum PZT deflection is ± 35 μm.

5.2.2 Spiral Scanning Pattern Generation

Resonance Frequency

In order to generate a two-dimensional image, an appropriate scan pattern needs to be selected that is suitable for implementation on the chosen scanner. PZT actuator can generate a variety of different scan patterns such as raster or Lissajous [74], which were described in the previous section of this thesis. However, the most optimal scan scheme for a tubular actuator is an expanding spiral pattern that can be produced by two sinusoidal driving voltages with linearly modulated amplitudes. Their generation will be discussed in the next subsection. The resonant fibre scanning at its resonant frequency can sweep a very large field of view with reduced actuator voltages. The resonance frequency f_{RES} can be determined theoretically by using the formula below (24) [93]:

$$f_{RES} = \frac{\beta}{4\pi L^2}\sqrt{\frac{ER^2}{\rho}} \tag{24}$$

Where:

$\boldsymbol{\beta}$ - constant related to the order of the resonance,

$\boldsymbol{E}$ – Young modulus of fibre material,

$\boldsymbol{R}$ – radius of the fibre,

$\boldsymbol{\rho}$ – fibre density,

$\boldsymbol{L}$ – free-standing length of the fibre.

Parameters related to fibre dimensions such as its radius, density, and length will affect the f_{RES}. When designing the fibre scanner (FS), one needs to consider the relation of the fibre length to the field of view (FOV) and the image acquisition time. A longer fibre arm is related to lower f_{RES}, this means that resonant scanning with longer fibre segment will allow in achieving larger FOV but at the cost of the increase in acquisition time.

The DC-ARF is made of silica glass, with a density $\boldsymbol{\rho}$ of 2.65 g/ cm^3**;** however, this value cannot be used for the DC-ARF due it hollow core. The appropriate $\boldsymbol{\rho}$ magnitude was calculated as 2.22 g/cm^3. The length of the fibre's arm should be kept to its minimum due to the need for miniaturization of the probe head dimensions. Here, f_{RES} were calculated using the formula above (24) for six different fibre arm lengths within the range of 5 to 30 mm, and presented in **Figure 5.3 (A)**. The figure shows a rapid increase in f_{RES} with shorter fibre lengths.

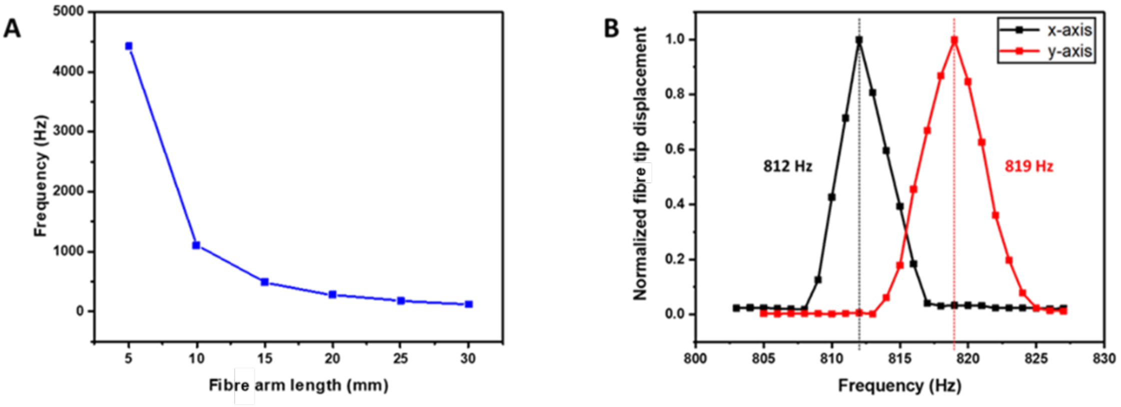

Figure 5.3 Resonance frequency for free-standing fibre in the endoscopic probe; **(A)** Evolution of the calculated resonance frequency as a function of the length of free-standing DC-ARF; **(B)** Experimentally measured resonance frequencies of two axes for fibre resonator were found to be 812 Hz for the *x*-axis and 819 Hz for the *y*-axis.

The optimal free-standing fibre length of 12 mm was identified after a series of experiments. Few lengths of the free-standing fibre between 8 – 25 mm were selected, and their maximum displacement was measured. The amplitude of displacement of 12 mm fibre arm for the *x*- and *y*-axis at its resonance frequency was experimentally measured at 812 Hz and 819 Hz respectively with a 7 Hz difference between the axes **(Fig. 5.3B)**. Optimally, fibre deflection in two lateral directions should be of the same value. However, this was not achieved due to asymmetry from the main axis of the probe.

The quality of the resonator is defined by the dimensionless $\boldsymbol{Q}$ factor that is the ratio of resonance frequency ($\boldsymbol{f_{RES}}$) to the FWHM of its bandwidth ($\boldsymbol{\Delta f_{RES}}$) (3) [94]. The higher value of the $\boldsymbol{Q}$ factor indicates the weaker ability of the resonator to damp and better quality of the resonance.

$$\boldsymbol{Q = \frac{f_{RES}}{\Delta f_{RES}}} \tag{25}$$

The approximate $\boldsymbol{\Delta f_{RES}}$ and calculated $\boldsymbol{Q}$ factor for the x-axis is 4.2 Hz and 193, and for the *y*-axis 5.2 Hz and 156, respectively. $\boldsymbol{Q}$ factor reported in the literature for similar systems was over 200 [80]. For the hollow core Kagome fibre, Q factor of 173 has been reported [41], which is close to the value of 175 that was obtained in this work. High Q factor accounts for the more stable resonator however, the system is also more susceptible to whirling effect, which will be addressed in the next section.

Spiral Scan

The spiral scan is generated by two sine waves that are modulated in time with a linearly modulated amplitude and a π/2 phase-shift between them **(Fig. 5.4)**.

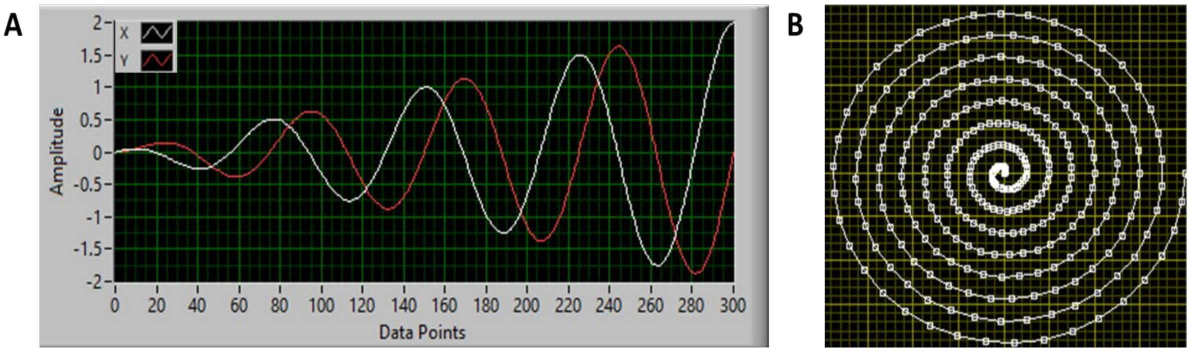

Figure 5.4 Schematic representation of the spiral scan formation; **(A)** Two sine waves with a linearly modulated amplitude and 90° phase shift creates a spiral pattern **(B)**.

Figure 5.5 graphically demonstrates the construction of the linearly increasing sine function as a result of the multiplication of a ramp and a sine wave.

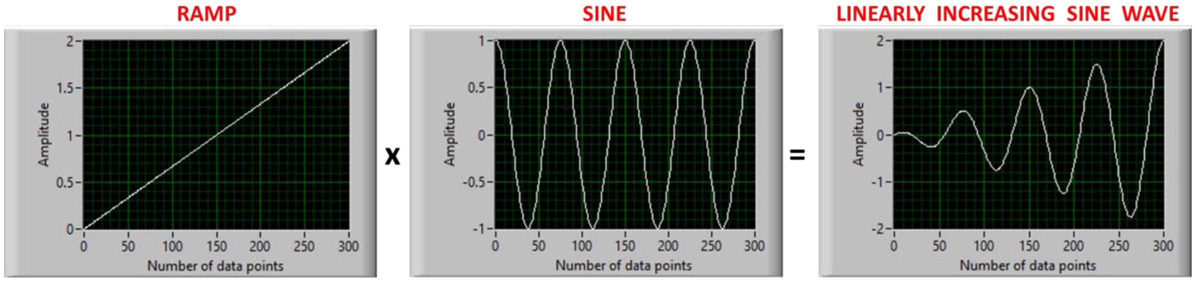

Figure 5.5 Formation of the linearly increased sine wave from ramp and sine function.

When two opposite pairs of electrodes of the fibre scanner are driven by modulated sine waves with a 90° phase, fibre performs circular oscillations expanding outwards from the main axis of the probe. The f_{RES} of the fibre and the maximum amplitude of the signal set the diameter of the spiral. The signal is collected during the period of spiral expansion indicated by the image scan period in **Figure 5.6**. A non-imaging period is required to allow for the fibre to return back to its initial point before taking the next image. As a result, any residue oscillation can be carried over to the next frame and can cause image deformation. Upon completion of the spiral scan, therefore, a damping signal (active braking) and free decay intervals are added to the driven waveform sequences (**Fig. 5.6**). Firstly, the active breaking period reverses fibre motion by changing its phase and removing 95% of fibre rotation in 5 to 30 cycles, moving fibre to the centre of the spiral scan. Secondly, free decay interval allows the remaining oscillations to perish, until fibre returns to its zero point and is ready for the next frame. **Figure 5.6** presents the full amplitude–modulated signal that drives the fibre scanner with all three phases, covering a single frame.

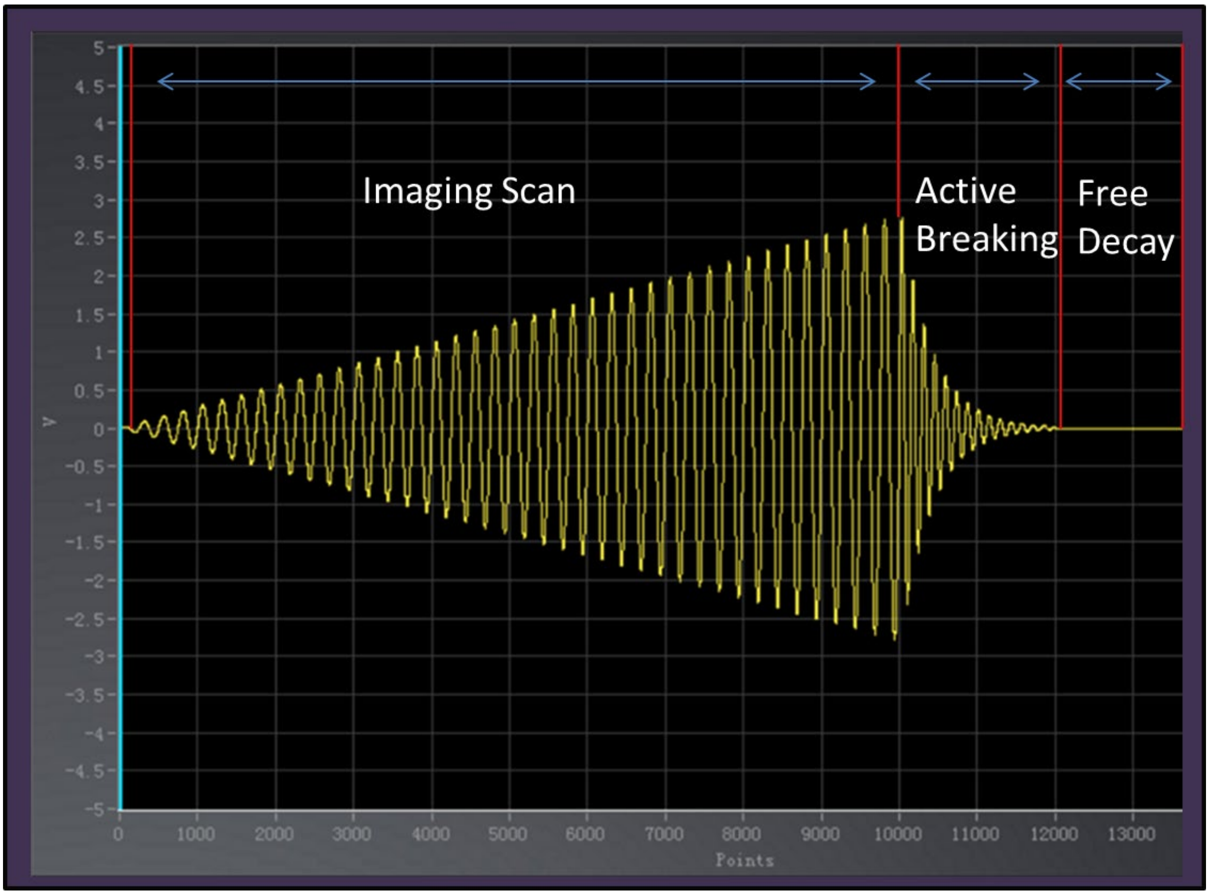

Figure 5.6 The amplitude-modulated signal drive of the fibre scanner. It contains three periods: imaging scan, active braking, and free decay. The imaging scan period sweeps the sample area and fibre collects the signal, while active braking and free decay return the fibre to its initial position and remove residual oscillations.

Calibration of the Spiral scan

Image obtained with a resonant scanning fibre is sensitive to distortions. Stretching and swelling of the image centre appear due to deviation between the actual and expected fibre trajectory. For spiral scan generation, one needs to learn about the sources that may cause distortions in order to control and mitigate their impact on image quality. **Figure 5.7** presents two outgoing spiral signals: the first was generated by the waveform generator (grey curve) and the second plot (red curve) is the fibre actual deflection registered by Position Sensitive Detector (PSD). The PSD identifies the position of the laser beam by measuring and recording the fibre tip motion instantly. The fibre oscillations did not follow a linear modulated ramp because of the transient state of the system. Its duration is related to the ***Q*** factor and lasts longer than the spiral time meaning that the transient regimes are inevitable.

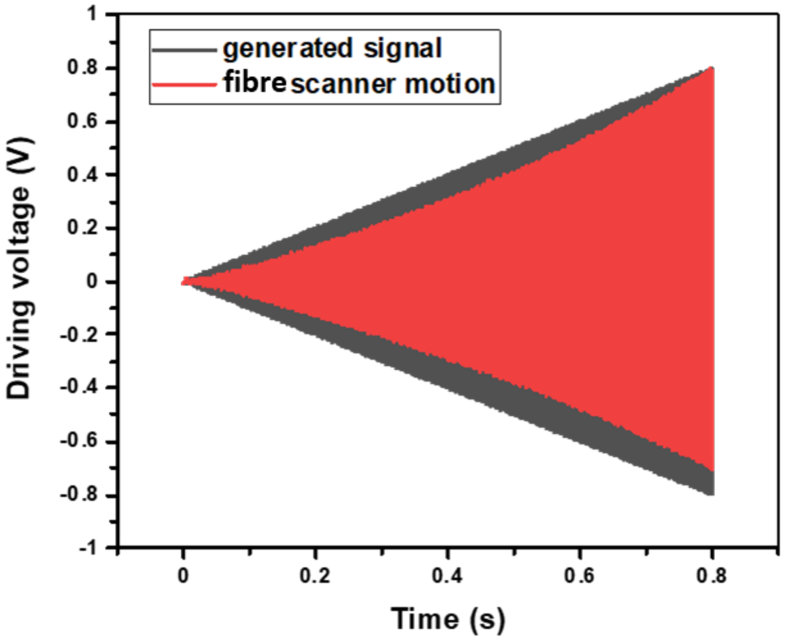

Figure 5.7 Red curve plot represents the fibre tip motion in response to a generated signal (grey curve). The transient regimes at the beginning of the outgoing spiral indicate a high ***Q*** factor.

The second source of these variations lays in the sensitivity of the fibre scanning system to asymmetry. Ideally, all parts in the probe should be concentric with its main axis. However, the asymmetry in the real system can originate from each component of the probe. For example, the position of the PZT electrodes and wires on the probe can create imperfections in the circular symmetry of the system. This leads to a strong coupling between the x- and y-axis and results in the whirling of the resonator. When a single electrode oscillates at its resonance frequency or close to it, it experiences a cross-coupling with the inactive axis and starts performing an elliptic trajectory **(Fig. 5.8A 1-2)**. Nevertheless, at off-resonance frequencies, fibre starts following the line scan with smaller displacement **(Fig. 5.8A 3-4)**. **Figure 5.8A 1-2** presents a cross-coupling event for individual x and y electrodes driven by sine wave and registered with a camera. The same results are observed for the linear modulation ramp recorded with the PSD in **Figure 5.8B 1-2** and its absence **(Fig. 5.8B 3-4)** when moved away from f_{RES}.

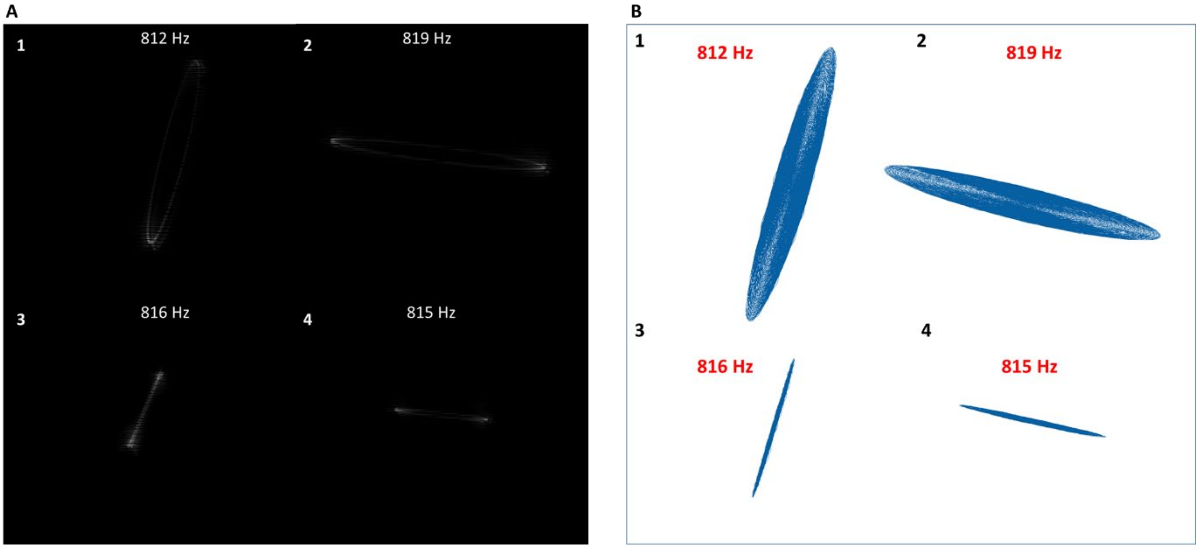

Figure 5.8 Whirling effect of the fibre resonator: **(A) 1-2** Cross-coupling of axes *x* and *y* when individual electrode resonated at its f_{RES} resulting in the elliptic trajectory; **(A) 2-3** Using off-resonance frequencies causes electrodes to follow line scan with a smaller displacement; **(B)** Whirling effect registered with the PSD, here single fibre axis was driven by a linearly increasing sine wave **1-2** at fibre resonance and **3-4** off fibre resonance.

The cross-coupled response of the fibre can be eliminated by exciting it in two independent and orthogonal pivots that correspond to the eigen directions of the fibre scanner (FS) [41]. Oscillating real electrodes (X, Y) of the PZT along the eigen directions will create two pairs of virtual electrodes (X_V, Y_V). This will break the coupling between real electrodes and bind them to their virtual counterparts. Removing of the whirling effect occurs when the virtual electrodes X_V and Y_V are driven at the mechanical resonance of the FS and the value of the θ angle is corrected until the individual electrode will follow a line scan **(Fig. 5.9)**.

Due to the time limitations, this method was not explored and deployed in this project instead just phase was used to obtain a circular patter as described below.

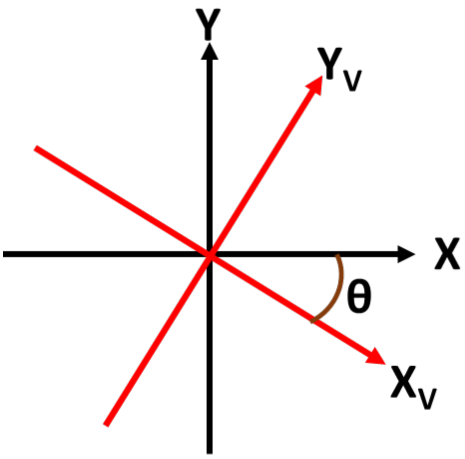

Figure 5.9 Elimination of the whirling effect by creating two virtual axes X_V and Y_V, and changing the θ angle between them and the real pair electrodes X, Y.

The premise of the resonating fibre scanner is the excitation at the same f_{RES} in both directions. However, asymmetry in the actualised system cause discrepancies between the value of f_{RES} for the *x*- and *y*-axis. This will generate phase shifts on each of them and create an elliptical pattern **(Fig. 5.10A)**. Adding an extra phase value to one of the electrode axes resolves the pattern imperfections and produces a circular scan **(Fig. 5.10B)**.

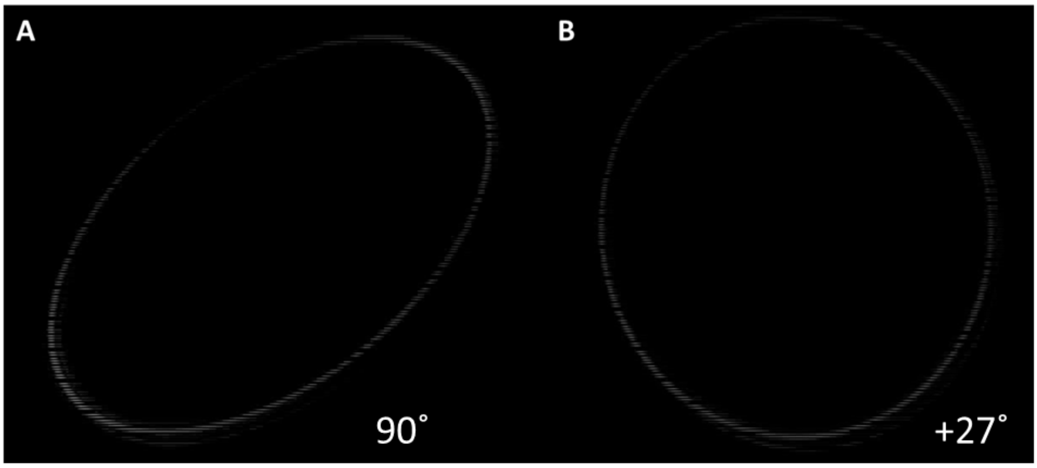

Figure 5.10 Correction of the phase deviation by adding extra phase value to obtain the circular pattern; **(A)** A circular scan with a 90° phase shift between two electrodes performs an elliptic trajectory; **(B)** an additional 27° removes the elliptic shape and corrects it to obtain a circular scan.

Maintenance of high image quality using a resonance fibre scanner requires calibration of the scan pattern. In this work, the spiral scan was created by the means of waveform parameters such as amplitude, frequency, and phase using a Lab View program. The signal obtained with this method lacks a non-imaging period and hence can resulting distortions at the beginning of each frame. The final waveform shape is the result of three separate signals (imaging, braking and decay part) however, due to time constraints only first segment of the waveform, which was sufficient to allow image construction was implemented to provide proof-of-concept. An example of the fibre scanner oscillation detected by the PSD is a position vs time plot **(A)** and the *x-y* plane **(B)** are presented in **Figure 5.11**.

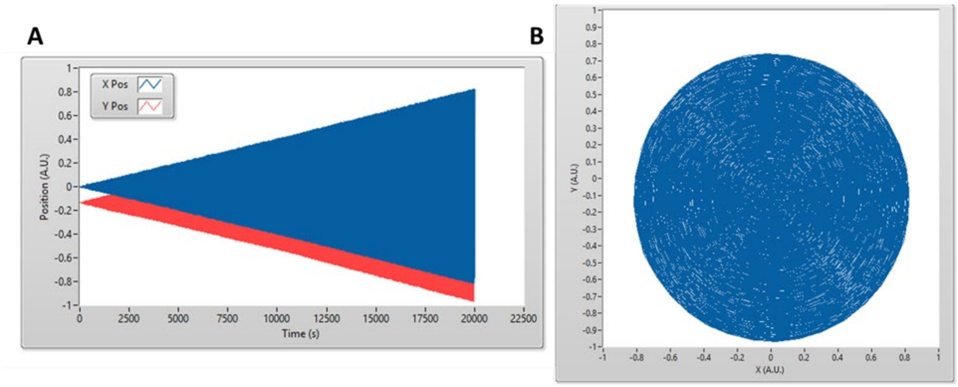

Figure 5.11 Registered spiral scanning pattern of the fibre scanner; **(A)** The PSD registers the *x* and the *y* position of the rotating fibre scanner with time; **(B)** spiral scan in the *x*-*y* plane.

Figure 5.12 is an example image of a motionless **(A)** and resonating fibre-optic cantilever **(B)**

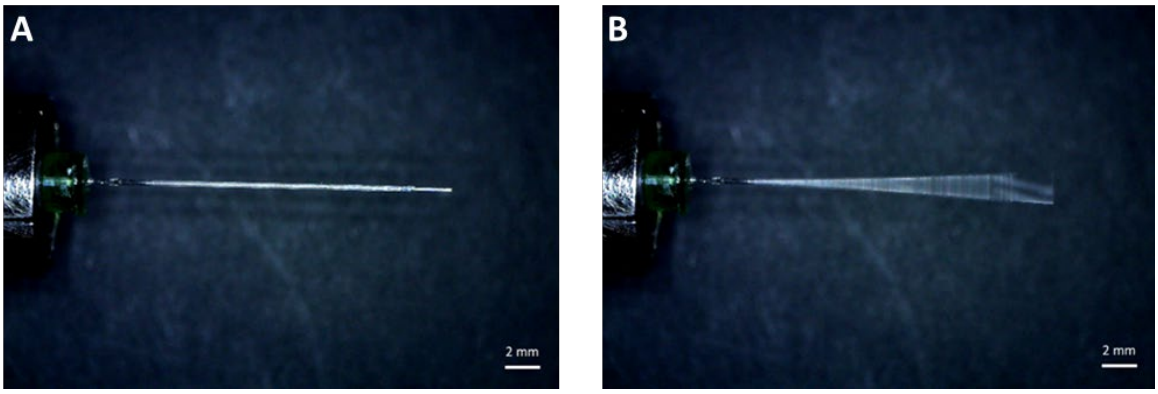

Figure 5.12 Fibre-optic cantilever at rest **(A)** and when performing the oscillations **(B)**.

5.2.3 Optical Micro-System of the Micro-Endoscope

Along with the fibre optic and the scanner, the optical micro-system is a key component of the endoscope. It focuses the laser beam onto the sample and collects the scattered signal. The optical micro-system contains a set of lenses, in which focal length, numerical aperture (NA), and optical aberrations define the magnification, FOV and resolution of the image. The diameter and length of the optical components add to the final dimensions of the probe head. The design of the micro-optics should be optimized to maximally reduce the size of the probe.

Furthermore, consideration should be given to the design of the fibre to allow fast laser delivery to the sample and nonlinear signal collection. The desired qualities of the fibre include but are not limited to non-destructive laser transmission and signal collection efficiency. The beam diameter is determined by the fibre dimensions and hence, can affect the NA and hence, resolution and therefore fibre dimensions should be given consideration [95]. The relation between a beam diameter and spatial resolution is described by the equation (26) [95]:

$$D_l = MD_{fc} \tag{26}$$

Where: D_l is the diameter of the laser focus, M is magnification, and D_{fc} is the diameter of the fibre core defined by its mode-field diameter (MFD).

A larger core size causes a less resolved image and lowers excitation intensity (power density) as the focal spot will be larger.

Hollow-core fibres (HCFs) have a larger core diameter and a lower NA compared to single-mode solid-core fibres. The latter are currently the ones that are mostly used in endoscopes for multiphoton imaging. Reduction of the (mode-field diameter) MFD of the HCF should lead to improvement of the resolution and magnification of the system, since, with a higher NA of fibre, the distance between the fibre tip and first optic in micro-objective lens would be decreased as well. The following section will describe and discuss the design and implementation of micro-objective with a high resolution.

Micro-Sphere for Higher Optical Properties of the Micro-Endoscope

A reliable method for the reduction of the MFD in the HCF is to fix a micro-sphere in the fibre tip face and several research groups have demonstrated it so far. Ghenuche *et al.* successfully demonstrated the usage of a 30 µm latex microsphere in the HC-PCF, and repeated it with a Kagome fibre using a 20 µm polystyrene sphere [96, 97]. For fibre scanning endoscopy, Lombardini firstly explored this method with a Kagome fibre [41] and Kudlinski with a DC-ARF [98]. Both authors applied CO_2 laser splicing to melt the edges of the microstructure of the fibre and set the sphere inside to strengthen the adhesion so that the micro-sphere would withstand high-frequency oscillations of the fibre scanner.

The material, diameter, and refractive index define the optical properties of the micro-sphere. For this project, a 30 µm dry soda lime glass micro-sphere (Thermo scientific) was used. The micro-spheres were dispersed on a microscope glass slide. For our experiments a microsphere was attached manually by translating it perpendicularly to a glass slide on which microspheres were dispersed. This was achieved with the help of a 3D micrometre translation stage under an optical microscope. During this procedure, it was important to not deform the fibre's capillaries. **Figure 5.13A** shows a photo of the lab setup for the insertion of microspheres into DC-ARF**.** An optical image of the side-view of the micro-bead inserted into the end-face of the DC-ARF is shown in **Figure 5.13B**. Once fixed into the fibre core, the micro-bead is tightly held by the electrostatic interactions and withstands high-frequency oscillations of the fibre scanner. Nevertheless, in order to make the micro-bead adhesion more stable and permanent, a UV curing optical adhesive (Norland, nr 61) was applied at the edges of the fibre tip. The proposed method is reproducible, easy to implement, and low-cost compared to the CO_2 laser splicing, which requires highly skilled training and availability of the high-cost equipment.

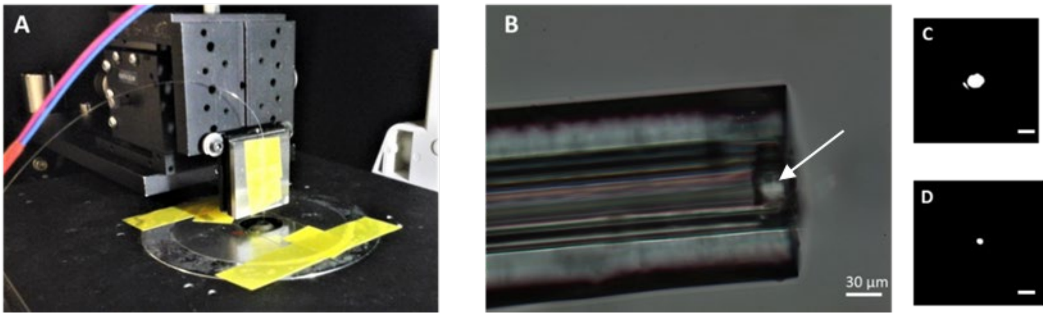

Figure 5.13 Micro-sphere insulation process in DC-ARF and its impact on laser beam diameter; **(A)** Setup used in the micro-sphere installation in the fibre face contains fibre facing down to make contact with micro-spheres placed on the microscope slide. The procedure is assisted with an optical microscope and 3D stage; **(B)** The side–view of the DC-ARF with the micro-bead inserted as shown by the white arrow; An image of the laser beam spot through the DC-ARF **(C)** without and **(D)** with a microsphere, bar scale = 17 µm.

The micro-sphere successfully reduced the MFD of the DC-ARF to a few micrometres as can be seen in **Fig. 5.13C-D**, which show images before and after attachment of a microsphere to a DC-ARF. This was explored further using a beam profiler camera. **Figure 5.14** shows the changes in the laser beam diameter after it propagates 0.36 mm from the DC-ARF without a micro-bead **(A-B)** and with micro-bead inserted into its core **(C-D)**. The beam diameter was significantly decreased by the use of the micro-bead **(Fig. 5.14C)** compared to the fibre without the bead **(Fig. 5.14A).** However, after travelling 0.36 mm **(Fig. 5.14D)** the beam was considerably larger than its bead-less counterpart **(Fig. 5.14B)** as a result of an increase in NA. The experimentally measured acceptance angle of the DC-ARF was 0.029, which was improved to 0.18 with a micro-sphere. Thus the use of a micro-bead improved the magnification and NA of the system.

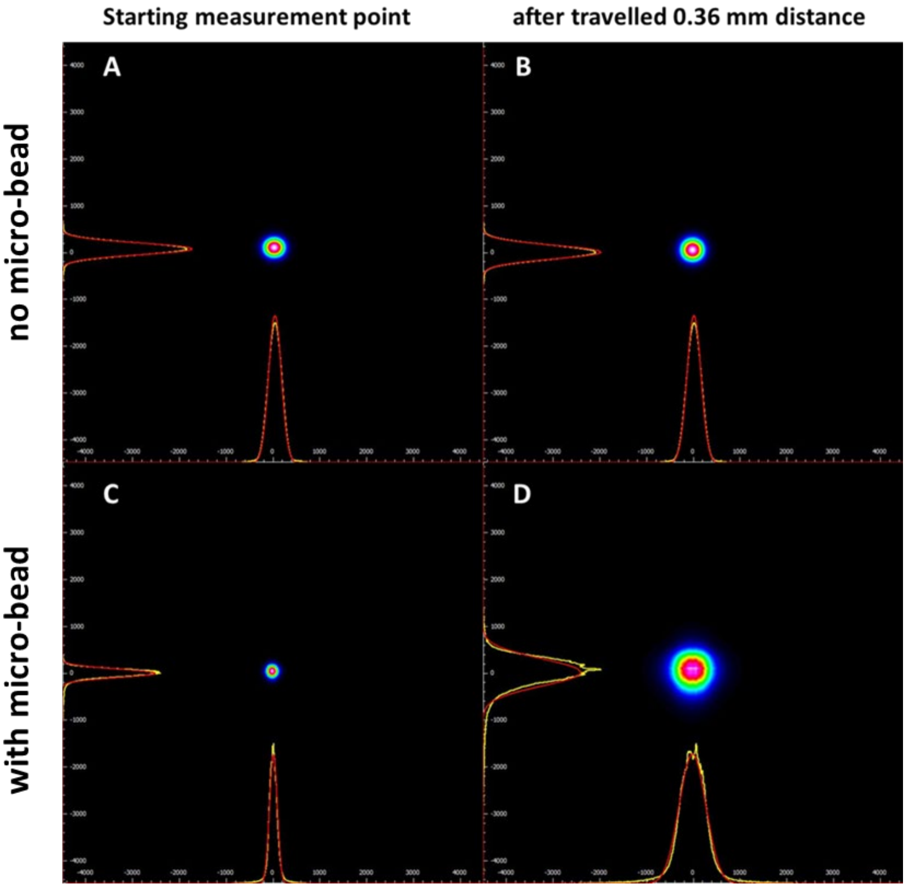

Figure 5.14 Improved focus of a laser beam spot with a micro-sphere. The size of the core diameter of the DC-ARF **(A)** and DC-ARF with an attached micro-sphere in the core **(C)** observed with a beam profiler camera. The beam profile was measured again after the beam propagated a distance of 0.36 mm. A significant increase in the spot diameter was observed for the fibre with the micro-sphere **(D)** while for that without the bead, negligible difference in the beam waist dimension was noticed **(A-B)**.

Micro-Lens Assembly

The selection of optical components for fabricating a micro-objective lens for the micro-endoscope was inspired by the research of Zhoa *et al.* on versatile two-photon endoscope [95]. The work presented tests of three types of micro-lenses with different configurations: a single GRIN lens, an aspheric lens with a GRIN lens, and three achromatic doublet lenses. The first two lens configurations would provide a better resolution due to higher NA. Furthermore, the GRIN lens is preferable in terms of dimensions and miniaturization of the microscopic probe head. However, both types of lens suffer from a severe chromatic dispersion effect. In their work the combination of achromatic doublets produced the best results with respect to the resolution and signal collection.

In this project, the configuration with two achromatic doublet lenses was used for the micro-endoscopic probe system. The chosen optics (Vis-NIR coating) were purchased from Edmund Optics. They had different focal lengths, namely: L_1= 3 mm (#84-127), L_2=4 mm (#84-128). The choice of the lens and the final configuration was assisted by simulations conducted in Optics

Software for Layout and Optimization (OSLO) [99] **(Fig. 5.15)**. The advantage of the smaller number of optical components is the higher optical power on the sample and simplicity.

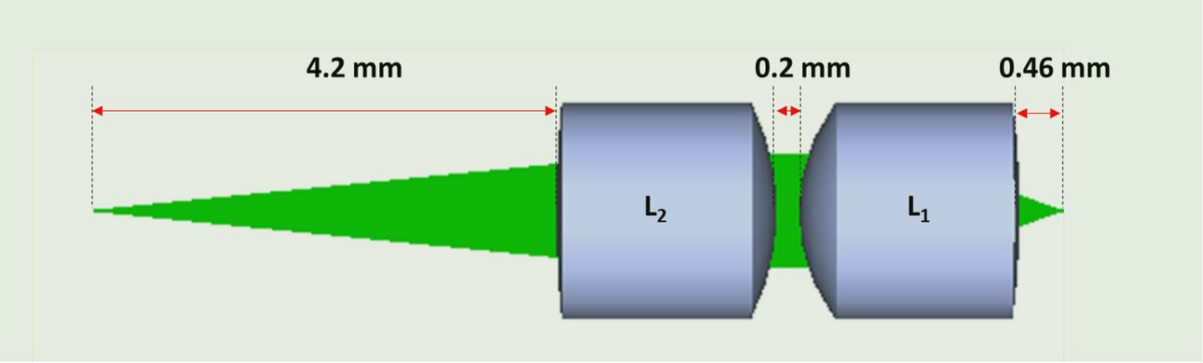

Figure 5.15 Micro-lens assembly objective designed for micro-endoscopic probe is composed of two achromatic doublets from Edmund Optics: L_1 - #84-127, L_2 - #84-128.

This configuration for the micro-objective assembly was characterised and the following parameters were measured and calculated :

NA from the fibre side = 0.18.

Distance from the fibre tip to the first lens surface = 4.2 mm.

NA from the sample side = 0.25.

Image FL = 0.46 mm.

Magnification M= 0.28.

FOV = 0.42 mm.

5.2.4 Imaging System

When the fibre tip scans the sample area in the expected pattern, the light interacts with the sample and the signal is collected back through the same fibre point-by-point. Control of the scanning process and signal measurement should happen instantaneously so that signal intensity is assigned to its right position on the scanning surface. However, in order to achieve miniaturization of the micro-probe head, the utilization of micro-parts is crucial and hence, for calibration there is no space to accommodate a typical (standard sized) motion sensor. This imposes the separation of the imaging process between the calibration of the fibre scan and that of the sample (signal intensity measurement across a sample). The most important part of imaging with such a probe is the synchronization of fibre scanner motion with the optical signal acquisition. However, the acquisition of position (image coordinates) requires that the fibre motion is calibrated beforehand. Hence, the system was designed to work in an open-loop two-step scheme. The architecture of the imaging process is presented in **Figure 5.16**.

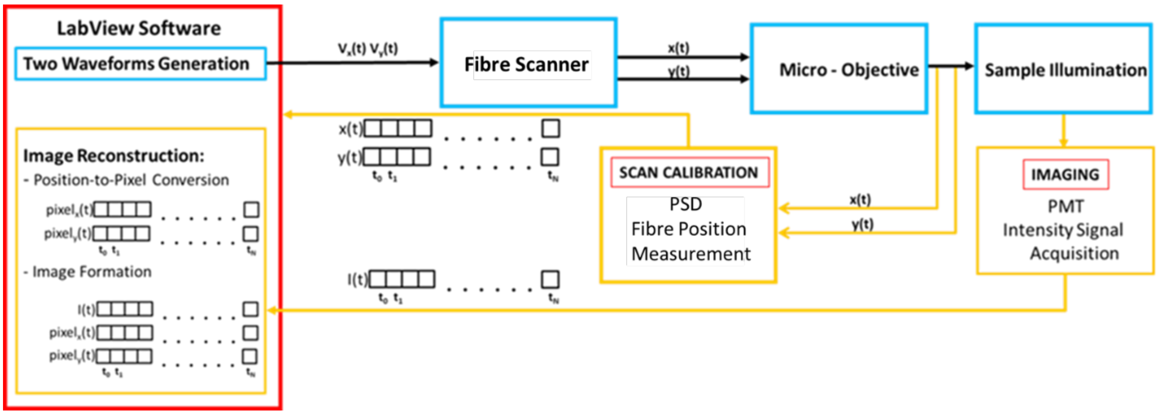
LabView Software
Two Waveforms Generation
Image Reconstruction:
- Position-to-Pixel Conversion
pixel$_x$(t)
pixel$_y$(t)
- Image Formation
I(t)
pixel$_x$(t)
pixel$_y$(t)
t$_0$ t$_1$
t$_N$
V$_x$(t) V$_y$(t)
Fibre Scanner
x(t)
y(t)
Micro - Objective
Sample Illumination
SCAN CALIBRATION
PSD
Fibre Position
Measurement
IMAGING
PMT
Intensity Signal
Acquisition

Figure 5.16 Schematic representation of the architecture of the imaging procedure that contains two steps: *scan calibration* that obtains $x(t)$, $y(t)$ position of the fibre scanner motion, and *imaging* – sample intensity signal acquisition. The image is reconstructed based on the fibre position and signal intensity data.

The first part of the system operation is named as *scan calibration* and its aim is the creation of a spiral pattern made from two waveforms using parameters such as amplitude, frequency, phase, duration, and sampling number. Two waveforms $V_x(t)$, $V_y(t)$ are generated using LabView [100] software drives the fibre scanner in the given scheme. The real-time fibre tip displacement is monitored and registered by a position sensitive detector (PSD) which measures fibre position $x(t)$, $y(t)$ based on beam spot motion. This builds a map of fibre positions during the scanning process. Two matrices are formed. At first matrix, fibre position data $x(t), y(t)$ are converted to discreet pixel coordinates $pixelx\ (t), pixely\ (t)$ (**Fig. 5.17**). These pixels form a square matrix, which size is defined by the user. A second matrix is created to register the number of samples for each pixel since sampling across the FOV is non-uniform. The positional data of the spiral pattern is stored in the software and used for image reconstruction until the scanner needs re-calibration (at the start of new experiment).

During the *imaging* step, fibre rotates according to the two driving waveforms $V_x(t)$, $V_y(t)$ made of parameters saved in the scan calibration part. The primary purpose of this second part of the image acquisition process is to collect the sample signal and assign it to scan positions. The PMT detector measures light intensity in epi-detection and provides the corresponding voltage signal to the software. The image reconstruction commences on sending the driving voltage to the fibre scanner. The signal intensity is matched to its position on the pixel matrix (**Fig. 5.17**). Finally, the intensity for each pixel is normalized by the sampling number corresponding to this pixel, and an image is produced.

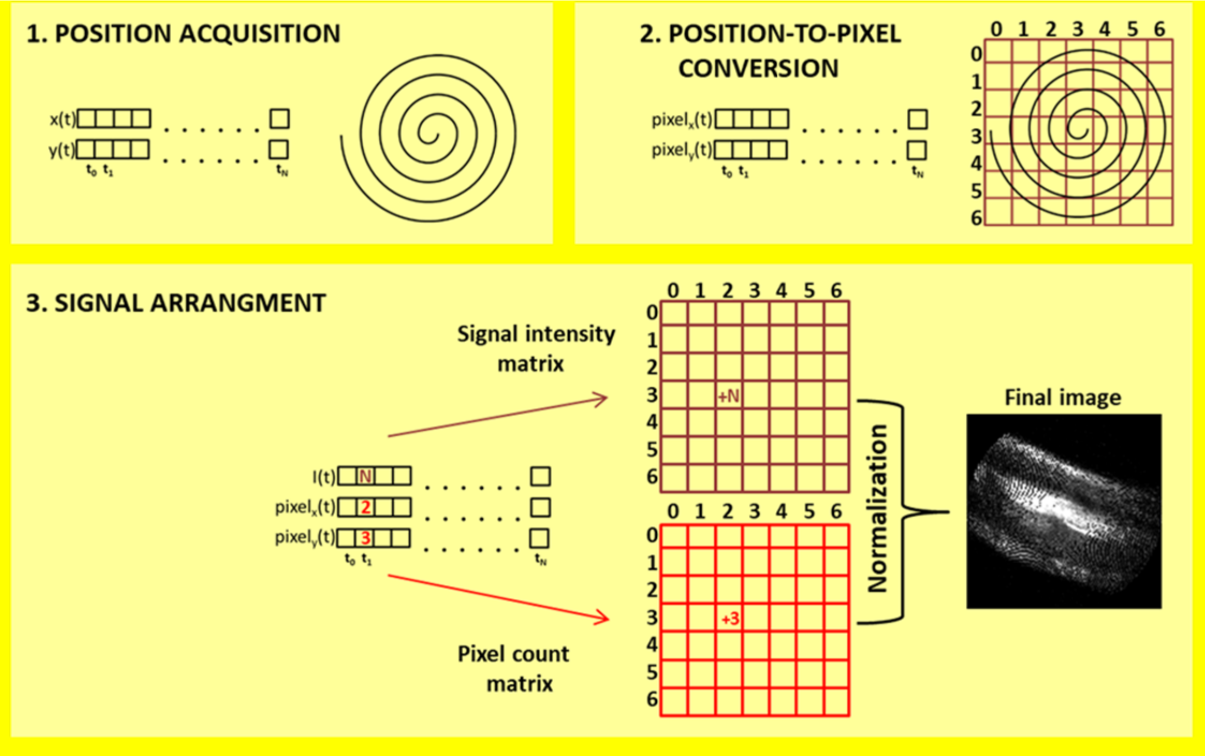
1. POSITION ACQUISITION
x(t)
y(t)
t0 t1
tN
2. POSITION-TO-PIXEL CONVERSION
pixelx(t)
pixely(t)
0 1 2 3 4 5 6
3. SIGNAL ARRANGMENT
Signal intensity matrix
I(t) N
pixelx(t) 2
pixely(t) 3
+N
+3
Pixel count matrix
Normalization
Final image

Figure 5.17 Image construction requires fibre position measurement **(1)**, which is converted to its pixel coordinates **(2)** creating a square matrix. The average light intensity is assigned to the spot position on the matrix specified at detection **(3)**. A second matrix is created to assign a number of counts for each pixel **(3)**. Finally, intensity matrix is normalized by the sampling number from second matrix, and an image is generated.

Hardware and Software for Data Acquisition

The National Instrument PCI-6110 multifunction I/O DAQ device was used to synchronize the process of data acquisition between the fibre position and signal intensity. It has 4 analogue inputs (AI), 2 analogue outputs (AO), and a maximum rate of 5 M/s/ch. The PCI card was connected to terminal block BNC-2110 to simplify the connection of the analogue signal. BNC block was sending generated V_x, V_y to the piezo amplifier (PI E-413.1) with two inverted channels and maximum output voltage of -250 to 250 V that controls piezo tube motion. Then BNC receives an input analogue response on fibre position from two-dimensional PSD (PDP90A, ThorLabs), which is controlled by a K-cube position aligner (KPA 101 ThorLabs), and signal intensity from PMT.

The software for this project was created as a result of the collaboration with Dr David Gray, a LabView software architect. Its main function is the synchronization of the fibre scanner motion driven by V_x, and V_y waveforms generated in the scan calibration step that gives the position measurement, with the signal acquisition obtained in the imaging step. Afterward, the software performs an image reconstruction process. These output/input tasks are started at a designed time activated by an analogue trigger and delivered by the BNC terminal block.

5.3 Multiphoton Micro-Endoscopic Imaging

5.3.1 The Experimental System

Schematic representation of the setup built for multiphoton micro-endoscopy is presented in **Figure 5.18**. Fs pulse of 810 nm was generated by a tuneable Ti: Sapphire oscillator (116 fs, 80 MHz Spectra-Physics, Mai Tai), and coupled into DC-ARF. Fibre delivers excitation laser beam to the distal end of the probe where the micro-sphere focuses the light, which is re-imaged on the sample plane (for imaging step) or objective (for the scan calibration step) by lens assembly. Simultaneously, two voltage signals V_x, V_y generated in LabView software are sent via block terminal BNC 2110 to the piezo amplifier (Physics Instrument) to increase signal strength by 25 times, and drive the PZT in a spiral pattern. The shape of the generated waveforms is also available to the user via an oscilloscope (Tektronix, TDS 2004B).

During the scan calibration, the focal spot of laser is re-focused on the objective plane (Olympus 10x, 0.25 NA). The collimated beam is either focussed and imaged on a camera (Thorlabs, DCC1545M) or a position sensitive detector (PSD) (ThorLabs, PDP90A) powered by K-Cube Position Aligner (ThorLabs, KPA 101) and connected to BNC. A flip-mirror located behind the objective allowed bringing the scanning laser beam to the camera or the PSD as required at the calibration stage.

In the imaging part of the system operation, the laser beam is re-focused on the sample plane. The system is designed to operate in the backward collection (epi-detection) configuration. The scattered sample signal is collected back by the focusing optics, and then coupled into the DC-ARF cladding surface. At the proximal fibre end, the signal below 458 nm is reflected by a dichroic mirror (Semrock, FF458-Di02; 458 nm long pass) and further filtered by 2 filters at 405 ± 5 nm (Thorlabs, FBH405-10) and 400 ± 10 (Thorlabs, FB400-10). A photomultiplier tube (PMT) (Hamamatsu, H10722-01) aids the detection of the SHG signal.

The point spread function (PSF) data for the determination of system resolution is collected in the forward detection. In this configuration, the reflected signal is gathered by the objects placed on the other side of the sample and focused by the lens on the PMT detector sensor.

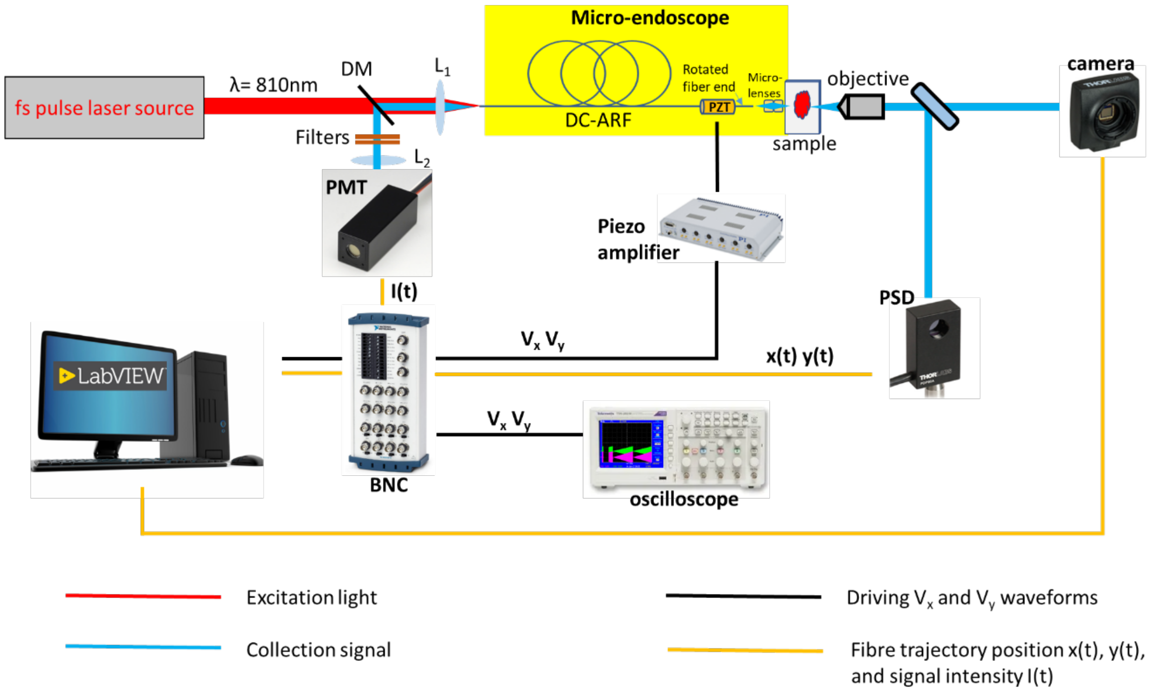
Micro-endoscope
fs pulse laser source
λ= 810nm
DM
L1
Filters
L2
PMT
DC-ARF
Rotated fiber end
PZT
Micro-lenses
objective
sample
camera
Piezo amplifier
I(t)
PSD
LabVIEW
Vx Vy
x(t) y(t)
BNC
Vx Vy
oscilloscope
Excitation light
Collection signal
Driving Vx and Vy waveforms
Fibre trajectory position x(t), y(t), and signal intensity I(t)

Figure 5.18 Schematic representation of the setup for micro-endoscopy. There are four distinct paths that are highlighted; *optical paths for*: light excitation (red), signal collection (blue); and *electrical connections for* : V_x, and V_y waveform generation (black), fibre position measurement $x(t)$, $y(t)$, and signal intensity $I(t)$ (yellow). PMT - Photon multiplier tube, PSD – Position sensitive detector, BNC – Terminal block, PZT – Piezo tube, L -lens.

Key parameters of the setup are summarized in ***Table 5***.

Specification	Value
Free standing fibre arm	12 mm
f_R	816 Hz
Peak-to peak drive voltage	100 V
FoV	420 µm
WD	0.46 mm
NA on fibre side	0.18
NA on the sample side	0.25
Magnification	0.28
Frame rates	0.33 µs
Pixel resolution	300 x 300
Lateral resolution	6.75 µm
Axial resolution	13.7 µm
Power at the sample	40 mW
Fibre length	1.5 m

Table 5. Summary of the final specifications of multiphoton micro-endoscopic setup built in this project. Data presents optical parameters and some of the endoscope dimensions.

5.3.2 Second Harmonic Generation Imaging with Micro-Endoscope

The micro-endoscopic system was tested in descanned epi-detection configuration using the second harmonic generation (SHG) technique. Samples of rat tail tendon and barium titanate crystals similar to those used in earlier chapters of this thesis were used here for evaluating the performance of the micro-endoscopic system. Images were successfully obtained and as expected strong SHG signals were observed from both samples (**Fig. 5.19**). The average power on the sample was 40 mW. The excitation wavelength was 810 nm and 405 nm for signal collection, respectively. The signal-to-noise ratio was determined and data is presented in the next section. As seen from **Figure 5.19**, the images contain structural details and as expected some fibrous structure is visible for collagen. As it was expected, the images present poorer quality compare to those taken with the benchtop system (**Fig. 3.9 a, b, 4.14 b**). The black dots present on the images are NaN (Not a Number) values, which indicates no signal detected due to the uneven spacing of sampling points in a spiral scan [101]. A more analysis on NaN-s is presented later.

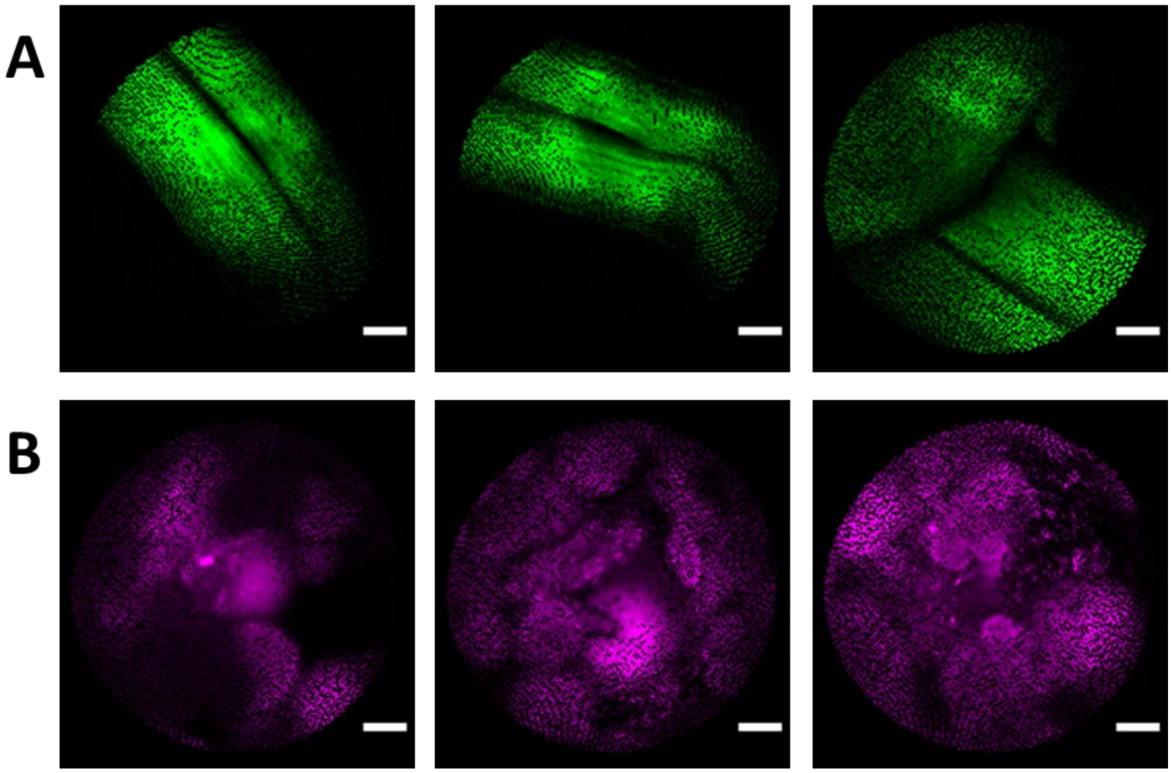

Figure 5.19 SHG images of a mouse tail tendon (**row A**), and barium titanate crystals (**row B**) taken with the multiphoton micro-endoscopic system using SHG technique. Image parameters: pixels 300x300, 0.33 fps, ~ 40 mW on the sample, magnification 0.28. Scale bar = 60 µm.

5.3.3 Signal-to-Noise Ratio (SNR)

Figures 5.20 and **5.21** present 1, 5, and 15 average images (a-i) of barium titanate crystals (**Fig. 5.20**) and mouse tail tendon (**Fig. 5.21**). The aim of this evaluation was to establish the optimal signal level at the minimum number of frames. Furthermore, the evolution of the signal-to-noise ratio (SNR) was measured for different numbers of averaged images.

Three images of mouse tendon samples which had blank and sample areas were selected to perform the SNR assessment. SNR was evaluated across a line profile that spanned these blank and sample areas. The method is described in detail in Chapter 3.2.6.

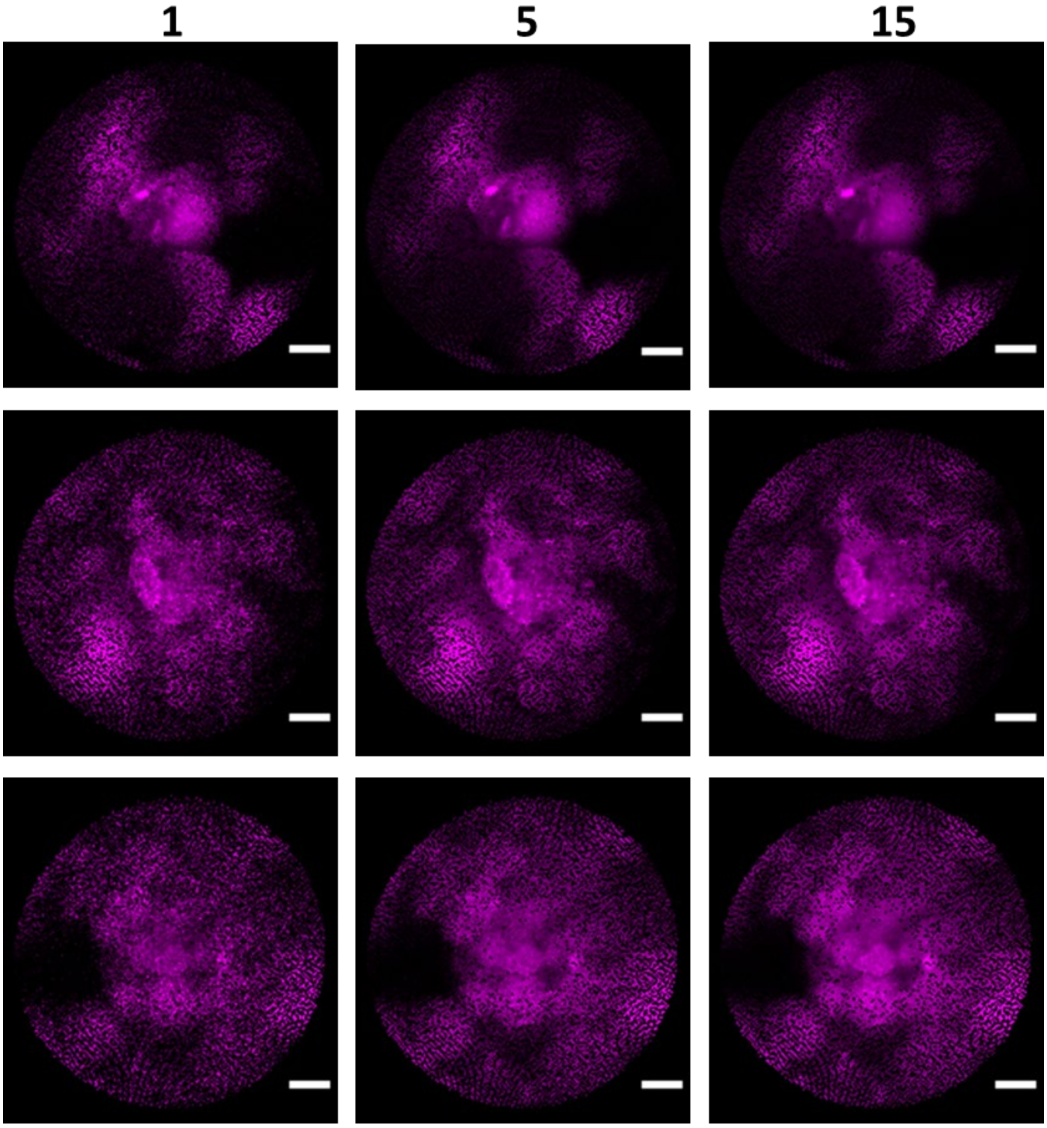

Figure 5.20 Images of barium titanate crystals with 1, 5, and 15 averages obtained from different areas of the same sample. Images show improvement in signal level as the number of frames increases. Scale bar = 60 µm.

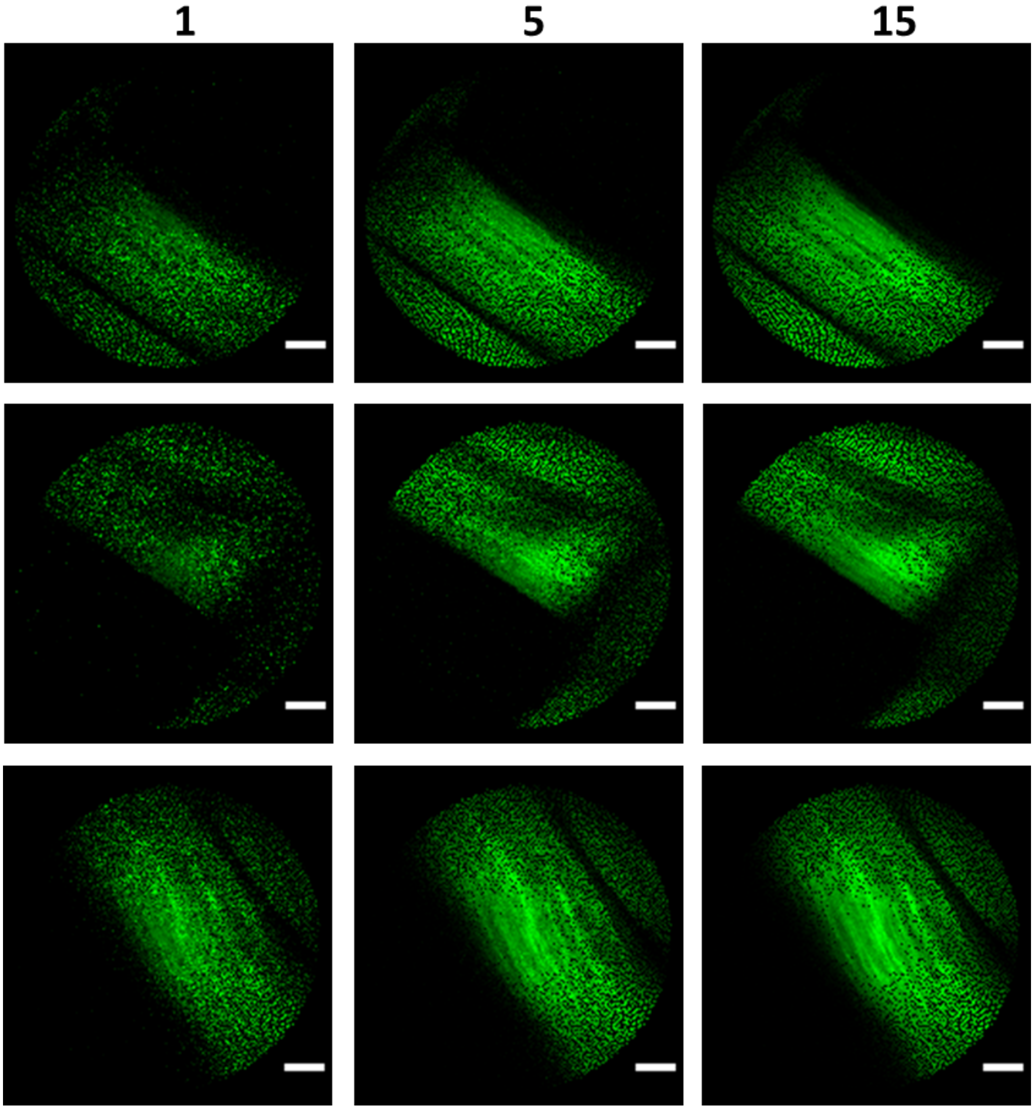

Figure 5.21 Images of mouse tail tendon obtained with 1, 5, and 15 averages from different areas of the same sample. Images show improvement in signal level as the number of frames increases. Scale bar = 60 µm.

The evaluation of grey value plots for images taken from three different areas indicates that the increase levels are typically highest in the middle part of the imaging. It also showed that increases between 1 and 5 frames (**Fig. 5.22**, graphs **A**, blue and red curves) but the improvement is not much on taking 15 averaged images (**Fig. 5.22**, graphs **A**, red and black curves). Graphs **B** of **Figure 5.22** presents the SNR values against distance along the line profile. SNR plot (blue curve) for 1 image is on a similar level as for two other images. However, the curve has more spikes than compared to curves with higher (5 and 15) number of frames (**Fig. 5.22B** curves red and black, and **Fig. 5.20**, and **5.21**). To summarize, an image with 5 averaged frames was found sufficient and increasing number of frames did not significantly improve SNR although it will extend the image acquisition time.

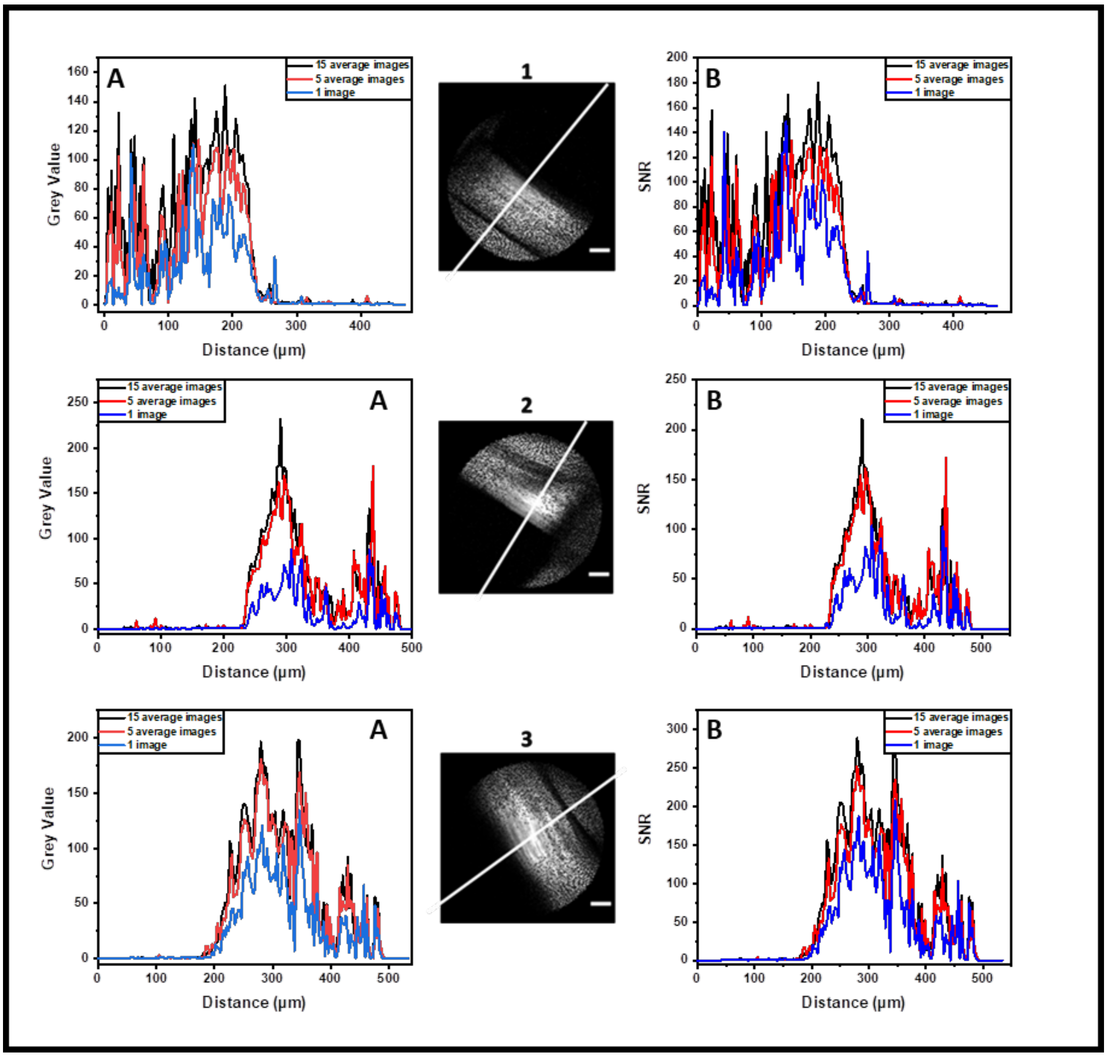

Figure 5.22 Graphs in panel **A** present grey value vs distance for the images taken along the white line profiles (images 1, 2, 3). Graphs in panel **B** show SNR as a function of distance for the images 1, 2, 3 obtained along with the white line profile.

5.3.4 Resolution

Resolution measurements were performed using polymer microspheres (4502A, Duke Standards). The system was tested with a variety of sizes of polymer beads (PB) in the forward detection. Resolvable images were obtained using 5 µm beads. The resolution of the system was evaluated by its point spread function (PSF), which is related to the response of the imaging system to a point source. The model PSF is expressed by its 3-dimensional diffraction pattern of light emitted from an infinitely small point source of the object. The formulas for theoretical PSF for *x, y,* and *z* directions are [41, 102]:

$$r_{x,y} = \frac{0.46\lambda}{NA} \quad (27) \qquad\qquad r_z = \frac{1.4n\lambda}{NA^2} \quad (28)$$

The above equations indicate that the system resolution depends on *NA* and *λ*. The calculated theoretical resolution for the endomicroscopic system built in this project is $r_{x,y}$ = 1.5 µm, and r_z = 18.1 µm. The practically obtained PSF was measured obtained by imaging 5 µm polystyrene beads using 810 nm excitation wavelengths. The intensity profile of 5 different beads was averaged in the Fiji [88] software and its full width at half maximum (FWHM) gave the value of the lateral (*x,y*) = 6.75 µm. To calculate the axial resolution, the orthogonal view of *z* stack of 10 images was obtained, then from its *xz* view FWHM was measured for given bead. Presented method established axial resolution (*z*) = 13.7 µm. **Figure 5.23** presents the image of the 5 µm polymer beads (**A**), the average signal intensity distribution of 5 beads plotted in the radial (**B**) and axial (**C**) direction and the orthogonal view of *xz* PB stack (**D**).

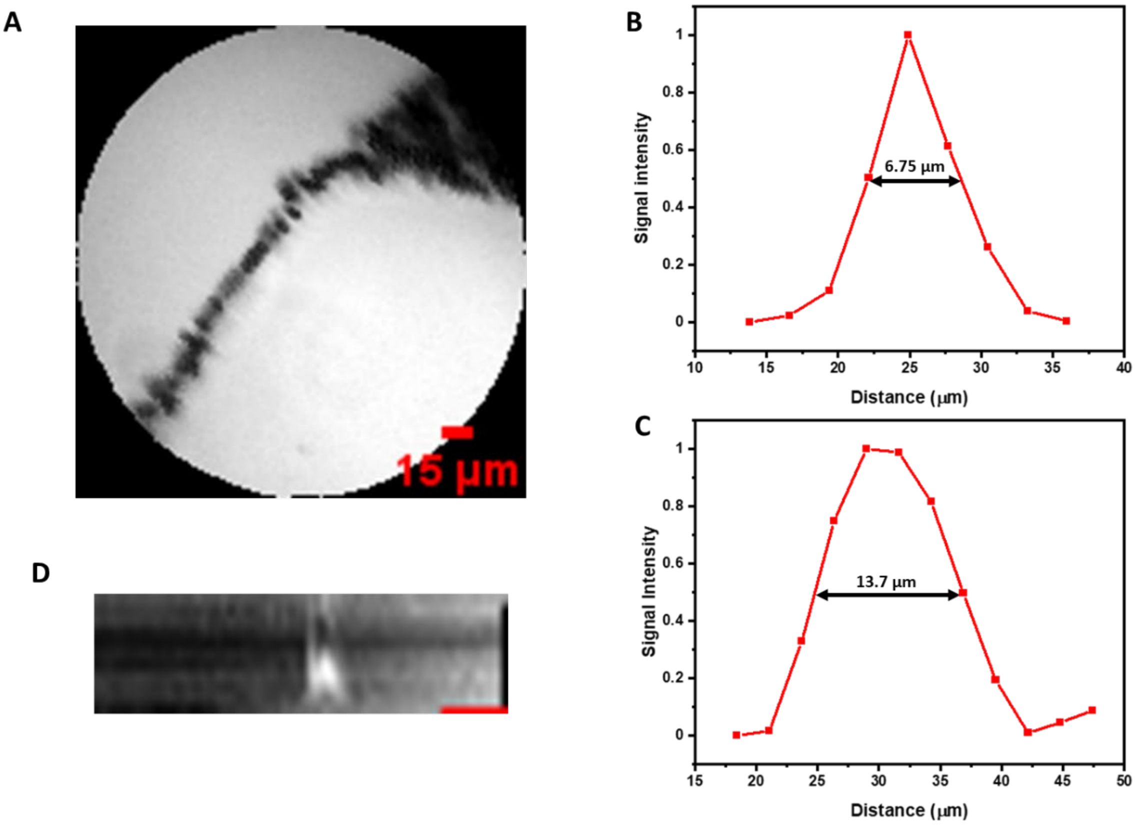

Figure 5.23 PSF measurements: **(A)** Image of 5 µm polystyrene beads obtained with the system for multiphoton micro-endoscopy in the forward detection scheme; **(B, C)** signal intensity peaks shows the FWHM at 6.75 µm and 13.7 µm in the lateral and axial direction, respectively; **(D)** Intensity map of the 3D PSF along the *xz* plane.

The deviation between the theoretical and measured values of the PSF may originate from the spherical aberration of the lenses and the imperfection of the fibre modality. Although system achieved high resolution, comparable setups obtained submicron image resolution of $(x,y) = 0.83$ and $(z) = 5.9$ [81]. Furthermore, the micro-sphere did not achieve a tight focal spot as was expected. Similar issues have been reported in the literature for fibre micro-endoscopes [41, 95]. This led to the lower NA and larger beam waist after focusing the laser through the silica bead located at the fibre end.

5.3.5 Not a Number (NaN) Values

The resonant spiral scanning has a non-uniform character. This means that the scanning speed is the lowest at the centre and increases moving towards the edge of the spiral. However, the software applies a constant sampling rate, which leads to a much higher sampling density around the centre of the spiral (**Fig. 5.4B**). Consequently, the middle of the image will be over-sampled and it's the edges will be under-sampled with gaps where no signal will be detected. The missing values in the data are called Not a Numbers (NaNs) and they reduce image quality. A square wave in the scanning pattern formation can be used to remove NaN values (**Fig. 5.24**). This allows better control of sampling points in terms of their number and scanning positions. The square waveform was not implemented in this project, instead the following methods were applied to reduce the effect of NaNs and to improve the final image quality.

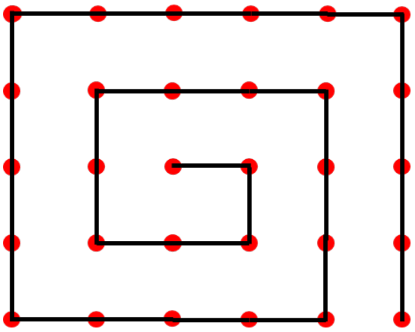

Figure 5.24 Uniform sampling points distribution.

Spatial Sampling Points Distribution

The number of NaNs recorded in an image depends on the pixel number, frequency of the waves, and scan duration. Since the frequency is fixed and is related to the properties of the resonator, more equal spatial sampling points distribution across the scanning pattern can be achieved by the manipulation of a number of pixels and frame time. **Figure 5.25** presents changes in the organization of the sampling points during the scan calibration step recorded every 10 µs. The centre of the images is entirely covered with the sampling points but more NaNs appear closer to the image edges. Although, the number of the sampling points is the same for each image (**Fig. 5.25**) still sampling points on images (**d, f**) occupy the greater part of the spiral plane than on images (**g, i**). Ultimately, spirals with organization of point like that presented in the image **d** were selected for overcoming the effect of NaNs.

Higher number of the pixels improves spatial resolution but creates more NaNs. Therefore, the number of pixels has to be balanced to reduce occurrence of NaNs. Here, the 300x300 pixels were selected as the most suitable in the reduction of the number of NaN values. Raising the number of pixels to 500x500 led to an increase of NaNs to a degree that they outnumbered points containing the image value data.

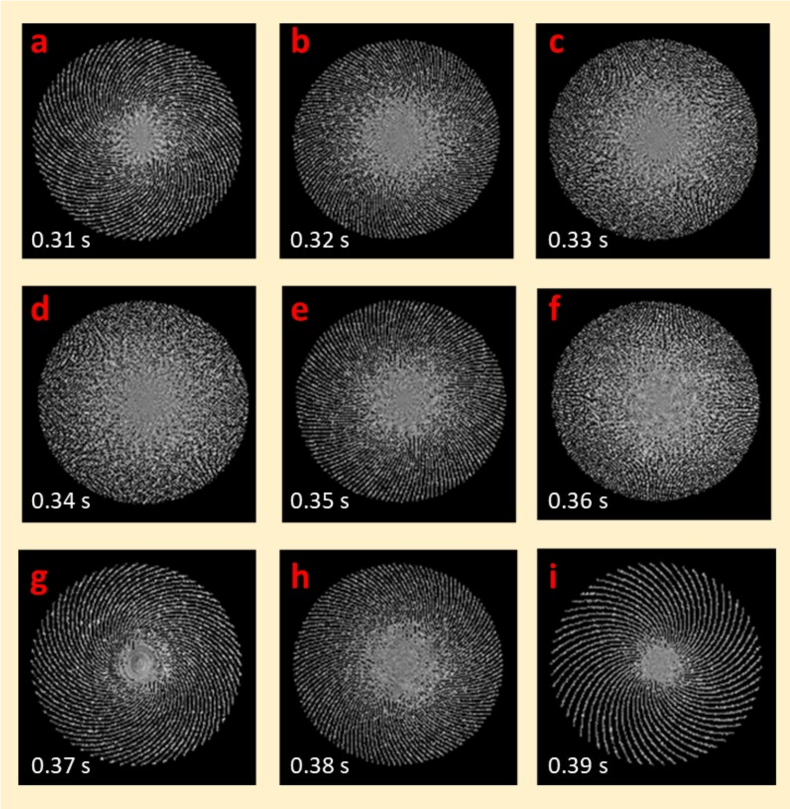

Figure 5.25 Changes in sampling point’s distribution for different spiral time durations. For more uniform distribution of sampled points across an image plane, hence, a reduction NaN numbers, the *d*, *f* images were selected as a template for image reconstruction.

Hybrid- Interpolation

An additional aid in removing NaN values was to apply a post-processing image step. The method employed in this work was a linear interpolation based on the linear polynomials to construct new data points within the range of a discrete set of known data points [103].

The linear interpolation processes every single point on the image matrix and can alter the original information of all the points. To sustain raw data with no modifications, hybrid interpolation was tested. Its operation is based on mixing raw data with NaN values that were corrected in interpolation. In the hybrid interpolation process, all raw data undergo linear interpolation, then the NaN values in the raw data matrix, are filled with the values from the linear interpolation. Only the points where NaN values occurred were interpolated; hence the image experiences lesser post-processing modification. Row **A** of **Figure 5.26** graphically illustrates hybrid interpolation with examples demonstrated in row **B**. The product of interpolation and hybrid interpolation gives very similar outcomes (**Fig. 5.26** images **5** and **6**) due to the high number of NaNs. Still, after the hybrid interpolation process, the image is sharper and cleaner (**Fig. 5.26** image **6**).

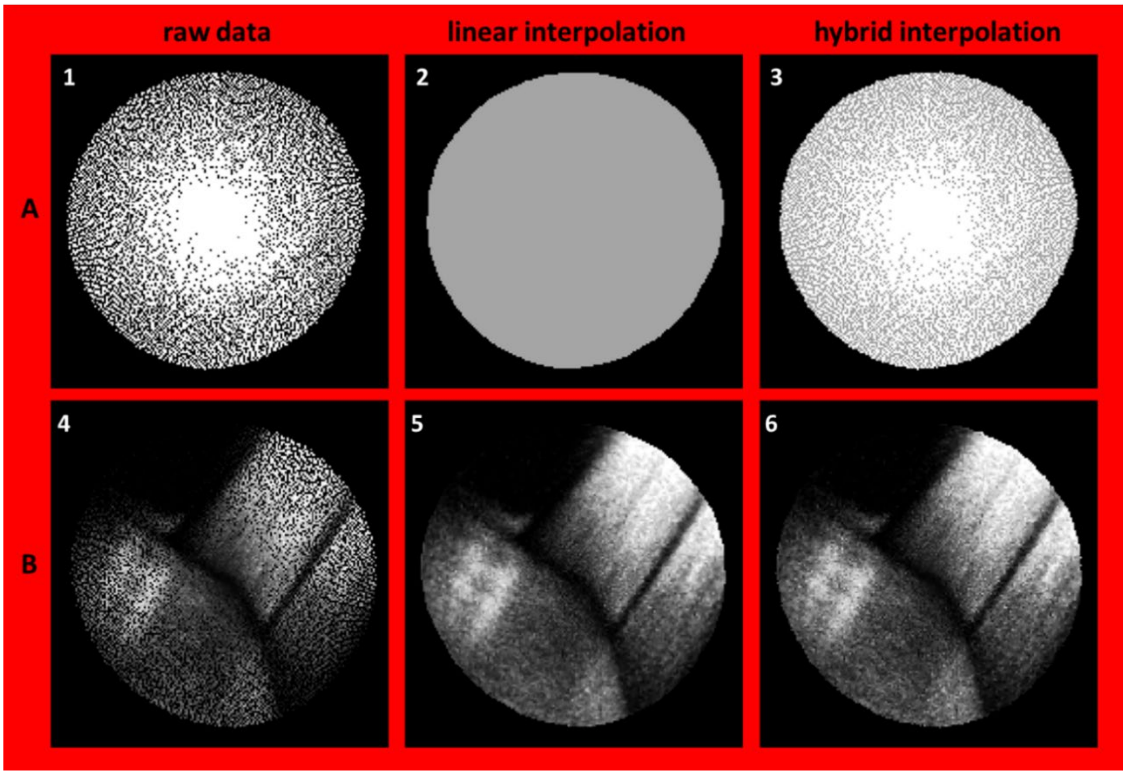

Figure 5.26 Post-process hybrid interpolation: raw data undergo linear interpolation, which estimates the missing NaN values that are then used in the hybrid interpolation process to refill absent information on the original image matrix (**row A**). Example of the hybrid interpolation applied on images taken with the micro-endoscopic system (**row B**). Image 4 shows raw data with black dots representing missing values; in image 5, raw data from image 4 underwent linear interpolation; image 6, hybrid interpolation assigned only NaNs obtained in linear interpolation to the black spots in image 4.

5.3.6 Optical Aberrations

A spherical lens surface refracts the rays at a different angles causing them to coincide at the different focal spots [104]. Here, there is an off-axis aberration related to different angles of the fibre created during the scanning operation. When fibre performs the spiral scan across the sample, its angle with the optical axis will change depending on the part of the spiral executed by the fibre so that a uniform focal spot will be created only when fibre is aligned with the optical axis. As the fibre goes towards the edges the angle between it and the lens increases causing a stretching of the focal spot. This has an impact on the image quality that shows blurriness at its edges and reduces the FOV (**Fig. 5.27**).

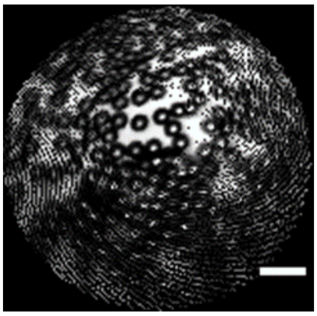

Figure 5.27 Transmission image of the 20 μm PB obtained in the forward detection presents off-axis spherical aberrations and the beads become blurry at the edges of the image. Bar scale = 60 μm.

5.4 Perspective and Future Work

This chapter demonstrated the realization and proof-of-concept application of a micro-endoscope system built for multiphoton microscopy. SHG images could be obtained for mouse tail (biological) and barium titanate crystal samples. Two-photon fluorescence signals of mouse lungs and bones, which were captured with the HHM, were not sufficiently strong to be detected by means of the endoscopic probe. This indicates that probe sensitivity has to be increased in order to expand the utilization of the micro-endoscope to other multiphoton modalities. Hence, more consideration needs to be put into the optical system design and reduction of the optical aberrations. Some points are presented below that should improve the probe performance.

Setup alignment

The biggest challenge of building a micro-endoscopic setup lay in the micro-components alignment. Due to their small size, the commercial and well-defined holders for optical components cannot be applied. This forced to construct a custom-made mounts for the setup made with millimetres rather than micrometres precision.

Within probe head components, to mount a fibre in the piezo tube, special adaptors were printed out and the hole for fibre mounting was drilled in them. However, the gap between fibre outer diameter

(~280 µm) and drilled hole (~400 µm) was about 120 µm and had to be filled with a glue, that was randomly distributed around the fibre. This caused fibre deviation from the main axis of the probe. Since the deviation angle (**Fig. 5.28A**) between main axis and fibre increased with the distance from the point of fibre fixation in the adaptor, by the time laser beam reached the lens assembly, the angle significantly increased and caused light entering the lens surface far off from the centre of the lens. This required to put a lot of efforts in improving precision of fibre mounting in the PZT. One of the methods was to keep the fibre in vertical position during the glue fasting, so the glue would not move more to one side due to gravitation force.

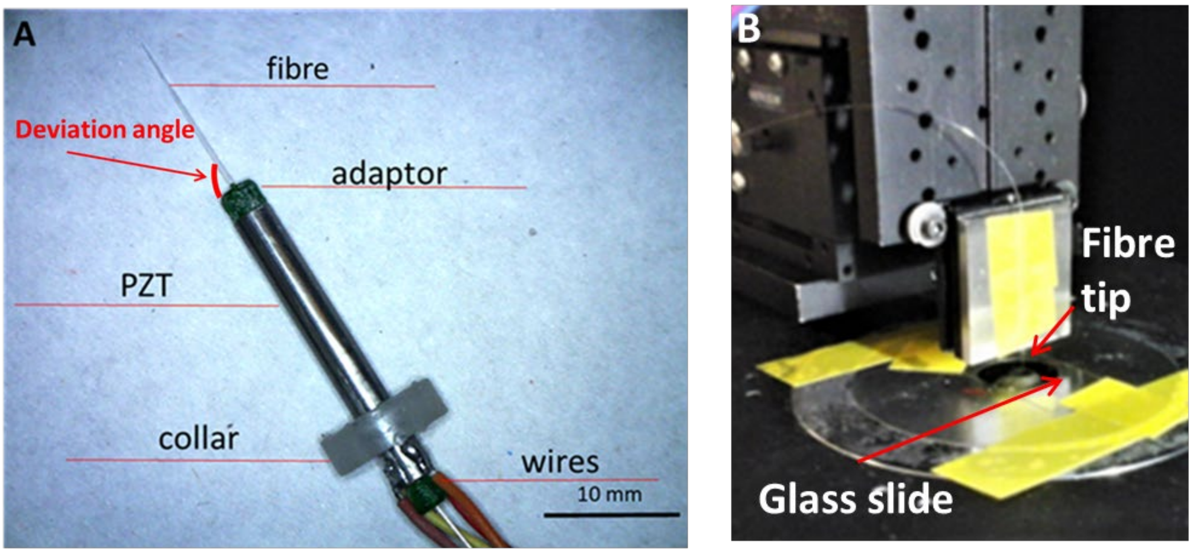

Figure 5.28 The examples of misalignment of optomechanical components **(A)** generation of deviation angle between fibre and adaptor that will increase with the distance and caused the laser beam enter the lenses assembly far off from the centre of the lens surface; **(B)** Micro-sphere insulation process in DC-ARF shows fibre tip that must be perpendicular to glass slide position to improve micro-sphere alignment with the axis of the fibre's core.

Another example of misalignment source is micro-sphere installation in DC-ARF core (**Fig. 5.28B**). The fibre tip must be placed in the metal block groove so that it will make an orthogonal angle with the surface of the glass slide. To control the quality on micro-sphere installation in DC-ARF, the samples of fibre tip with micro-sphere were examined under light microscope first, and then the laser was coupled to the fibre sample for the beam spot inspection with the camera. If the results of above examination was satisfying, the fixation of micro-bead in fibre tip was strengthen with a UV curing optical adhesive that was applied at the edges of the fibre tip. The orthogonal angle between fibre and glass slide, and pre- glue fibre tip control steps had to ensure higher alignment of micro-bead with fibre central axis.

Scanning Pattern Irregularity

The enhancement of the repeatability of the scan pattern can be achieved by adding a non-imaging part to the scan pattern. This will improve the regularity of the scanning pattern. On the other hand, the absence of the active braking and decay steps increase the imaging frame rate. Furthermore, one needs to consider the impact of the fibre deformity on the spiral scan uniformity and regularity. DC-ARF carries an extra weight that is fixed to its tip in form of a micro-sphere. If fibre is situated horizontally to the optical table, the fibre tip may slightly deviate towards the ground due to gravity. Unless the probe is in use, it is advisable to keep it in the vertical plane. At this stage of the project, it was not practiced.

Optical Aberration

The optical aberration presented in this work has its origin from the spherical shape of the optical components and changing operational fibre angle with the optical axis of the system. Miniaturized dimensions and short working distance put constrains on the optics for micro-endoscopy. This imposes degradation of the image due to the spherical aberration that is inevitable for this size and applications of the instrumentation. Reduction of its impact can be achieved by applying a shorter length of the fibre arm as the fibre will not lean out excessively of the optical axis. However, this will decrease the field of view (image size).

Image Frame Time

The image frame time can be further improved by using the higher resonance frequency f_{RES} that is related to the length of the free-standing fibre part. **Figure 5.3A** demonstrates the huge increase in the f_{RES} as a function of the fibre arm between 10 mm and 5 mm. By shortening the fibre arm length, the image frame rate can be better optimized.

Probe Assembly

All experiments in this section were conducted using an unassembled probe. Although the probe integration is not covered in this work, here are some considerations that need to be taken before embarking on the process. The first part of the assembly process requires the selection of the materials for the micro-components encapsulation. The preferred materials should be bio-neutral, lightweight, and non–conductive. The integration of the probe is a hand-operated process, therefore, it requires high precision and experience in manual skilled engineering work. The significance of the symmetrical micro-parts assembly and its impact on the correct and efficient spiral scan formation was described and highlighted in the section describing probe design (5.2.1).

5.5 Conclusions

The current section described the design and construction process of the probe for nonlinear endoscopy. The core of the probe contains the fibre, a scanner, and an optical lens system. In order to achieve system miniaturization, a tubular piezo actuator was implemented and the appropriate scan correction was performed. This gave the ability to the fibre-scanning imaging device to execute a spiral scan across the sample plane.

The optical lens system components were selected based on the desired miniature probe size and fibre features. For this project, the setup for micro-sphere installation in fibre core tip was assembled and a reliable technique was developed. At the end of the process, the optical system parameters were characterized to learn more about the probe's ability to perform nonlinear, label-free endoscopy.

A great deal of time was dedicated to the development of the program in the Labview software for synchronized controlling scan calibration and imaging operations. This chapter presented the results of collaboration with Dr David Gray on the programming code that successfully controlled the hardware of the setup and final image reconstruction. The software allowed post-processing correction of the images in real-time.

Firstly, imaging tests of the fibre-scanning device for endoscopy showed images of mouse tail and barium titanate crystal obtained with SHG. The average power on the sample was 40 mW. The image resolution and SNR indicated a promising probe performance this early developmental stage for this micro-endoscope. Additionally, as a consequence of the generation of ramp sine waves, the sampling point distribution on the image matrix lacked uniformity causing the appearance of black dots that represented missing image values (NaNs) and decreased final image quality . Methods to overcome this issue by optimization of image pixel number distribution, duration time of the spiral scan, and post-processing hybrid interpolation were tested and discussed. Hybrid interpolation was found to be the most appropriate post-processing method to reconstruct images. While further improvements in terms of frame time or irregularity of the scanning pattern are required the development showed the potential of DC-ARF based micro-endoscopic system.

Chapter 6 Conclusions and Perspective

The aim of this thesis was to propose a more optimal solution for high power ultra-short laser pulse delivery and signal collection applied in nonlinear endoscopy. Hollow-core, double-clad anti-resonant fibre (DC-ARF) was proposed as a potent candidate for transmission of excitation laser in the core and back collection of the emission signal in the glass cladding. It allowed for the propagation of ultra-short pulses with minimum distortions generated by dispersion and nonlinear effects. Furthermore, the low refractive coating used in its fabrication created a contrast difference in the refractive index between the jacket and cladding needed for the glass inner cladding area to gain the guiding capability. DC-ARF is characterized by loss < 0.2 dBm^{-1} sustained over the 500 nm transmission window between 800 nm – 1300 nm that allows for accommodation excitation wavelengths for multiphoton microscopy. Additionally, the signal could be collected by the cladding that guides across all visible wavelengths.

DC-ARF was compared with two other waveguides: solid core fibre (SCF) and single-clad anti-resonant fibre (SC-ARF) that can guide only in the core. They were tested for delivering ultra-short pulse and backward signal transmission. The guiding condition created by hollow-core of ARF that is like free-space propagation allowed the two ARFs to guide the laser almost unaltered with negligible dispersion and nonlinear effects. Furthermore, only DC-ARF due to its high NA and large combined surface area of core and cladding was capable of back-coupling and transmitting sufficient signal to generate SHG images.

Next, DC-ARF was incorporated into a custom-made hand-held microscope (HHM); its design was the first step of this project in testing DC-ARF with a miniaturized and portable imaging device. The performance of HHM was evaluated based on the power delivery to the sample and signal collection in three configurations: free-space non-descanned detection (NDD), free-space descanned detection (DD), and descanned detection (DD) via DC-ARF by using SHG and TPF techniques. The imaging results showed a radical drop in the signal level between free-space descanned detection (DD), and descanned detection (DD) via DC-ARF. Computer modelling and optimization of selected optical components could help increase signal coupling efficiency. Experiments with the HHM informed on the performance of DC-ARF.

Finally, in the last stage of this PhD work, a micro-probe head for multiphoton endoscopy was constructed with three main components: DC-ARF, piezo tube (PZT) actuator, and micro-lens assembly. The work on the hardware of the system went simultaneously with writing the software for controlling and synchronization of the main setup operations. LabView program generated waveforms for calibrating the scanning spiral produced by the PZT actuator and reconstructed images. SHG images were characterized by a large FOV (0.42 mm) and high resolution (lateral =

6.75 µm, axial = 13.7 µm). Moreover, the work investigated the occurrence of NaNs in images and practical solution to decrease their impact to improve image quality either by altering imaging parameters or in post-processing. Finally, potential refinements of the performance of the designed micro-endoscope were discussed. Image frame time can be increased by using shorter free-standing fibre part or by improving upon the scan pattern irregularity, which can be achieved by introducing an active braking and free decay part into the driving PZT signal.

List of References

[1] Cancer Research UK, [online], Available: http://www.cancerresearchuk.org/about-cancer, [Accessed 22 June 2018].

[2] Boppart S A, Brown J Q, Farah CS, Kho E, Marcu L, Saunders Ch M, Sterenborg H J C M, “Label – free optical imaging technologies for rapid translation and use during intraoperative surgical and tumor margin assessment”, Biomedical Optics., 23(2): 021104 (2017).

[3] Stummer W, Pichlmeier U, Meinel T, Wiestler OD, Zanella F, Reulen H-J, “Fluorescence-guided surgery with 5-aminolevulinic acid for resection of malignant glioma: a randomised controlled multicentre phase III trial “, Lancet Oncol, 7: 392-401 (2006).

[4] New G, “Introduction to nonlinear optics”, Cambridge University Press, (2011).

[5] Zipfel WR, Williams RM, Christie R, Nikitin AY, Hyman BT, Webb WW, “Live tissue intrinsic emission microscopy using multiphoton-excited native fluorescence and second harmonic generation”, Proceedings of the National Academy of Sciences, 100(12): 7075–7080 (2003).

[6] Xu X, Cheng J, Thrall MJ, Liu Z, Wang X, Wong ST, “Multimodal non-linear optical imaging for label-free differentiation of lung cancerous lesions from normal and desmoplastic tissues”, Biomedical optics express, 4(12): 2855–2868 (2013).

[7] Gasecka P, “Polarization resolved nonlinear multimodal microscopy in lipids: from model membranes to myelin in tissues”, Theses, Université Aix-Marseille, (2015).

[8] Aloísio MG, Magalhes FL, Soares JS, Junior EP, de Lima MFR, Mamede M, de Paula AM, ” Second harmonic generation imaging of the collagen architecture in prostate cancer tissue”, Biomedical Physics & Engineering Express, 4(2): 025026 (2018).

[9] Hompland T, Erikson A, Lindgren M, Lindmo T, de Lange Davies C, “Second-harmonic generation in collagen as a potential cancer diagnostic parameter”, Journal of biomedical optics,13(5): 054050–054050 (2008).

[10] Paoli J, Smedh M, Ericson MB, "Multiphoton Laser Scanning Microscopy—A Novel Diagnostic Method for Superficial Skin Cancers", Seminars in Cutaneous Medicine and Surgery, 28(3): 190–195 (2009).

[11] Haringsma J, Tytgat GN, Yano H, Iishi H, Tatsuta M, Ogihara T, Watanabe H, Sato N, Marcon N, Wilson BC, Cline BC, “Autofluorescence endoscopy: feasibility of detection of gi neoplasms unapparent to white light endoscopy with an evolving technology”, Gastrointestinal endoscopy, 53(6): 642–650 (2001).

[12] Kobayashi M, Tajiri H, Seike E, Shitaya M, Tounou S, Mine M, Oba K, “Detection of early gastric cancer by a real-time autofluorescence imaging system”, Cancer letters, 165(2): 155–159 (2001).

[13] Ikeda N, Hiyoshi T, Kakihana M, Honda H, Kato Y, Okunaka T, Furukawa K, Tsuchida T, Kato H, Ebihara Y, “ Histopathological evaluation of fluorescence bronchoscopy using resected lungs in cases of lung cancer”, Lung Cancer, 41(3): 303–309 (2003).

[14] Jung W, Tang S, McCormic DT, Xie T, Ahn Y, Su J, Tomov IV, Krasieva TB, Tromberg BJ, Chen Z,” Miniaturized probe based on a microelectromechanical system mirror for multiphoton microscopy”, Opt Letters, 33(12): 1324–1326 (2008).

[15] Myaing MT, Ye JY, Norris TB, Thomas T, Baker JR, Wadsworth WJ, Bouwmans G, Knight JC, Russell P, “Enhanced two-photon biosensing with double-clad photonic crystal fibers”, Opt Letters, 28(14): 1224-6 (2003).

[16] Tang S, Jung W, McCormick D, Xie T, Su J, Ahn J, Tromberg BJ, Chen Z, “Design and implementation of fiber-based multiphoton endoscopy with microelectromechanical systems scanning”, J Biomed Opt, 14(3): 034005 (2009).

[17] Légaré F, Evans CL, Ganikhanov F, Xie XS, “Towards CARS Endoscopy”, Opt Express, 14(10): 4427-4432 (2006).

[18] Hayes JR, Sandoghchi SR, Bradly TB, Liu Z, Slavik R, Gouveia MA, Wheeler NV, Jasion G, Chen Y, Fokoua EN, Petrovich MN, Richardson DJ, Poletti F, “Antiresonant hollow core fibre with an one octave spanning bandwidth for short haul data communications” Journal of light wave technology, 35(3): 437-442 (2017).

[19] Cheng J-X, Xie X S,“ Coherent Raman Scattering Microscopy“, CRC Press, (2013).

[20] Miller RC, “Optical Harmonic Generation in Single Crystal $BaTiO_3$”, Physical Review, 134(5): A1313 (1964).

[21] Mostaco-Guidolin L, Rosin NL, Hackett T-L, “Imaging collagen in scar tissue: development in second harmonic generation microscopy for biomedical applications”, Int. J. Mol. Sci., 18: 1772 (2017).

[22] Masters BR, So P, “Handbook of biomedical nonlinear optical microscopy”, Oxford University Press on Demand, (2008).

[23] Pawley JB,” Handbook of Biological Confocal Microscopy”, Springer, (2006).

[24] Abdulkadir S, “Histopathology Made easy”, [online], Available: https://www.academia.edu/40884313/Histopathology_Made_easy [access 28 August 2021].

[25] Jacques SL, “Optical properties of biological tissues: a review”, Phys. Med. Biol., 58(11): R37–R61 (2013).

[26] Wu S, Butt H-J, “Near-infrared photochemistry at interfaces based on upconverting nanoparticles “, Phys. Chem. Chem. Phys, 35 (2017).

[27] Huang S, Heikal AA, Webb WW, “Two-Photon Fluorescence Spectroscopy and Microscopy of NAD(P)H and Flavoprotein”, Biophysical Journal, 82(5): 2811-2825 (2002).

[28] Ricard-Blum S, “The collagen family” Cold Spring Harb Perspect Biol, 3(1): a004978 (2011).

[29] Svoboda K, Yasuda R, "Principles of Two-Photon Excitation Microscopy and Its Applications to Neuroscience", Neuron., 50(6): 823–839 (2006).

[30] Keiser G, “Optical fibre communications”, McGraw-Hill, Inc., (1983).

[31] Thyagarajan K, Ghatak A, “Fiber optical essentials”, Wiley-Interscience, (2007).

[32] Saleh BEA, Teich MC, “Fundamentals of photonics”, Wiley-Interscience, (2007).

[33] Russell P, ”Photonic crystal fibers”, Science, 299(5605): 358–362 (2003).

[34] Okamoto K, “Fundamentals of optical waveguides”, Elsevier Academic Press, (2006).

[35] Yu F, Knight JC, “Negative curvature hollow – core optical fibre”, IEEE Journal of Selected topics, 22(2): 4400610 (2016).

[36] Agrawal GP, “Nonlinear fibre optics”, Academic press, (2007).

[37] Humbert G, Knight J, Bouwmans G, Russell P, Williams D, Roberts P, Mangan B, “Hollow core photonic crystal fibers for beam delivery”, Optics express, 12(8): 1477–1484 (2004).

[38] Knight JC, Skryabin DV, “Nonlinear waveguide optics and photonic crystal fibers“,Optics Express, 15(23): 15365-15376 (2007).

[39] Poletti F, “Nested antiresonant nodeless hollow core fiber”, Optics Express, 22(20): 23807-23828 (2014).

[40] Mosley P, Huang PW, Welch MG, Mangan BJ, Wadsworth WJ, Knight JC, “Ultrashort pulse compression and delivery in a hollow-core photonic crystal fiber at 540 nm wavelength “, Opt Letters, 35(21):3589-3591 (2010).

[41] Lombardini A, “Nonlinear optical endoscopy with micro-structured photonic crystal fibers”, Aix-Marseille Université, (2016).

[42] Shephard JD, Couny F, Russell PSJ, Jones JD, Knight JC, Hand DP,"Improved hollow-core photonic crystal fiber design for delivery of nanosecond pulses in laser micromachining applications", Applied optics, 44(21): 4582–4588 (2005).

[43] Couny F, Benabid F, Light PS, "Large pitch kagome-structured hollow-core photonic crystal fiber ", Optics Letters, 31(24): 3574-3576 (2006).

[44] Markos Ch, Travers JC, Abdolvand A, Eggleton BJ, Bang O, "Hybrid photonic-crystal fiber", Rev. Mod. Phys., 89: 045003 (2017).

[45] Sakr H, Chen Y, Jasion GT, Bradley TD, Hayes JR, Mulvad H, Davidson IA, Numkam Fokoua E, Poletti F "Hollow core optical fibres with comparable attenuation to silica fibres between 600 and 1100 nm", Nature Communications, 11: 6030 (2020).

[46] Jaworski P, Yu F, Carter RM, Knight JC, Shephard JD, Hand DP," High energy green nanosecond and picosecond pulse delivery through a negative curvature fibre for precision micro-machining", Optics Express, 23(7): 8498- 8506 (2015).

[47] Jaworski P, Yu F, Maier RRJ, Wadsworth WJ, Knight JC, Jonathan D. Shephard, Hand DP, "Picosecond and nanosecond pulse delivery through a hollow-core negative curvature fibre for micro-machining applications," Opt. Exp., 21(19): 22742–22753 (2013).

[48] Wang Z, Yu F, Wadsworth WJ, Knight JC, "Efficient 1.9 μm emission in H2 -filled hollow core fiber by pure stimulated vibrational Raman scattering", Laser Phys. Lett.,11(10): 105807 (2014).

[49] Bateman SA, Belardi W, Yu F, Webb CE, Wadsworth WJ, "Gain from Helium-Xenon discharges in hollow optical fibres at 3.5 μm", presented at the Advanced Photonics Conf., Barcelona, Spain, Paper SoM4B.3 (2014).

[50] Urich A, Maier RRJ, Yu F, Knight JC, Hand DP, Shephard JD, "Silica hollow core microstructured fibres for mid-infrared surgical applications", Journal of Non-Crystalline Solids, 377: 236 (2013).

[51] Urich A, Maier RRJ, Yu F, Knight JC, Hand DP, Shephard JD," Flexible delivery of Er:YAG radiation at 2.94 μm with negative curvature silica glass fibers: a new solution for minimally invasive surgical procedures", Biomed Opt Express, 4:193–205 (2013).

[52] Helmchen F, Fee MS, Tank DW, Denk W, "A Miniature Head-Mounted Two-Photon Microscope: High-Resolution Brain Imaging in Freely Moving Animals", Neuron, 31(6): 903-912 (2001).

[53] Sherlock B, Warren SC, Stone J, Knight J, Neil MAA, Paterson C, French PMW, Dunsby Ch, ‘‘Fibre-coupled multiphoton microscope with adaptive motion compensation’’, Biomed. Opt. Express, 6: 1876–1884 (2015).

[54] Sherlock B, Warren SC, Alexandrov Y, Yu F, Stone J, Knight J, Neil MAA, Paterson C, French PMW, Dunsby Ch, “ In vivo multiphoton microscopy using a handheld scanner with lateral and axial motion compensation “, J. Biophotonics, 11(2): 201700131 (2018).

[55] Liao Ch,Wang P, Huang ChY, Lin P, Eakins G, Bentley RT, Liang R, Cheng J,”In Vivo and in Situ Spectroscopic Imaging by a Handheld Stimulated Raman Scattering Microscope“, ACS Photonics, 5: 947−954 (2018).

[56] Fu L, Gu M, “Fibre-optic nonlinear optical microscopy and endoscopy“, Journal of Microscopy, 226(3): 195-206 (2007).

[57] Jung JC, Schnitzer MJ, “Multiphoton endoscopy“, Opt. Lett., 28(11): 90 –904 (2003).

[58] Hirose K, Aoki T, Furukawa T, Fukushima S, Niioka H, Deguchi S, Hashimoto M,“ Coherent anti-Stokes Raman scattering rigid endoscope toward robot-assisted surgery”, Biomedical Optics Express, 9(2): 387 (2018).

[59] Myaing MT, MacDonald DJ, Li X,“ Fiber-optic scanning two-photon fluorescence endoscope”, Opt. Lett., 31(8):1076–1078 (2006).

[60] Bird D, Gu M, “Compact two-photon fluorescence microscope based on a single-mode fiber coupler”, Opt. Lett., 27(12):1031–1033 (2002).

[61] Fu L, Gan X, Gu M, “Nonlinear optical microscopy based on double-clad photonic crystal fibers”, Opt. Express., 13(14): 5528–5534 (2005).

[62] Balu M, Liu G, Chen Z, Tromberg BJ, Potma EO,” Fiber delivered probe for efficient CARS imaging of tissues”, Opt Express, 18(3): 2380-2388 (2010).

[63] Deladurantaye P, Paquet A, Paré C, Zheng H, Doucet M, Gay D, Poirier M, Cormier JF, Mermut O, Wilson BC, Seibel EJ, “Advances in engineering of high contrast CARS imaging endoscopes”, Opt Express, 22(21): 25053–25064 (2014).

[64] Wang Z, Gao L, Luo P, Yang Y, Hammoudi AA, Wong KK, Wong STC, “Coherent anti-Stokes Raman scattering microscopy imaging with suppression of four-wave mixing in optical fibers”, Opt Express, 19(9): 7960–7970 (2011).

[65] Tai S-P, Chan M-C, Tsai T-H, Guol S-H, Chen L-J, Sun C-K, “Two-photon fluorescence microscope with a hollow-core photonic crystal fiber”, Opt Express, 12: 6122–6128 (2004).

[66] Brustlein S, Berto P, Hostein R, Ferrand P, Billaudeau C, Marguet D, Muir A, Knight J, Rigneault H," Double-clad hollow core photonic crystal fibre for coherent Raman endoscope", Opt Express,19 (13): 12562-12568 (2011).

[67] Kaur M, Lane PM, Menon C, "Scanning and Actuation Techniques for Cantilever-Based Fiber Optic Endoscopic Scanners—A Review", Sensor, 21: 251 (2021).

[68] Göbel W, Kerr JND, Nimmerjahn A, Helmchen F, "Miniaturized two-photon microscope based on a flexible coherent fiber bundle and a gradient-index lens objective", Optics Letters, 29(21): 2521-2523 (2004).

[69] Lukic A, Dochow S, Bae H, Matz G, Latka I, Messerschmidt B, Schmitt M, Popp J, "Endoscopic fiber probe for nonlinear spectroscopic imaging", Optica, 4(5): 496-501 (2017).

[70] Lukić A, Dochow S, Chernavskaia O, Latka I, Matthäus Ch, Schwuchow A, Schmitt M, Popp J, "Fiber probe for nonlinear imaging applications", Journal of Biophotonics, 9: 138-143 (2016).

[71] Fua L, Jainb A, Xieb H, Cranfielda Ch, Gu M, "Nonlinear optical endoscopy based on a double-clad photonic crystal fiber and a MEMS mirror", Optical Express, 14(3): 1027- 1032 (2006).

[72] Jung W, Tang S, McCormic DT, Xie T, Ahn Y, Su J, Tomov IV, Krasieva TB, Tromberg BJ, Chen Z," Miniaturized probe based on a microelectromechanical system mirror for multiphoton microscopy ", Optics Letters, 33(12): 1324-1326 (2008).

[73] Tang S, Jung W, McCormick D, Vie T, Su J, Ahn Y, Tromberg BJ, Chen Z, "Design and implementation of fiber-based multiphoton endoscopy with microelectromechanical systems scanning", J Biomed Opt., 14(3): 034005 (2009).

[74] Tekpinar M, Khayatzadeh R, Ferhanoglu O," Multi-pattern generating piezoelectric fibre scanner toward endoscopic applications", Optical Engineering, 58(2): 023101 (2019).

[75] Vilches S, Kretschmer S, Ataman C, Zappe H, "Miniaturized Fourier-plane fiber scanner for OCT endoscopy ", J. Micromech. Microeng., 27:105015 (2017).

[76] Liang W, Murari K, Zhang Y, Chen Y, Li M-J, Li X, "Increased illumination uniformity and reduced photodamage offered by the Lissajous scanning in fiber-optic two-photon endomicroscopy", J Biomed Opt., 17(2): 021108, (2012).

[77] Do D., Yoo H., Gweon D.-G., "Fiber-optic raster scanning two-photon endomicroscope using a tubular piezoelectric actuator", J. of Biomedical Optics, 19(6): 066010 (2014).

[78] Rivera DR, Brown CM, Ouzounov DG, Pavlova I, Kobat D, Webb WW, Xu C, "Compact and flexible raster scanning multiphoton endoscope capable of imaging unstained tissue ", PNAS, 108(43): 17598-17603 (2011).

[79] Wu Y, Leng Y, Xi J, Xingde Li X, “Scanning all-fiber-optic endomicroscopy system for 3D nonlinear optical imaging of biological tissues”, Optical Express, 17(10): 7907 – 7915 (2009).

[80] Ducourthial G, Leclerc P, Mansuryan T, Fabert M, Brevier J, Rémi Habert R, Braud F, Batrin R, Vever-Bizet Ch, Heckly GH, LucThiberville L, Anne DruilheA, Alexandre Kudlinski A, Louradour F, “Development of a real-time flexible multiphoton microendoscope for label-free imaging in a live animal”, Scientific Report, 5:18303 (2015).

[81] Lombardini A, Mytskaniuk V, Sivankutty S, Andresen ER, Chen X, Wenger J, Fabert M, Joly N , Louradour F, Kudlinski A, Rigneault H, “High-resolution multimodal flexible coherent Raman endoscope”,Light Sci. Appl. 7:10 (2018).

[82] Sherlock B, Yu F, Stone J, Warren S, Paterson C, Neil MAA, French PMW, Knight J, Dunsby Ch, “ Tunable fiber-coupled multiphoton microscopy with a negative curvature fiber”, J. Biophotonics, 9(7): 715 (2016).

[83] Setti V, Vincetti L, Argyros A, “Flexible tube lattice fibers for terahertz applications,” Opt Express 21(3): 3388–3399 (2013).

[84] Belardi W, Knight JC, “Effect of core boundary curvature on the confinement losses of hollow antiresonant fibers” Opt Express, 21(19): 21912–21917 (2013).

[85] Gao S-F, Wang Y-Y, Liu X-L, Ding W, Wang P, “Bending loss characterization in nodeless hollow-core anti-resonant fiber” Opt Express, 24(13): 14801-14811 (2016).

[86] Siegman A.E., “New developments in laser resonators”, Proc. SPIE 1224: 2–14 (1990).

[87] ISO Standard 11146, “Lasers and laser-related equipment – Test methods for laser beam widths, divergence angles and beam propagation ratios”, (2005).

[88] Pologruto TA, Sabatini BL, Svoboda K, “ScanImage: flexible software for operating laser scanning microscopes” Biomed. Eng. Online, 13 (2003).

[89] Schindelin J, Arganda-Carreras I, Frise E, Kaynig V, Longair M, Pietzsch T, Preibisch S, Rueden C, Saalfeld S, Schmid B, Tinevez J-Y, White DJ, Hartenstein V, Eliceiri K, Tomancak P, Cardona A,” Fiji: an open-source platform for biological-image analysis” Nature Methods, 9(7): 676–682 (2012).

[90] Galli R, Uckermann O, Andresen EF, Geiger KD, Koch E, Schackert G, Steiner G, Kirsch M, “Intrinsic Indicator of Photodamage during Label-Free Multiphoton Microscopy of Cells and Tissues”, Plos One, 9(10): 110295 (2014).

[91] Allocca G, Kusumbe AP, Ramasamy SK, Wanga N," Confocal/two-photon microscopy in studying colonisation of cancer cells in bone using xenograft mouse models", BoneKEy Reports, 851 (2016).

[92] Raghunvanshi DS, Moore SI, Fleming AJ, Yong YK, "Electrode Configurations for Piezoelectric Tube Actuators with Improved Scan Range and Reduced Cross-Coupling", IEEE/ASME Transactions on Mechatronics, Available Online (2020).

[93] Kinsler LE, Frey AR, Coppens AB, Sanders JV, "Fundamentals of Acoustics", 3rd ed., Wiley, New York (1982).

[94] Green EI, "The Story of Q", American Scientist, 43: 584–594 (1955).

[95] Zhao Y, Nakamura H, Gordon RJ, "Development of a versatile two-photon endoscope for biological imaging ", Biomedical Optical Express, 1(4): 1159 – 1172 (2010).

[96] Ghenuche P, Rigneaul H, Wenger J, "Photonic nanojet focusing for hollow-core photonic crystal fiber probes", Applied Optics, 51(36): 8637-8640 (2012).

[97] Ghenuche P, Rigneault H, Wenger J, "Hollow-core photonic crystal fiber probe for remote fluorescence sensing with single molecule sensitivity", Optics express,20(27): 28379-28387 (2012).

[98] Kudlinski A, Cassez A, Vanvincq O, Septier D, Pastre A, Habert R, Baudelle K, Douay M, Mytskaniuk V, Tsvirkun V, Rigneault H, Bouwmans G, "Double clad tubular anti-resonant hollow core fiber for non-linear microendoscopy " Opt Express, 28(10): 15062-15070 (2020).

[99] Optics Software for Layout and Optimization (OSLO), [online] Available: https://lambdares.com/oslo/, [Accessed 24 February 2018].

[100] LabView, [online] Available: https://www.ni.com/en-gb/shop/labview.html, [Accessed 24 February 2018].

[101] Bowman K, "An Introduction to Programming with IDL: Interactive Data Language", Academic Press, (2006).

[102] Diaspro A, "Confocal and two-photon microscopy: foundations, applications and advances", Wiley-Liss, (2001).

[103] Davis PJ, "Interpolation and approximation", Dover, (1975).

[104] Mueller M, "Introduction to Confocal Fluorescence Microscopy", SPIE, (2005).